Journal of Materials Chemistry A

ROYAL SOCIETY OF CHEMISTRY

REVIEW

View Article Online
View Journal | View Issue

Cite this: J. Mater. Chem. A, 2025, 13, 38753

Exploring metal halide perovskites as active architectures in energy storage systems

Juhi Juhi, [ab] Marcin Saski, [ac] Maria K. Kochaniec, [a] Władysław Wieczorek, *[a] Robert Dominko [bd] and Janusz Lewiński *[ac]

Metal halide perovskites (MHPs) have emerged as versatile, cutting-edge materials in the field of energy conversion and storage, expanding their influence well beyond photovoltaics to transform technologies such as lithium-ion batteries (LIBs), supercapacitors (SCs), and photo-induced energy storage systems. Initially renowned for their remarkable performance in solar cells, MHPs are now attracting significant attention in energy storage applications due to their outstanding properties, including high ionic conductivity (10^{-3} to 10^{-4} S cm^{-1}), long charge-carrier diffusion lengths, tunable band gaps, large surface areas, and structurally flexible lattices. Both lead-based and lead-free variants have demonstrated considerable promise, particularly as electrode materials and in the fabrication of stable artificial solid electrolyte interphases (ASEIs). In addition, the strong light absorption capabilities of halide perovskites have opened pathways toward photo-rechargeable devices, where perovskite solar cells (PSCs) are integrated directly with energy storage systems to enable sustainable and efficient photo-charging. This review provides a concise overview of recent progress in the synthesis and compositional engineering of MHPs, examining how structural and chemical tuning governs their optoelectronic and physicochemical properties. It further explores the emerging applications of perovskite materials in diverse energy storage devices, emphasizing the role of composition in optimizing electrochemical performance. Special attention is given to the integration of PSCs with storage systems as a promising avenue for next-generation multifunctional energy technologies. Finally, the review outlines future opportunities and the key challenges that must be addressed to fully realize the potential of MHPs in high-performance, durable, and scalable energy storage solutions.

Received 27th May 2025
Accepted 14th September 2025

DOI: 10.1039/d5ta04267d

rsc.li/materials-a

1. Introduction

In recent years, the demand for renewable energy sources has increased due to rising pollution from fossil fuels and the ongoing energy crisis. Solar energy is recognized as the most abundant clean alternative to conventional energy generation methods. However, due to their variable availability, the fourth technological revolution calls for innovative energy storage solutions like batteries and supercapacitors (SCs) to enhance the use of electricity generated from these renewable sources.[1,2] Currently, lithium-ion batteries (LIBs) represent the most advanced and preferred technology for energy storage solutions in the market. The development of LIB technology began in the late 1980s and early 1990s, and its recognition culminated in the award of the Nobel Prize in 2019. Since then, it has established itself as the benchmark due to its superior energy density (100–265 Wh kg^{-1}) compared to any other battery technology currently available.[3] Given their significantly high energy and power density, LIBs have attracted a great deal of interest for their use in portable electronics, but also in battery electric vehicles (BEVs).[4] Nonetheless, LIB technology faces certain drawbacks, for instance, capacity deterioration, safety concerns, and inadequate cycle stability.[5,6] Given the current limitations, existing LIB technology is unable to achieve the ultimate goal of decarbonizing the world and necessitates additional research. In contrast, SCs offer superior cycle life and high power capability by storing energy through the reversible adsorption of ionic species on highly porous electrodes. However, their widespread adoption is constrained by a comparatively lower energy density, which limits their use in applications requiring long-duration energy storage.[7] To address the limitations associated with LIBs and SCs, the development of next-generation LIB technologies offering enhanced longevity, faster charging, improved safety, and cost-effectiveness critically depends on advancements in key battery components, including electrodes, electrolytes, and interfaces. Similarly, achieving higher energy density in SCs requires

[a]Faculty of Chemistry, Warsaw University of Technology, Noakowskiego 3, 00-664 Warsaw, Poland. E-mail: wladyslaw.wieczorek@pw.edu.pl
[b]National Institute of Chemistry, Hajdrihova Ulica 19, 1000 Ljubljana, Slovenia
[c]Institute of Physical Chemistry, Polish Academy of Sciences, Kasprzaka 44/52, 01-224 Warsaw, Poland
[d]ALISTORE – European Research Institute, CNRS FR 3104, 15 Rue Baudelocque, Amiens 80039 Cedex, France

significant innovation in material design and device architecture. Therefore, researchers are constantly exploring next-generation materials to replace traditional electrode materials. One of the emerging groups of active materials in this field is inorganic and organic–inorganic metal halide perovskites (MHPs), with the general formula ABX_3, where A represents a small organic or inorganic cation, B is a divalent metal ion, and X is a halogen anion. MHPs are a specific family of crystalline materials featuring a soft crystal lattice with excellent structural and compositional tunability.[8]

Over the past decade, MHP materials and their wide-ranging applications have experienced remarkable growth. Their exceptional optoelectronic properties, combined with the ability to control photogenerated ions and electronic charges simultaneously, make them an outstanding material for numerous technological uses. MHPs first gained prominence as the foundation for a new era in photovoltaics, with perovskite solar cells (PSCs) rapidly transforming the renewable energy landscape.[9–13] These cutting-edge devices offer simpler fabrication methods, lower production costs, and the potential to surpass silicon-based efficiencies, thanks to their high light absorption coefficients across a broad spectrum. As a result, PSCs not only have the capacity to complement the existing photovoltaic (PV) market but also to challenge the long-standing dominance of crystalline silicon cells, paving the way for new manufacturing paradigms.[14] Among the diverse family of ABX_3 perovskites, methylammonium lead iodide ($MAPbI_3$) and formamidinium lead iodide ($FAPbI_3$), along with their mixed cation or mixed halide forms, are prototype mono-cationic materials for the absorber layer in PSCs.[15–19] The real boom started after the application of these MHPs as active material in solar cells, starting at a power conversion efficiency (PCE) ~3.8% in 2009 ($MAPbI_3$ in dye-sensitized architecture).[20] Since then, intensive material innovation and device engineering have pushed efficiencies beyond 26%, particularly through A-site and X-site compositional engineering strategies. For example, the integration of multiple cations in $FAPbI_3$-based systems like triple cation $Cs_x(MA_{0.17}FA_{0.83})_{(1-x)}Pb(I_{0.83}Br_{0.17})_3$ perovskite in meso-architecture has led to PCE values of ~21.1% in 2016,[19] and more recently, the efficiencies exceeded 26% in a small-area unit cell.[18,21] The efficiency progress of PSCs and standard device architectures[22] is shown in Fig. 1. A particularly promising direction in this field is the development of flexible PSCs, which have achieved PCEs exceeding 25% (certified at 24.90%), surpassing other flexible solar cell technologies.[23] Thanks to their high power-to-weight ratio, flexible PSCs are well suited for use in mobile and space energy systems, as well as in portable functional devices.[24] Despite these impressive performance gains, the commercialization of perovskite-based devices is still hindered by insufficient long-term operational stability.[25–27] Device instability arises from degradation of both the active and buffer layers, which is linked to intrinsic properties of MHPs, such as lattice disorder, ion migration, and trap-state formation. These degradation processes can be triggered or accelerated by environmental factors (moisture, oxygen) and external stressors, including light exposure, heat, and electric fields. Over the past decade, significant progress has been made in improving PSC stability through various strategies.[26,28] However, stability remains a key challenge requiring continued investigation. Furthermore,

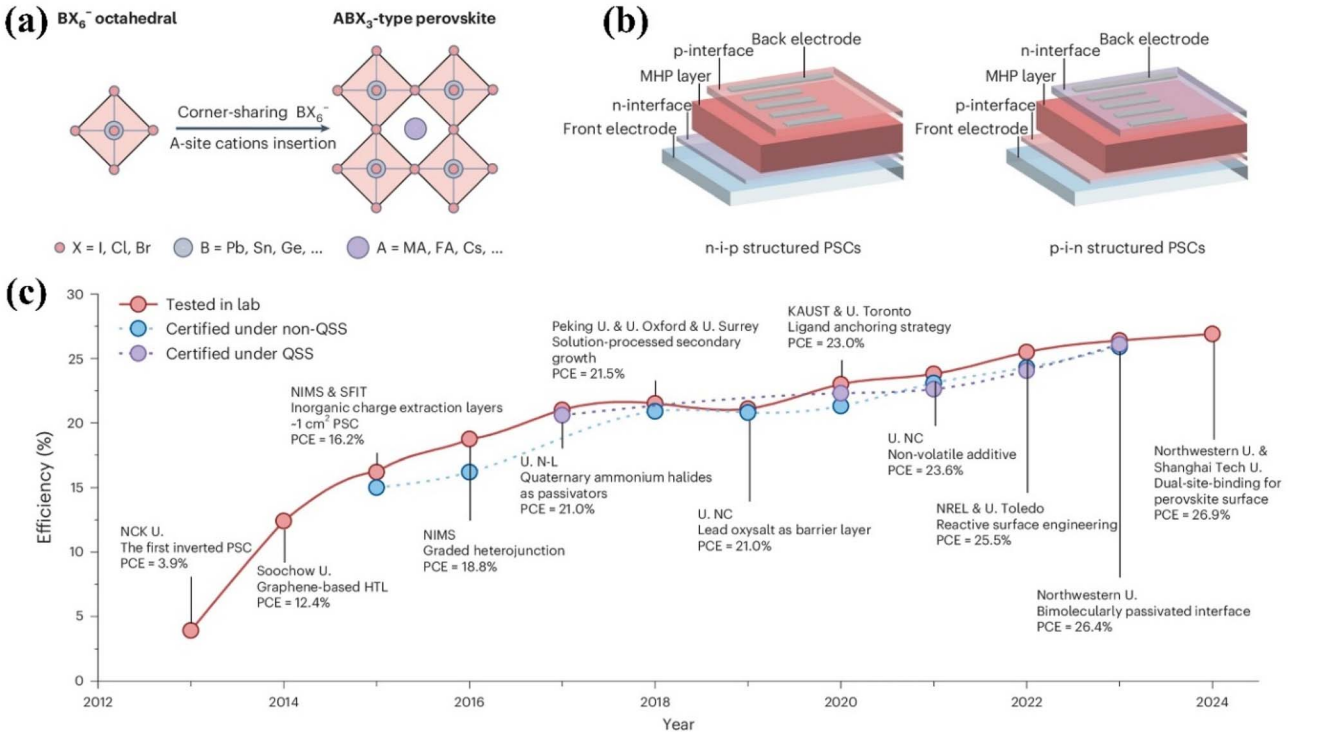

Fig. 1 (a) Representation of the ABX_3 perovskite building principle, (b) typical architectures of PSC devices, (c) the efficiency gain of PSCs[22] Copyright 2024, *Nat. Photonics*.

scaling-up PSCs to large-area devices presents additional difficulties, particularly in achieving high-quality, uniform perovskite films at industrially relevant scales, meaning that the performance of large-area PSC modules still falls short of commercialization requirements. The tunable optical and electronic properties of MHPs, combined with rapid progress in their compositional engineering, have positioned them as promising candidates for a wide range of optoelectronic applications. As a result, their potential has quickly expanded beyond PVs, with high-performance light-emitting diodes (LEDs) leading the way. Perovskite-based LEDs have already achieved electroluminescence external quantum efficiencies exceeding 25% for red and green emissions, while maintaining exceptional color purity.[12,29,30] Beyond LEDs, MHPs show strong promise for other advanced devices, including lasers, field-effect transistors, photodetectors, and photocatalysts.[31–33] More recently, their unique properties have been explored in next-generation memory devices[34–36] and even artificial synapses for neuromorphic computing.[37]

Not surprisingly, MHPs have also paved their way for a new class of energy storage devices where solar PV systems have been integrated with batteries such as LIBs,[38] Zn metal batteries,[39] Na-metal batteries,[40] LIBs,[41] and also SCs.[42] This can be attributed to the same properties that make them ideal for PV devices. The initial use of hybrid MHPs ($MAPbBr_3$ and $MAPbI_3$), synthesized through hydrothermal methods as anodes in LIBs, was documented by Xia *et al.*[43] Since that time, various studies have been carried out, including the creation of new MHPs for their use as anodes in LIBs[44–46] and their adoption as artificial solid electrolyte interphases (ASEI).[47,48] Moreover, their integration in SCs has also gained considerable attention because of exciting properties such as electronic confinement, structural flexibility, attractive performance, and stability.[49] For example, recently Riaz and coworkers showed that the $CsSnBr_3$/PANI-based electrode exhibits good cyclic stability (91.6%). They further confirmed the high energy density and power density (37.5 Wh kg^{-1}, 1275.4 W kg^{-1}) of these electrodes at 3.4 A g^{-1}.[50]

It is no coincidence that new review articles appear regularly in these booming research areas.[8,9,12,25,51,52] We aim to provide an original and valuable expert perspective that delivers a concise yet comprehensive overview of recent advances in the preparation and compositional engineering of MHP materials in different forms, with particular emphasis on the factors influencing their optoelectronic and physicochemical properties. It offers a focused perspective on the promising yet still underexplored potential of these materials in energy storage systems. The discussion covers both all-inorganic and hybrid organic–inorganic MHPs, emphasizing their electrochemical performance across different device configurations. Key topics include the use of perovskites as anode materials for LIBs and SCs, the design of ASEIs on lithium metal, and a detailed examination of lithium storage mechanisms in perovskite-based anodes. Recent developments in photo-induced LIBs and SCs are also reviewed. In addition, the article highlights the critical physicochemical properties that underpin the versatility and high performance of MHPs, linking these characteristics to their functional behaviour in energy storage applications. The review concludes with an outlook on future research directions and the remaining challenges that must be addressed to unlock the full potential of MHPs in next-generation energy storage technologies.

2. Fundamental properties of MHP materials

MHPs offer distinct advantages over conventional inorganic semiconductors, particularly their exceptional chemical and structural tunability combined with favorable carrier dynamics and transport properties. By tailoring parameters such as stoichiometry, dimensionality, and nanostructure, key material characteristics, including bandgap energy, crystallinity, and chemical stability, can be precisely engineered. A defining feature of perovskites is ion-migration: although often regarded as a drawback that contributes to performance losses and instability in optoelectronic devices, it can also be strategically exploited to enable novel functionalities in halide-perovskite-based electronics.[53] Consequently, detailed investigations of their crystal structures and elemental compositions are essential to fully understand and optimize the unique electrochemical behavior of different halide-perovskites and to identify the most suitable candidates for use as active materials in diverse devices, including LIBs and SCs. This section focuses on the fundamental attributes of MHPs that govern their chemical and optoelectronic properties, incorporating recent progress toward addressing stability challenges that impact device performance. Additionally, various synthesis strategies for MHPs will be discussed, given their decisive influence on the physicochemical characteristics of the resulting materials. Finally, special attention will be given to the interactions between MHPs and Li-ions, which play a critical role in their application within lithium-based energy storage systems.

2.1. Compositional engineering and phase transitions of MHPs

As mentioned previously, the typical three-dimensional (3D) MHPs share the basic chemical formula ABX_3, where 'A' is a monovalent cation (such as Cs^+, $CH_3NH_3^+$ or MA, $HC(NH_2)_2^+$ or FA *etc.*), 'B' is a divalent transition metal cation (generally Sn^+, Pb^+, *etc.*), and 'X' is a monovalent halide anion (Cl^-, Br^-, I^-), forming corner-sharing $[BX_6]^{4-}$ octahedra cavities containing the 'A' cations as shown in Fig. 2a.[29] This family of materials can be further divided into two groups according to the nature of the A-site cation: all-inorganic halide perovskites incorporating inorganic cations and organic–inorganic halide perovskites (or so-called hybrid halide perovskites) incorporating charge-compensating amine cations. For achieving structural stability in the 3D network, the ionic radii of the cations and anions should follow the empirically derived Goldschmidt tolerance factor (t) and octahedral factor (μ).[54] Both tolerance and octahedral factor predict the perovskite crystal stability with variations in metal cations and halide anions. The following equation can describe the tolerance factor:

$$t = \frac{r_A + r_X}{\sqrt{2}(r_B + r_X)} \quad (1)$$

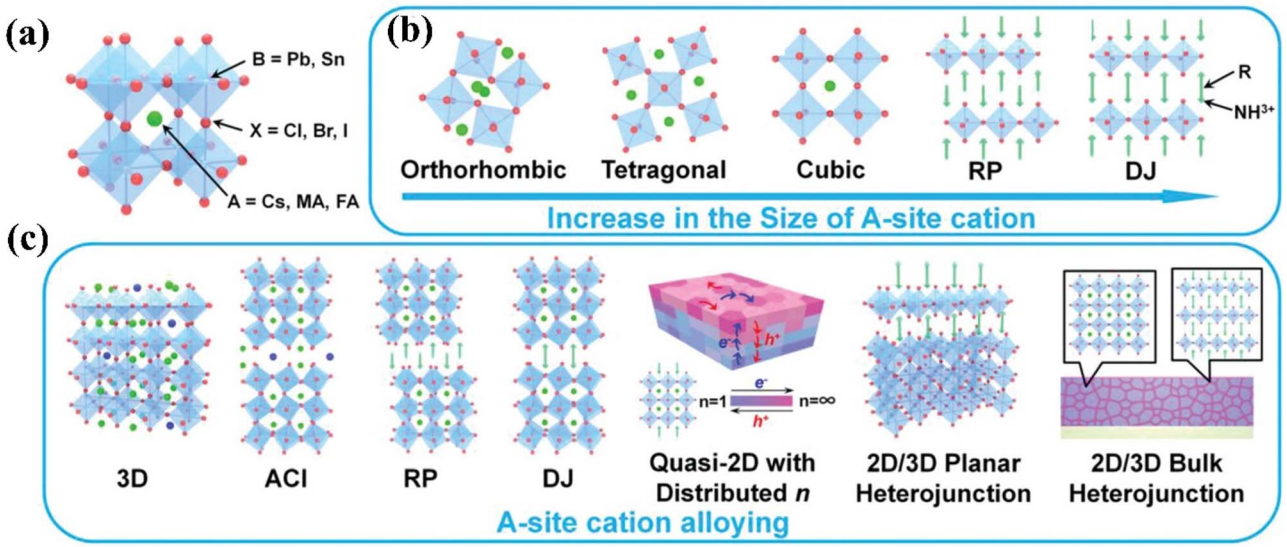

Fig. 2 (a) Schematic illustration of the typical ABX_3 structure of MHPs. (b) Formability of 3D MHPs as a function of size of A-site cation. (c) ABX_3 structure evolution with A-site cation alloying[29] Copyright 2020, *Adv. Funct. Mater.*

where r_A and r_X are the ionic radii of the A-site cation and X-site halide anion, and r_B is the Shannon ionic radius of the B-site cation, respectively, in the ABX_3 perovskite halide compounds. The octahedral factor can be expressed by the following equation:[55]

$$\mu = \frac{r_B}{r_X} \quad (2)$$

A stable 3D perovskite structure at room temperature and ambient pressure is generally achieved when the t and μ fall within the ranges $0.813 < t < 1.107$ and $0.442 < \mu < 0.895$, respectively,[56] and a highly symmetric cubic structure characteristic of MHPs is typically stabilized only within a narrower tolerance factor range of $0.9 < t < 1$.[57] Deviation from this range results in distortion of the cubic lattice, leading to lower symmetry structures. The size of the A-site cation plays a crucial role in dictating the structural stability of perovskites. Since the A-site cations reside within the $[BX_6]^{4-}$ framework, a cation that is lower than the ideal size causes tilting of the BX_6 octahedra. This tilting induces structural distortion, giving rise to lower symmetry phases such as tetragonal or orthorhombic forms. Moreover, if the size of the A-site cation is larger than the ideal size, two-dimensional (2D) structures like Ruddlesden–Popper (RP) phase and Dion–Jacobson (DJ) phase will be formed (Fig. 2b).[58] Moreover, when A-site cations are alloyed by small or oversized cations, various crystal structures will be formed, including one-dimensional (1D) structures (Fig. 2c).[59,60]

2.2. Factors guiding chemical and physical properties of MHPs

The physicochemical properties of MHPs are critical determinants of their functionality in energy storage devices. For example, in traditional LIBs, MHPs with intermediate band gaps (such as $CsPbBr_3$) function effectively as stable electrodes owing to their favorable ion-electron conductivity, while their ability to tolerate defects reduces capacity loss.[8] For photo-induced LIBs, MHPs with narrow band gaps (like $MAPbI_3$) perform exceptionally as materials for light absorption, where their high carrier mobility facilitates effective conversion of solar energy to charge, and ambipolar transport allows for concurrent Li-ion storage.[61] These advantageous properties stem from the intrinsic electronic structure of MHPs, which grants them high optical absorption, long carrier diffusion lengths, and tunable energy levels. The electronic and opto-electronic properties of MHPs can be influenced by a combination of intrinsic material factors and external stimuli, which in turn determine their performance in these energy storage devices. The key factors are specified more precisely below.

2.2.1 Compositional factors. The physicochemical properties of MHP materials originate from their unique inorganic lattice and the intricate interactions between the inorganic framework and organic components.[62] Consequently, structural modification of MHPs achieved by introducing specific cations or anions at various sites within the parent ABX_3 perovskite structure has become a widely adopted strategy to tailor their fundamental physical and chemical characteristics. Initially, the prevailing belief was that the role of the A-site cation was to maintain the overall charge neutrality. However, more recent studies have demonstrated that the versatility of the A-site cation indirectly affects the structure–property–performance.[63] In contrast, the electronic properties of MHPs are more directly governed by the composition of the B- and X-site ions.[64,65] For example, in $MPbX_3$, the deeper region of valence band minima (VBM) consists mainly of p orbitals of the 'X' ions and a small contribution from the overlapping of s orbitals of the 'B' ions. The edge of VBM consists of anti-bonding states of the s orbitals of 'B' ions and p orbitals of 'X' ions. Therefore, when different

halides are used with different electronegativity, the position of the VBM edge changes, hence the bandgap changes. On the other hand, the conduction band minima (CBM) are mainly determined by the antibonding overlap between the p orbitals of 'B' site ions and a small contribution of the p orbitals of 'X' site ions.[66] In the case of tin-based perovskites ($ASnX_3$), the interactions between the A-site cation and the $[SnX_3]^-$ sublattice are more complex. Predicting the properties of these materials requires consideration of additional factors such as redox stability and defect chemistry.[67,68] The featured electronic structure of MHPs is different from that of conventional semiconductor materials, *i.e.*, gallium arsenide (GaAs), with their band gaps forming in between bonding and antibonding orbitals.[69] A detailed discussion on the influence of A-, B-, and X-site doping on the physicochemical properties of MHPs is provided in the subsequent sections.

2.2.1.1 'A' cation. The A-site cation in MHPs plays an indirect but essential role in influencing their electronic properties. By altering the lattice volume and introducing structural distortions to the ideal cubic ABX_3 framework, the A-site cation leads to the formation of various non-cubic phases. Although these structural changes have only a limited impact on the electronic band structure, they are critical for understanding and optimizing the optoelectronic performance of MHPs.[63,70] A highly symmetric cubic structure tends to exhibit reduced band gaps due to improved packing symmetry. However, as the A-site cation size increases beyond this optimal range ($t > 1$), the resulting lattice expansion and structural deformation lead to bandgap widening.[71] This structural deformation primarily affects ionization energy (IE), while volumetric/lattice expansion has a more pronounced influence on electron affinity (EA). The ionic nature of MHPs makes them susceptible to ion migration, particularly under external electric fields or illumination. Such migration can create crystal defects that degrade device performance through current–voltage hysteresis, phase segregation, and chemical corrosion. A-site engineering has emerged as an effective strategy to mitigate these challenges. For instance, partial substitution of A-site cations with oversized organic ions like guanidinium (Gua^+) introduces stabilizing hydrogen bonds with the $[PbX_6]^{4-}$ lattice,[72] suppressing lattice dynamics and enhancing device stability and performance.[73] Additionally, A-site doping can stabilize desirable perovskite phases and address long-standing issues in long-term operational stability, a key barrier to commercialization.[74]

The size of the A-site cation also constrains the formation and stability of the $[BX_6]^{4-}$ framework. To date, five monovalent cations are known to form 3D lead-halide perovskites: MA,[75] FA[75] and Cs^+ cations[76] and the more recently reported aziridinium (Az)[77] and methylhydrazinium (MHy).[78] Of these, α-$MAPbX_3$, α-$AzPbX_3$, α-$FAPbX_3$, and α-$CsPbX_3$ can form perovskite structures across all halide compositions. However, α-$FAPbI_3$ and α-$CsPbI_3$ are metastable and tend to transform into the non-perovskite yellow δ-phases under ambient conditions.[79] $MHyPbCl_3$ and $MHyPbBr_3$ form B-site distorted perovskite structures,[78] while $MHyPbI_3$ crystallizes in a perovskitoid phase similar to δ-$CsPbI_3$.[80] To improve stability and tailor the material properties, these A-site cations can be mixed to form alloyed perovskites, as mentioned previously. Moreover, certain large organic cations can be partially incorporated into the 3D perovskite lattice to enhance their optoelectronic performance. Examples include imidazolium (IM^+; $C_3H_5N_2^+$),[81] dimethylammonium (DMA^+; $CH_3NHCH_3^+$)[82] ethylammonium ($CH_3CH_2NH_3^+$; EA),[83] guanidinium ($C(NH_2)_3^+$; Gua),[73] and acetamidinium ($CH_3C(NH_2)_2^+$; Aca).[84] All mentioned materials exhibit temperature-dependent phase transitions; therefore, this needs to be taken into account during device design.

In parallel, the development of 2D perovskites using even larger organic cations as spacer ligands has gained considerable interest. These materials consist of inorganic $[BX_6]^{4-}$ octahedral sheets separated by bulky organic layers, leading to a general composition of $(L_2BX_4)(ABX_3)_{n-1}$, where 'L' represents the organic spacer. Commonly used ligands include butylammonium (BA) and phenylethylammonium (PEA), which impart hydrophobicity and thus enhance moisture resistance. These 2D perovskites exhibit strong photoluminescence, attributed to their quantum well-like electronic structures. However, a significant limitation of these materials in optoelectronic applications is the structural heterogeneity resulting from the coexistence of domains with varying inorganic layer thicknesses. Additionally, their anisotropic charge transport properties further restrict their applicability. The structural diversity and design strategies for 2D perovskites will be discussed in detail in the following section of this review.

2.2.1.2 'B' cation. In MHPs, the B-site is typically occupied by divalent metal cations such as Ge^{2+}, Sn^{2+}, and Pb^{2+}, which possess fully or partially filled 4s, 5s, and 6s valence orbitals, respectively. These ns^2 lone-pair electrons contribute significantly to the upper region of the VB, playing a crucial role in determining the VBM and, consequently, the electronic structure of MHPs. The stereochemical activity of these lone pairs strongly influences the electronic properties, and an increase in atomic radius (from Ge to Sn to Pb) has been shown to correspond with a widening of the bandgap. This trend is attributed to the changes in the energy level and activity of the lone-pair states. In 2D MHPs, reduced structural dimensionality allows for a broader range of off-center displacements of the B-site metal cation. As a result, the stereochemical activity of the ns^2 lone-pair electrons is more pronounced in 2D Ge-, Sn-, and Pb-based perovskites.[65] Goesten and Hoffmann conducted an in-depth analysis of the impact of substituting Pb^{2+} with Sn^{2+} or Ge^{2+}, along with halide variation, on the bandgap of $CsPbBr_3$.[64] Complementarily, Nishat *et al.* proposed that a reduction in the B-site cation's atomic radius increases the nuclear electrostatic attraction on valence electrons, thereby raising the IE and EA.[85] This stronger binding of valence electrons can lower both the bandgap and bonding energy. Thus, a decrease in atomic radius may result in narrower band gaps, in contrast to trends driven by lone-pair effects. Moreover, the stability of the B-site divalent oxidation state decreases across the series Ge < Sn < Pb, reflecting increasing electronegativity. For example, substituting Pb^{2+} with Sn^{2+} results in a significant reduction in IE and a moderate decrease in EA. More recently, Liang *et al.* demonstrated that B-site substitution with lanthanide or alkaline-earth metal ions enhances lattice cohesion and

increases I^- migration barriers, offering a more effective stabilization strategy than A-site or X-site doping.[86] Beyond divalent substitution, MHP structures can also be tailored through the incorporation of trivalent B^{3+} cations (*e.g.*, Bi^{3+}, Sb^{3+}) or a combination of monovalent (B^+) and trivalent (B^{3+}) cations. In the former case, the classic ABX_3 structure is no longer maintained due to charge imbalance, resulting in new stoichiometries such as $A_3B_2X_9$. These structures lack the corner-sharing BX_6 octahedral connectivity, leading to significantly altered optoelectronic properties. In the latter case, double perovskites of the type $Cs_2B(I)B(III)X_6$ are formed, preserving the perovskite framework while enabling broader compositional versatility. The trivalent B-site in such double perovskites is often occupied by p-block elements like Bi^{3+},[87,88] Tl^{3+},[89] Sb^{3+},[89] and In^{3+} [90] though examples incorporating d- and f-block elements also exist.[91–93] The monovalent B(I) cation can include Li^+, Na^+, Ag^+, Tl^+, Cu^+, or Au^+. Among these, Cu^+, Tl^+, and Au^+ are rarely used due to their strong reducing capabilities, which can destabilize common B^{3+} species.[94] Halide substitution in these systems frequently results in phase segregation. Cl-based perovskites exhibit high structural stability, whereas bromide analogues are typically metastable, and iodide-based compounds are often synthetically inaccessible.[95,96] An alternative structural strategy involves vacancy-ordered perovskites, particularly for tetravalent B-site ions. Representative examples include Cs_2TiX_6 [97] and Cs_2SnX_6,[98] where charge balance is maintained by introducing ordered vacancies, offering unique optoelectronic properties while preserving structural stability.

2.2.1.3 'X' anion. The composition of the halide (X-site) in MHPs plays a pivotal role in determining the feasibility of perovskite lattice formation. It enables fine-tuning of key physicochemical properties, including bandgap energy and photoluminescence characteristics (shown in Fig. 3).[99] For instance, $APbCl_3$ perovskites exhibit a wide bandgap of approximately 3.0 eV, resulting in white coloration and luminescence in the 400–450 nm range. In comparison, $APbBr_3$ analogues possess a narrower bandgap (~2.2 eV) with emission centered around 500–550 nm, whereas $APbI_3$ counterparts exhibit the narrowest bandgap (~1.5 eV), corresponding to emission in the near-infrared range of 800–850 nm. Mixed-halide compositions exhibit intermediate band gaps and emission profiles, which are approximately proportional to their halide content. This compositional flexibility enables the rational design of perovskite materials tailored for specific optoelectronic applications.[100] Substitution at the halide site also significantly impacts the electronic structure, particularly the IE and EA of the material. This can be theoretically analysed by examining the trend in halide anion properties, such as increasing atomic radius and lone-pair electron energy levels along the series Cl^- ($3s^2$) → Br^- ($4s^2$) → I^- ($5s^2$). The CBM is primarily governed by the B-site cation p-orbital energy levels, which tend to shift downward as the atomic radius of the halide increases. This trend can be attributed to the quantum confinement effect: as the B–X bond length increases from Cl to I, the electron localization on the B-site is reduced, leading to a lowering of the CBM energy. Simultaneously, the VBM shifts upward across the same series, primarily due to the decreasing electronegativity of the halide ions (Cl > Br > I). These combined effects of halide substitution enable precise control over the electronic band structure of ABX_3 perovskites, further enhancing their suitability for a wide range of optoelectronic applications.[101]

2.2.2 Phase transition and external factors. MHPs, owing to their inherently ionic lattice structures, exhibit significant ion migration, dynamic lattice behavior, and a pronounced sensitivity to external stimuli such as temperature, pressure, and redox conditions. These characteristics render both hybrid organic–inorganic and all-inorganic MHPs highly responsive to their environment and often undergo structural phase transitions. Polymorphism is one of the most notable consequences of this structural flexibility, which profoundly influences the electronic structure and, consequently, the optoelectronic properties of MHP.[102–105] Structural features considered in the A-site cation engineering and temperature- and pressure-induced phase transitions in selected hybrid organic–inorganic MHPs are shown in Fig. 4. The diversity in crystal structures and associated phase transition temperatures for both lead-based and lead-free MHPs is summarized in Table 1. In general, 3D MHPs adopt a high-symmetry cubic structure at elevated temperatures and undergo sequential phase transitions from cubic to tetragonal to orthorhombic upon cooling. For instance, Hansen *et al.*[106] Employed high-resolution powder neutron diffraction to study the temperature-dependent phase transitions in $MAPbI_3$. The authors observed transitions from the γ-

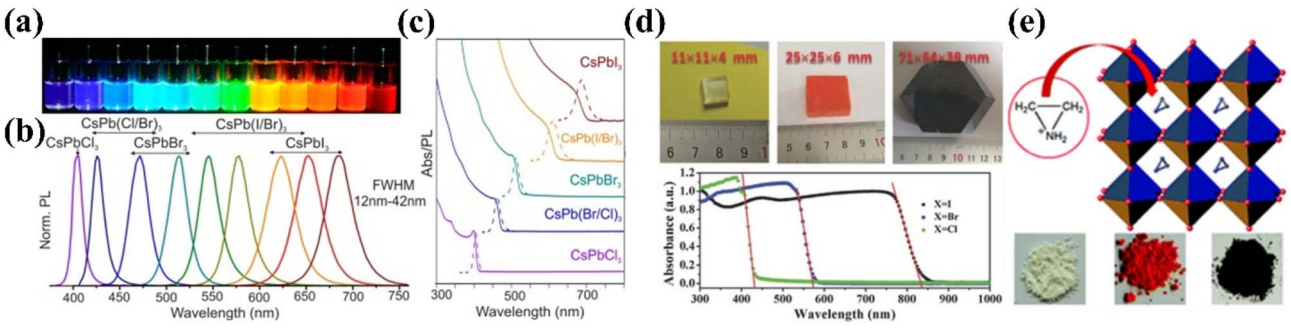

Fig. 3 Influence of the X-site halogen atom on optical properties of MHP: (a–c) luminescence and absorbance of $CsPbX_3$ materials[99] Copyright 2019, *Nat Commun.*, (d) image and absorbance of $MAPbX_3$ crystals, (e) visualization of $AzPbX_3$ powders.

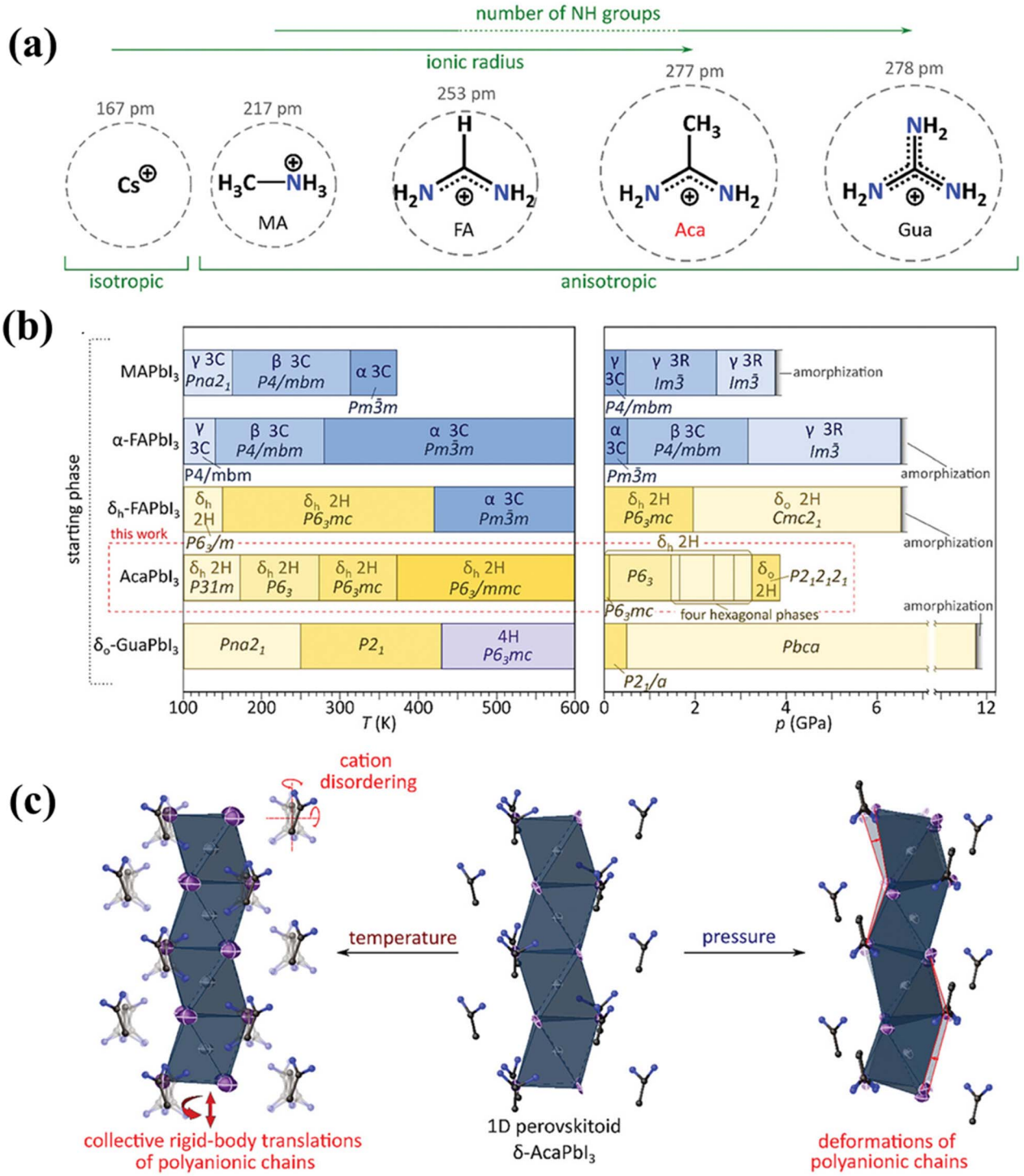

Fig. 4 (a) Structural features considered in A-site cation engineering for organic–inorganic perovskites, (b) temperature- and pressure-induced phase transitions in selected hybrid organic–inorganic MHPs (yellow, blue, and violet colors represent 1D preovskitoid, 3D perovskites, and 3D perovskitoid phases, respectively), (c) representation of the thermally- and pressure-induced structural transformations in δ-$AcaPbI_3$.[104]

to the β-phase and from the β- to the α-phase at 165 K and 327 K, respectively. Interestingly, recent *ab initio* quantum dynamics simulations for pristine $MAPbI_3$ demonstrated that the structural deformations induced by thermal fluctuations and phase transitions are on the same order as deformations induced by defects.[107] Cs-based halide perovskites offer higher structural stability than their organic analogues; they are also susceptible to structural phase transitions under the influence of external factors. For example, $CsPbI_3$ perovskite exhibits four polymorphs with temperature-induced transitions (Fig. 5a).[108] Remarkably, the black phase α-$CsPbI_3$ perovskite exhibits poor structural stability at room temperature and spontaneously

Table 1 Different crystal systems (lead-based and lead-free) of commonly used MHPs in LIBs, their phase transition temperature, and space group

Compound	Crystal system	Space group (polytype)	Temperature (K)	References
$MASnI_3$	Tetragonal	$Pm\bar{3}m$ (3C/α)	293	75
		$I4cm$ (3C/β)	200	
$MASnCl_3$	Cubic	$Pm\bar{3}m$ (3C/α)	478	114
	Rhombohedral	$R3m$	350	
	Monoclinic	$P1c1$	318	
$MASnBr_3$	Tetragonal	$P4mm$ (3C/β)		115
$MAPbBr_3$	Cubic	$Pm\bar{3}m$ (3C/α)	298	116
	Tetragonal	$I4/mcm$ (3C/β)	220	117
		$P4/mmm$ (3C/β)	150–155	118
	Orthorhombic	$Pna2_1$		118
$MAPbCl_3$	Cubic	$Pm\bar{3}m$ (3C/α)	200	116
	Tetragonal	$P4/mmm$ (3C/β)	173–179	118
	Orthorhombic	$P222_1$	< 173	118
$FAPbI_3$	Cubic	$Pm\bar{3}m$ (3C/α)	420	75
	Hexagonal	$P6_3$ (2H/δ)	270	75
	Trigonal	$P3$ (2H/δ)	150	75
$FAPbBr_3$	Cubic	$Pm\bar{3}m$ (3C/α)	275	119
	Tetragonal	$P4/mbm$ (3C/β)	175	
	Orthorhombic	$Pnma$ (δ)	100	
$FASnI_3$	Cubic	$Pm\bar{3}m$ (3C/α)	275	119
	Tetragonal	$P4/mbm$ (3C/β)	175	
	Orthorhombic	$Pnma$ (3C/γ)	100	
$FASnBr_3$	Cubic	$Pm\bar{3}m$ (3C/α)	275	120
	Tetragonal	$P4/mbm$ (3C/β)	175	
	Orthorhombic	$Pnma$ (3C/γ)	100	
$CsPbI_3$	Cubic	$Pm\bar{3}m$ (3C/α)	593	75
	Orthorhombic	$Pnma$ (δ)	293	121
$CsPbBr_3$	Cubic	$Pm\bar{3}m$ (3C/α)	433	122
$CsSnI_3$	Cubic	$Pm\bar{3}m$ (3C/α)	500	123
	Tetragonal	$P4/mbm$ (3C/β)	380	
	Orthorhombic	$Pnma$ (3C/γ)	300	
$CsSnBr_3$	Cubic	$Pm\bar{3}m$ (3C/α)	298	124
$CsSnCl_3$	Cubic	$Pm\bar{3}m$ (3C/α)	413	114
$CsGeI_3$	Cubic	$Pm\bar{3}m$ (3C/α)	533	125
$CsGeBr_3$	Cubic	$Pm\bar{3}m$ (3C/α)	538	125

transforms to the yellow, photoinactive, non-perovskite δ-phase. Moreover, as shown in Fig. 5b, these distinct phases exhibit markedly different optoelectronic characteristics, including variations in band gap, photoluminescence quantum yield, charge carrier mobility, and carrier lifetime.[109] Moreover, the impact of high pressure has also been extensively utilized to deepen the understanding of structure–property relationships of MHPs.[110] For example, Kong *et al.*[111,112] investigated high-pressure-induced phase transitions in $MAPbBr_3$. This material experiences a cubic–cubic phase transition from $Pm\bar{3}m$ (3C) to $Im\bar{3}$ (3R) at approximately 0.5 GPa, which was attributed to the distortion of the $PbBr_3$ polyhedron (Fig. 5c). The authors also indicated that the narrowest band gap (Fig. 5d), along with the longest carrier lifetime (Fig. 5e), is also observed near the phase-transition pressure of approximately 0.5–0.6 GPa. Their results have highlighted the effectiveness of using pressure to modulate crystal structures, which results in a favorable enhancement of material properties. Additionally, the effect of phase changes on electronic and optical properties of three perovskite phases of $CsSnI_3$, as well as their non-perovskite structure, was studied by D. D. Nematov *et al.*[113] The authors showed that the absorption (Fig. 5f) and photoconductivity (Fig. 5g) of $CsSnI_3$ are enhanced in the infrared and visible light ranges as it transitions from the low-temperature phase to the high-temperature phase. In contrast, the stable yellow phase of $CsSnI_3$, known as the δ-phase, only absorbs short-wavelength light. The high levels of absorption and optical conductivity suggest that all $CsSnI_3$ crystals, which have a perovskite structure, possess excellent spectral characteristics suitable for photovoltaic applications.

In general, most perovskite and perovskitoid materials undergo no more than five distinct phase transitions before decomposing at elevated temperatures due to the volatility of A-site constituents or amorphization under high pressure.[103,126,127] Notably, δ-$AcaPbI_3$ (Fig. 4) represents a unique case with the most extensive polymorphism reported among MHPs, exhibiting at least nine distinguishable polymorphs. Of these, four occur under varying temperature conditions at ambient pressure, while five emerge under high-pressure conditions at room temperature. All identified phases are variations of distorted 2H

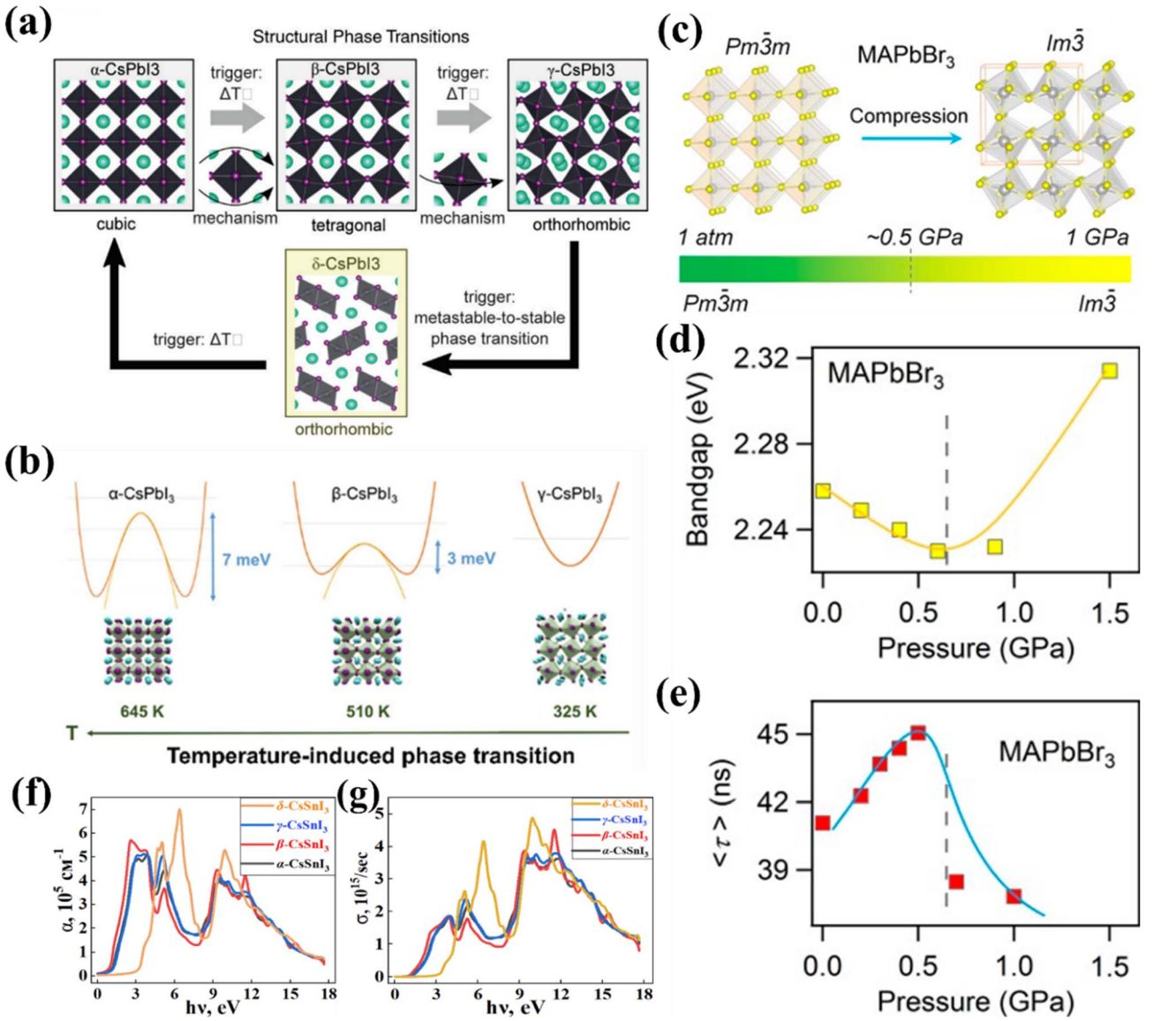

Fig. 5 (a) Variable-temperature phase transitions among the $CsPbI_3$ polytypes,[108] (b) illustration of variation of bandgap with the phase transition of $CsPbI_3$ crystal[109] Copyright 2018, *ACS Nano*. (c) Pb–Br inorganic frameworks of $MAPbBr_3$ for low-pressure $Pm\bar{3}m$ and high pressure $Im\bar{3}$ phases. The high-pressure phase in $MAPbBr_3$ exhibits the characteristic elongation of the lead–halide octahedral, together with smaller lead–halide–lead bond angles. (d and e) Demonstration of the band-gap narrowing and carrier-lifetime prolongation in $MAPbBr_3$ at mild pressures, respectively.[111] Copyright 2016, *Proc. Natl. Acad. Sci. U. S. A.* (f) and (g) Calculated absorption coefficient and optical conductivity of α-, β-, γ-, and δ-phases of $CsSnI_3$ as a function of photon energy in the *X* direction.[113] Copyright 2025, *J. Electron. Mater.*

polytypes. Interestingly, δ-$AcaPbI_3$ also undergoes partial amorphization under high pressure, followed by recrystallization due to Pb atom displacement along the *c*-axis.[104] Beyond polymorphism, ABX_3 perovskites can also exhibit polytypism, which is a specific form of polymorphism characterized by variations in the stacking sequence of otherwise identical layers.[15] Polytypes combine crystal sub-units of α/3C and δ/2H phases and are commonly observed in systems incorporating oversized A-site cations, such as Aca,[104] DMA,[82] as well as in mixed FA perovskites.[15] For example, hybrid organic–inorganic lead halides can form polytypes within various crystal systems, including hexagonal (2H, 4H, 6H or 8H), cubic (3C), and rhombohedral (3R, 9R).[15,128] Gratia *et al.*[128] noted that hexagonal polytypes emerge as transitional products on the surface of thin films of mixed-ion perovskites during the annealing process, unveiling a crystallization polytypic sequence of 2H–4H–6H–3C. The perovskite structure can be cut into layers by the addition of elongated organic BA or PEA cations, leading to the formation of 2D perovskite phases.[129]

2.2.3 Dimensionality. By leveraging the diverse structures and compositions of MHPs, the dimensionality of MHPs can be precisely adjusted, ranging from 3D to various low-dimensional forms such as quasi-2D, 2D, 1D, and zero-dimensional (0D) configurations. There are two types of low-dimensionalities, one

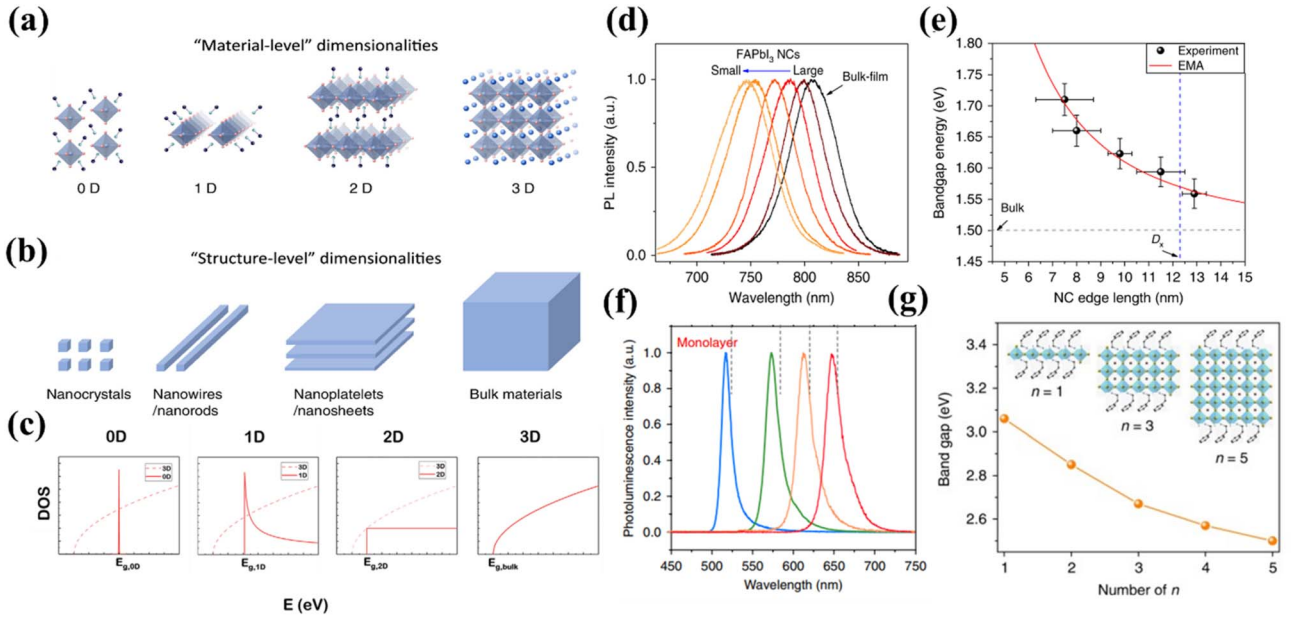

Fig. 6 (a) Schematic representation of "material-level" and (b) "structure-level" 3D bulk, 2D, 1D, and 0D perovskite materials[130] Copyright 2020, *InfoMat*, and (c) is the corresponding density of states *versus* the energy E_g[131] Copyright 2021, *Small*. (d) Photoluminescence (PL) spectra of $FAPbI_3$ nano-crystals (NCs) with different sizes. (e) Bandgap energies *versus* the edge length of $FAPbI_3$ NCs[132] Copyright 2021, *Small*. (f) PL of exfoliated monolayers for 2D layered $BA_2(MA)_{n-1}Pb_nI_{3n+1}$ Ruddlesden–Popper perovskites of $n = 1$ to 4 homologues[135] Copyright 2018, *Nat. Mater.* (g) The bandgap of $PEA_2A_{1.5}Pb_{2.5}Br_{8.5}$ (A = MA and Cs) perovskites with different numbers of layers[136] Copyright 2018, *Nat. Commun.*

is the "structure-level" and "material-level".[130] The "structure-level" low-dimensional aspect highlights the different morphologies and typically refers to nanostructures like nanosheets, nanowires, and nanocrystals (NCs) (Fig. 6a). In contrast, the "material-level" low-dimensional aspect of perovskite focuses on the fundamental structure where the $[BX_6]^{4-}$ octahedra are interspersed with large dielectric spacer molecules, resulting in a bulk formation of atom-level 0D clusters, 1D quantum wires, or 2D quantum wells (QWs) (Fig. 6b). The crystalline perovskite nanostructures with reduced dimensionality show distinctive optoelectronic properties with quantum-confined effect compared with their bulk counterparts (Fig. 6c).[131] Due to this phenomenon, the bandgap energy of low-dimensional perovskites is greater than that of their bulk forms. This is accompanied by a variation in the geometric size of perovskite nanostructures, which further alters the bandgap. As depicted in Fig. 6d, the photoluminescence emission wavelengths were systematically adjusted through the gradual decrease in the size of $FAPbI_3$ NCs.[132] Consequently, the calculated bandgap energy rose from 1.5 eV in bulk material to more than 1.7 eV for perovskite NCs with an edge length of approximately 8 nm (Fig. 6e). In addition to the hybrid perovskite NCs, inorganic perovskite NCs and quantum dots (QDs) also exhibit bandgap energies dependent on size or diameter, such as $CsPbI_3$ and $CsPbBr_3$.[133,134] This size effect can also be anticipated in 1D perovskite nanowires (NWs), where the diameter determines the bandgap energy and emission wavelength independent of the length.[134] Furthermore, in 2D perovskites, the octahedral layers are situated between the organic spacers. These organic compounds provide extra functionality, such as a tunable quantum well structure that can be modified by varying the length and type of the organic chain. Fig. 6f presents the photoluminescence spectra of 2D $BA_2(MA)_{n-1}Pb_nI_{3n+1}$ perovskites, which depend on the number of layers, demonstrating a significant wavelength tuning range from approximately 520 nm to 650 nm (~130 nm difference, corresponding to a shift of about ~0.47 eV).[135] A comparable layer-dependent pattern was observed in 2D perovskites composed of three cations that include both organic (PEA, MA) and inorganic (Cs) components (Fig. 6g), revealing a consistent decrease in bandgap energy as the number of layers increases, with an energy difference of up to ~0.6 eV between single-unit-cell and five-unit-cell crystals.[136]

2.3. Preparation of MHPs and MHP-based batteries and supercapacitors

2.3.1 Preparation of MHPs. Preparation methods of MHPs, alongside the chemical composition, are one of the key factors influencing the physicochemical properties of the title materials. To date, numerous techniques for obtaining MHPs in the form of bulk materials,[137] nanocrystalline,[31,138,139] single-crystal materials,[100] and thin film[13,100] have been reported. These processes have been applied, and they can be categorized as occurring in liquid, gas, and solid phases. Selected methods for the preparation of perovskite materials are presented in Fig. 7. Solution-based synthesis of bulk or single-crystal MHPs remains one of the most widely employed methods for preparing perovskite materials (Fig. 7a, c and d); however, it is constrained by the limited availability of suitable solvents. In most cases, highly ionic perovskite precursors are dissolved in

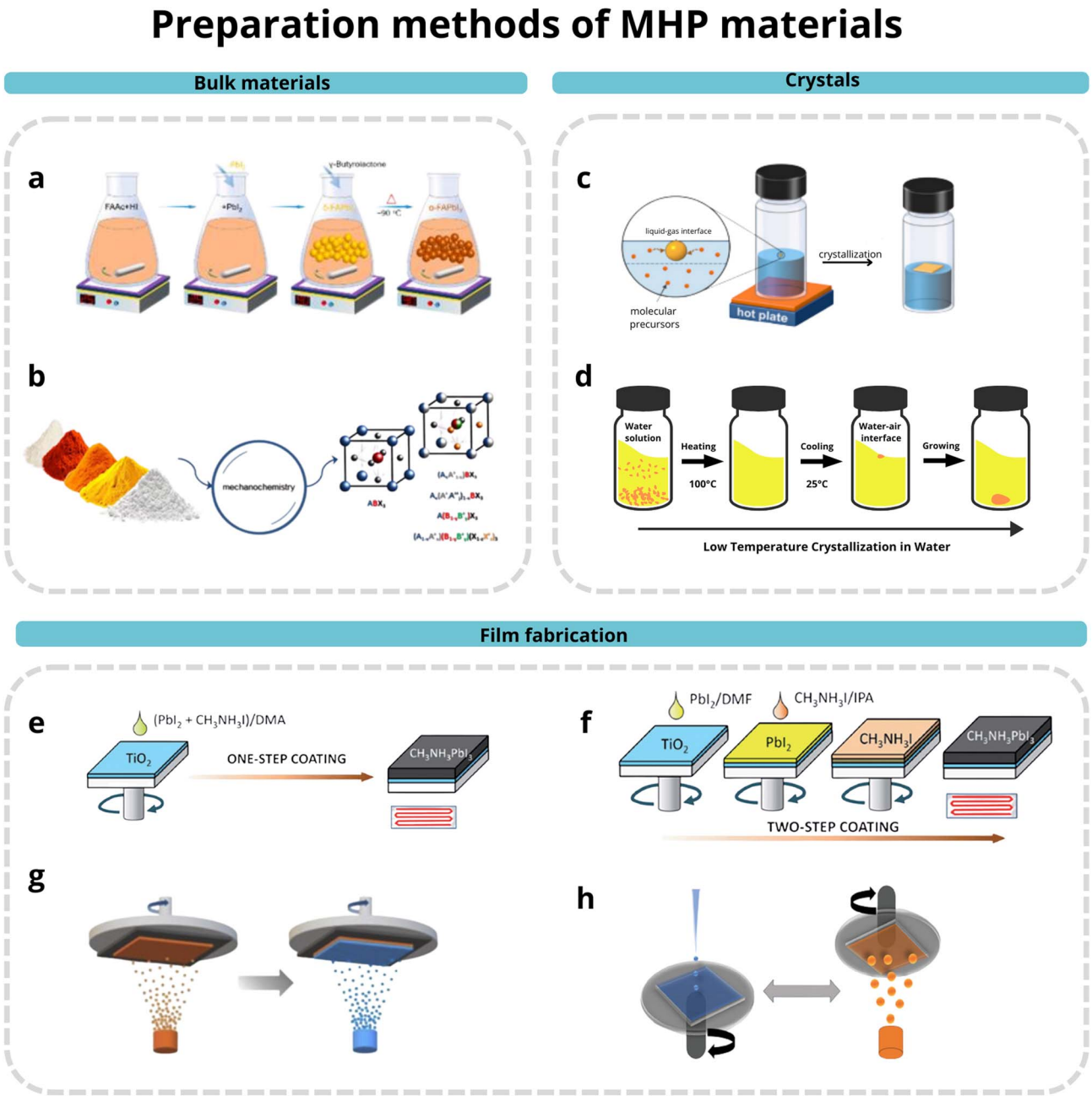

Fig. 7 Selected methods of the preparation of various forms of MHP materials, including (a, c and d) solution-based synthesis, (b) solid-state mechanochemical synthesis, (e) one-step and (f) two-step deposition, (g) vacuum evaporation, and (h) hybrid evaporation-solution approach.

toxic solvents such as dimethylformamide (DMF), often in combination with an antisolvent to promote crystallization. Other solvents capable of dissolving perovskite precursors, including *N*,*N*-dimethylacetamide and *N*-methyl-2-pyrrolidone, are also recognized as toxic.[140] Although the less hazardous dimethyl sulfoxide (DMSO) can effectively dissolve metal halides. However, due to its high boiling point, DMSO is difficult to dispose of and poses challenges for large-scale processing.[141]

Furthermore, the solution-based approaches for the preparation of MHPs may be considered as relatively versatile, they are also limited by substrate solubility and long-term stability. In 2015, the Lewiński group made a groundbreaking discovery, describing a new pathway for the production of perovskite materials through a mechanochemical process (Fig. 7b), involving solvent-free grinding of substrate powders in a ball mill.[142] This solvent-free synthetic approach is very attractive to curtail the chemical waste generation and simplify the preparation process. The solid-state mechanochemical preparation of MHPs enables the production of high-purity material in a short time and with low energy input, facilitating the use of precursors that are difficult to dissolve, such as CsCl[143] or

AgCl.[95] Hence, the mechanochemical synthesis offers a highly flexible platform for doping engineering at different atomic sites.[137] Subsequently, the MHPs derived from mechanochemical synthesis were successfully used for the fabrication of PSC, which contributed to an approximately 10% relative improvement in cell efficiency and operational characteristics compared to devices based on analogous solution-derived perovskite materials, and resolved the issue of the long-term storage of perovskite materials.[142,144] Later on, the solution of PSC properties was attributed to the lower density of trap states within materials, due to the higher quality of MHP grains on the surface.[145] Mechanochemical synthesis offers several advantages, including precise control over stoichiometry, improved reproducibility, enhanced stability, and higher phase purity in the resulting mechano-perovskite materials. It also enables more feasible large-scale production.[146] Although this method is fast, efficient, and environmentally friendly, relying on energy generated through grinding, shearing, and compression, the underlying mechanisms remain relatively poorly understood.

In the process of preparing perovskite thin films for various devices, deposition,[100,147,148] and patterning[13] are often key steps. Regarding wet methods, a further complication arises from the solvent-mediated growth of polycrystalline perovskite thin films, which can be carried out through either a one-step or two-step deposition approach. The one-step coating usually involves pre-mixed perovskite solution (*e.g.*, PbI_2 and MAI) followed by anti-solvent dripping, and the two-step sequential procedure,[149] one of the main methods used for depositing perovskite films for various applications,[150] which involves deposition of an inorganic layer before converting the film to perovskite by reacting with organic solution (Fig. 7e and f, respectively). By altering synthesis conditions, different nucleation and growth behaviors occur, which in turn directly shape the microscopic morphology of perovskite films, then change their optical and electrical properties.[151] These dominant deposition techniques typically use DMF-based precursor solutions, which remain the dominant deposition technique, yet they face the same environmental and health concerns associated with toxic solvents.[152] DMSO, while a safer alternative, is highly hygroscopic, often resulting in poor film crystallinity and the formation of numerous point defects.[141] Moreover, PSCs fabricated using DMSO-mediated synthesis generally exhibit lower efficiencies than those produced with DMF.[141,153,154] Consequently, solvent engineering to achieve high-quality perovskite films remains a major challenge.[155] To overcome the cost and scalability issues associated with the low-humidity requirements for device fabrication, studies are now investigating high-humidity conditions. The goal is to better understand perovskite crystal growth and to develop more robust, stable perovskite films.[147]

The solvent-mediated growth of polycrystalline MHP thin films suffers from critical limitations, including sensitivity to processing conditions, poor control over solvent-mediated crystallization, low reproducibility between laboratories, and restrictions on film size. To address these drawbacks, vacuum evaporation has emerged as a rapidly advancing solvent-free fabrication route (Fig. 7g).[156,157] This method enables uniform deposition of precursors and precise control over film thickness. Nevertheless, the power conversion efficiencies of vacuum-evaporated PSCs still lag behind those of high-quality solution-processed devices.[158,159] Recently, a hybrid evaporation-solution approach has been proposed as a promising alternative (Fig. 7h). This technique involves evaporating metal halide precursors onto a substrate, followed by spin-coating an organic halide precursor solution to complete film formation.[157,160–162] This hybrid strategy combines the advantages of both techniques, offering improved film quality and greater processing flexibility, and may represent a viable route toward scalable, high-performance perovskite device fabrication.

2.3.2 Preparation of MHP-based batteries and supercapacitors. An in-depth understanding of the crystal structure and elemental composition of MHPs is crucial to explain the unique electrochemical behaviours observed in various MHP-based LIBs.[43] This disparity underscores the importance of examining the influence of chemical composition on Li-ion storage properties. It is also important to note that both MHP-based batteries and SCs are fabricated by ISO standards. Typically, the electrode fabrication involves preparing a slurry composed of the active material (MHPs), a binder (polyvinylidene fluoride, PVDF), and a conductive additive (*e.g.*, hard carbon) in a particular weight ratio (most commonly 80 : 10 : 10). This mixture is dissolved usually in *N*-methyl-2-pyrrolidone (NMP) and cast to form the anode. While this method is widely regarded as the "gold standard" in LIB manufacturing, initially developed for chemically robust materials such as oxides, it poses challenges when applied to MHPs. The soft crystal lattice of MHPs is prone to dissolution in polar organic solvents, which can compromise the phase integrity during processing. The MHP solubility is also intentionally used in solution-based methods for producing perovskite solar cells, where solvent mixtures such as DMF : DMSO enable the formation of uniform thin films. Although this property does not preclude the use of MHPs in LIBs, it necessitates careful control over processing conditions to preserve phase purity. As a result, alternative fabrication routes such as solid-state approaches, including mechanochemical synthesis, are being explored to address these challenges and enhance the stability of MHP-based electrodes during device fabrication.[146,163]

One of the biggest challenges in current perovskite processing is the need for extremely dry and inert conditions. This is because MHPs are quite sensitive to moisture and oxygen. The fact that we can't carry out solid-state processing in regular environments really drives up both the initial and ongoing costs, especially when it comes to large-scale production of active materials. The use of gloveboxes, dry rooms, and specialized equipment for controlled atmospheres adds significantly to these expenses. This financial hurdle highlights the importance of future research not just in enhancing material stability, but also in creating moisture-tolerant MHP compositions and scalable fabrication methods that can work in normal conditions. At the moment, there aren't any thorough studies looking into the socio-economic factors of using

MHPs in LIBs. This is mainly because the use of MHPs in LIBs is still in its early stages of development, which is making it tough to accurately assess material and processing costs. However, similar to the early forecasts for perovskite solar cells, there's hope that MHP-based LIBs could become cost-effective as technology advances. This optimism stems from the relatively low cost of precursors, like lead salts, and the possibility of low-temperature processing.[164,165] While MHPs aren't quite ready to be used as commercial anode materials yet, their unique characteristics, such as mixed ionic–electronic conductivity, the ability to tune their composition, and high dielectric constants, point to a promising future in energy storage technologies.

2.4. Mechanism of lithium interaction with MHPs

The LIB utilizing MHPs ($MAPbBr_3$ and $MAPbI_3$) as an anode was first reported in 2015 by Xia *et al.*[43] The authors described good electrochemical performance for $MAPbBr_3$ with a first discharge capacity of 331.8 mAh g^{-1} at a current density of 200 mA g^{-1}, which is six times of the maximum theoretical capacity (55.96 mAh g^{-1}) if it is assumed that one Li-ion could intercalate per formula unit. This significant difference in electrochemical performance suggests a conversion reaction or another effect that is at play, since six Li-ions per formula unit would otherwise be required.[166] Despite these impressive performance metrics, the key mechanism by which Li-ion is intercalated in MHPs remains unknown. Initially, two mechanisms were

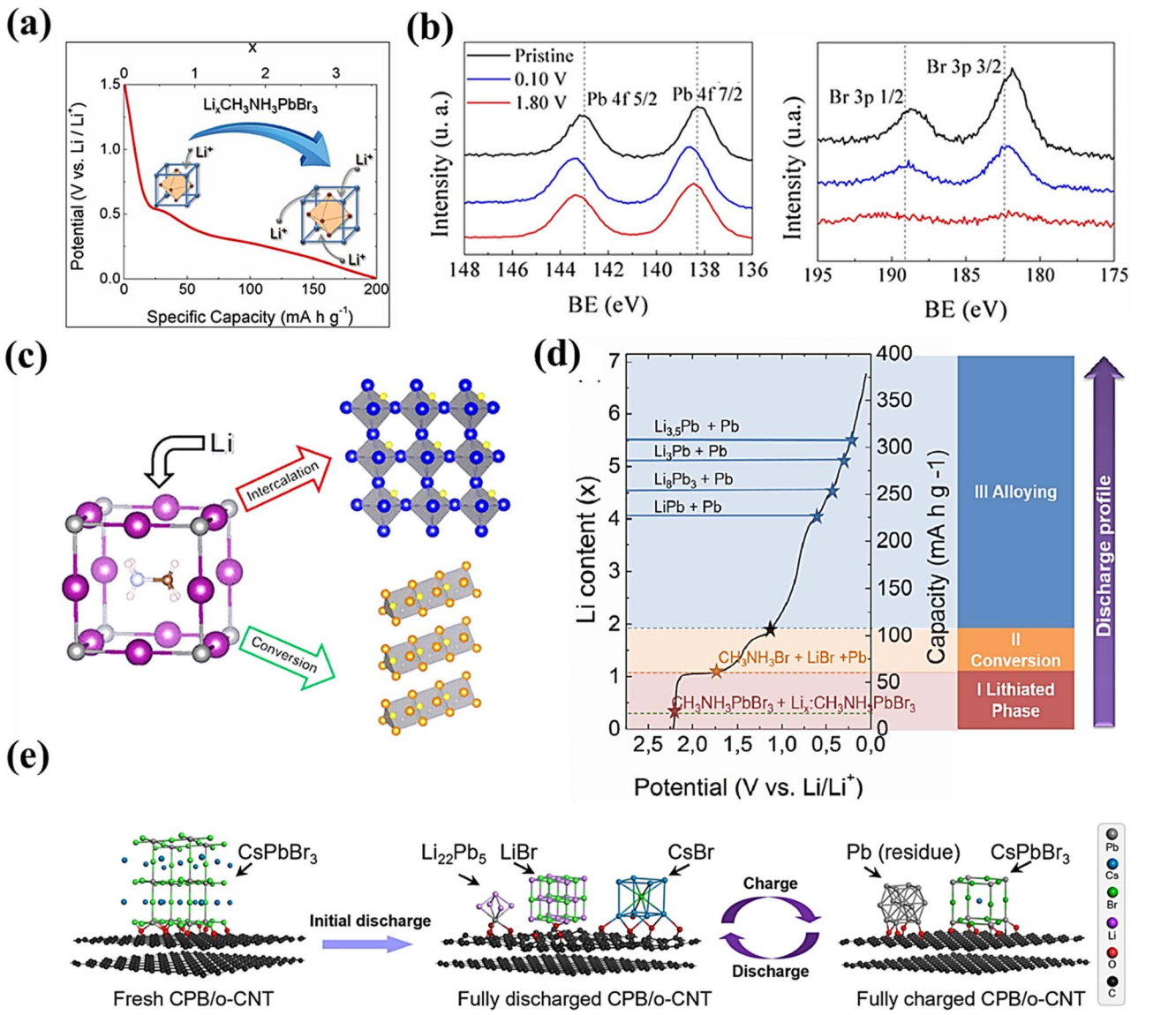

Fig. 8 (a) Crystal structure of organometal halide perovskite $MAPbBr_3$ indicating multiple Li-ion interaction. (b) Pb 4f and Br 3d core-level XPS signal of $MAPbBr_3$ anodes at different states: pristine, 0.10 V (discharge), and 1.80 V (subsequent charge)[167] Copyright 2017, *J. Phys. Chem. Lett.* (c) Schematic illustration of conversion and intercalation mechanism occurring in organic–inorganic MHPs[166] Copyright 2017, *ACS Energy Lett.* (d) The recorded discharge profile, where each stage is highlighted in a different color: first, the pure material (red), and lithiated phase (red); second, the conversion stage (orange), and, third, the alloying stage (blue)[168] Copyright 2019, *ChemElectroChem*. (e) Schematic illustration of the structural evolution process of CPB/o-CNT composite upon cycling[44] Copyright 2025, *Energy Storage Mater.*

Table 2 Li-transport mechanisms, SEI composition & evolution of different MHPs

Perovskite material	Electrolyte	Li storage mechanism/proposed reaction	Initial SEI characteristics	SEI evolution	Ref
$CsPbCl_3$	1 M $LiBF_4$ in PVDF-HFP + $BMIMBF_4$ (1 : 3 w/w)	Conversion → 2Li + $CsPbCl_3$ → CsCl + 2LiCl + Pb; subsequent Li–Pb alloying (Li_xPb) during deeper discharge	Likely contains LiCl, CsCl, Li–Pb alloys, solid electrolyte matrix	*Ex situ* XRD after 10 cycles: loss of $CsPbCl_3$ peaks; intensification of Pb + Li_xPb_y → conversion + alloying dominant	45
$CsPbBr_3$	1 M $LiPF_6$ in EC : DEC : DMC (1 : 1 : 1) with 5% FEC	(1) Intercalation → conversion→ alloying $CsPbBr_3 + 6.4Li^+ + 6.4e^- \rightarrow CsBr + Li_{22}Pb_5 + 2LiBr$ (discharged) (2) Partial reformation of the $CsPbB_3$ on charge $xCsBr + Li_{22}Pb_5 + 2xLiBr \rightarrow xCsPbBr_3 + (22 + 2x)Li^+ + (22 + 2x)e^- + (5 - x)$Pb (residue) (charged)	Likely contains FEC-derived FEC-rich SEI, LiBr, CsBr, LiPb alloys, and Pb residue	*Ex situ* XRD and XPS after long-term cycling; reduced content of $CsPbBr_3$ perovskite; pulverization → CsBr/Pb nanoparticles on CNTs	44
$CsPbI_3$	1 M $LiPF_6$ in EC/DMC (1 : 1)	Intercalation forming Li_xCsPbI_3 at higher V; deeper discharge yields conversion and Li–Pb alloying	Probably contains LiF, Li_xPF_y, $Li_xPF_yO_z$ from salt decomposition; Li-alkoxy species (CH_3OLi, $(C_2OLi)_2$) from EC/DMC reduction; possible Cs/Li iodides	SEI forms in the first cycle and stabilizes; post-100-cycle XRD/SEM: δ-$CsPbI_3$ peaks retained	46
$MAPbBr_3$/$MAPbI_3$/$MAPbIBr_2$	1.0 M $LiPF_6$ in EC/DEC (1 : 1) vol ratio)	Li intercalation followed by Pb(II) → Pb(0) reduction and conversion to LiX + Pb + Li_xPb alloys (LiPb, $Li_{2.6}Pb$, $Li_{4.4}Pb$, *etc.*), plus SEI formation (LiF, Li_2CO_3, organics); below ∼0.6 V, alloying–dealloying dominates	LiF, Li_2CO_3, alkoxides; Pb/Li_xPb in SEI; possible LiI residues	Pb, Li–Pb alloys, and halide products may remain embedded in SEI after 10 cycles	169
$MANiCl_3$	1.0 M $LiPF_6$ in EC/DMC ((1 : 1) vol ratio)	Intercalation into $MANiCl_3$ lattice → conversion to MACl + LiCl + metallic Ni → alloying to Li–Ni alloys (Li_xNi_y) + MACl	SEI containing LiF, LiCl, and organic carbonate species from electrolyte decomposition	May form thicker SEI after cycling; increased R_{SEI}; chloride salt and Ni-rich interphase	170
Cs_4PbBr_6	$LiPF_6$ in EC/DEC (1 : 1)	$Cs_4PbBr_6 + LiPF_6 \rightarrow CsPF_6 + PbBr + LiBr$; $CsPF_6$ unstable → Cs^+ ions released; Cs^+ participates in SEI formation (self-healing electrostatic shielding, SHES) to suppress Li dendrites; Pb^{2+} undergoes partial alloying with Li, not fully reversible → capacity fade	Likely contains LiF, LiBr, Cs-containing species ($CsPF_6$ decomposition products); Pb/Li–Pb alloy fragments; organic electrolyte reduction products	SEI may become Cs-rich; the SHES mechanism promotes uniform Li deposition; Pb centers are trapped in the organic matrix after irreversible alloying	171
Bz–Pb–I (1D hybrid)	1 M $LiPF_6$ in EC/DMC (1 : 1) + 5%	Multi-step alloying resulting in metallic Pb and different Li_xPb alloy formation (Li_8Pb_3, $Li_{22}Pb_5$, LiPb, $Li_{10}Pb_3$, *etc.*)	SEI is LiF-rich *via* FEC; halide residues; organic matrix interfaces	—	172

proposed for Li uptake in perovskites, which are indicated below:

(1) Intercalation mechanism: Vicente *et al.*[167] suggested that there is topotactic Li^+ insertion into perovskites without severe structural alterations, as shown in Fig. 8a. The XPS analysis indicated that no Li–Pb alloying reactions occur (Fig. 8b). However, it was unclear which species are reduced because of Li intercalation, given that the Pb and Br electronic structures remain mostly unchanged.

(2) Conversion mechanism: in the same year, using electrochemical and powder X-ray diffraction techniques, combined with DFT, Dawson *et al.*, proposed that both intercalation and conversion reaction occurs during the charge/discharge cycle. The authors indicated that for all three hybrid perovskites, $MAPbX_3$ (X = Cl, Br, I), the energy for conversion reactions is more favorable than the intercalation reactions. Some main features of their results are indicated below.[166]

(a) There are two possible sites for Li-ion insertion in $MAPbX_3$ (X = I/Br/Cl), octahedral and tetrahedral. Also, the site preference depends on both material and Li-ion concentration.

(b) At low Li-ion concentrations, insertion into $MAPbI_3$ becomes more favorable because it is easier to insert Li into larger $MAPbI_3$, causing less distortion in PbI_6 octahedra.

(c) Upon full Li intercalation ($x = 1.0$), the PbX_6 octahedra displays structural distortion in all three materials, with $MAPbBr_3$ and $MAPbCl_3$ exhibiting the greatest structural distortion. This may indicate the presence of conversion (to lithium halides (LiX) and Pb metal) or decomposition reactions upon full Li-ion interaction.

(d) The Li-ion conversion process is more energetically favorable than the Li-ion intercalation.

In 2019, Vicente *et al.*[168] conducted another study to understand the Li uptake mechanism in $MAPbBr_3$ using *operando*-XRD analysis in conjunction with galvanostatic lithiation (discharge) and delithiation (charge) steps (Fig. 8c and d). The authors identified three reaction stages (lithiated phase, conversion, and alloying) associated with varying Li-ion molar content. However, the mechanism of phase transition during the subsequent cycles was not established. For all-inorganic halide perovskites, *ex situ* XRD patterns of the $CsPbCl_3$ electrode indicated that the preferred mechanism for Li-ion storage in the initial discharge cycle is through conversion reactions rather than Li-ion intercalation.[45] As a result, the disputed and vague findings from the *ex situ* characterizations obscure the understanding of the structural changes of halide perovskites throughout the lithiation and delithiation process. Recently, X.-H. Wu *et al.*[44] utilized *in situ* X-ray diffraction (XRD) and electrochemical impedance spectroscopy (EIS), along with *ex situ* characterizations, to explore the intricate mechanisms of lithium storage and release in $CsPbBr_3$, including the phase transition that occurs during the first three cycles. The findings indicate that at full discharge, $CsPbBr_3$ breaks down into CsBr, LiBr, Pb, and $Li_{22}Pb_5$ phases *via* intercalation–conversion–alloying reactions, followed by the regeneration of $CsPbBr_3$ during the charging process (Fig. 8e).

However, several studies have reported different Li-ion transport mechanisms and SEI formation (shown in Table 2); the precise mechanistic pathways are still a bit of a mystery in this field. This uncertainty largely stems from the intricate structural changes that MHPs undergo during cycling, the diverse range of perovskite compositions (such as lead-based, tin-based, and double perovskites), and the absence of systematic *in situ* characterization under realistic battery conditions. Therefore, this field of research requires further investigation.

3. MHPs in LIBs

Due to the limited theoretical capacity, the risk of short circuits from dendrite formation, and the inadequate ability to sustain continuous high current discharge, currently available graphite anode materials present significant challenges. Consequently, there is a growing need for alternative anode materials that offer higher theoretical capacities, improved cycle stability, and greater cost efficiency.[173,174] In this context, MHPs have recently gained attention as potential anode materials for LIBs. Several researchers have investigated different MHP compositions to develop high-performance anodes capable of replacing conventional graphite-based systems. Beyond their application as anode materials, MHPs have also been employed as ASEI layers on Li-metal anodes (LMAs) to mitigate detrimental side reactions with liquid electrolytes. This section aims to provide a comprehensive overview of the application of various MHPs in LIBs, focusing on their roles as both active anode materials and protective interfacial layers.

3.1. MHP-based anodes in LIBs

3.1.1. 3D MHP-based anodes. As mentioned earlier, the first use of 3D MHPs as anode materials was proposed by Xia *et al.*[43] In 2015, where hydrothermally synthesized $MAPbBr_3$ and $MAPbI_3$ microcrystals displayed a first discharge capacity of nearly 330 mAh g^{-1} and 50 mAh g^{-1} at 200 mA g^{-1} current density (Fig. 9a). Moreover, the cycle stability of $MAPbBr_3$ shows prominent improvement as compared to $MAPbI_3$ (Fig. 9b). While the specific reasons for the enhanced performance of $MAPbBr_3$ based batteries remain unclear, this study suggests that halide perovskites hold promising potential for lithium storage applications. Several years later, research also indicates that the charge/discharge capacity can be enhanced when I^- is replaced with Br ($MAPbBr_3$), as illustrated in Fig. 9c. However, an incomplete substitution of Br^- ($MAPbIBr_2$) leads to a decrease in charge/discharge capacity, as the lattice parameter shifts from tetragonal $MAPbI_3$ to cubic $MAPbBr_3$. This suggests that perovskites with varying halogens exhibit different specific capacities, primarily due to two factors: (1) the influence of halogens on the crystal structures, as we covered in part 3.1, and (2) the competition between the lower atomic mass of Br^- and the larger lattice parameter of I^-. The effect of crystal morphology on the electrochemical performance of $MAPbBr_3$ was investigated by Q. Wang *et al.*[175] In the study, they compared five different microcrystal sizes (~2.9 mm, ~2.4 mm, ~1.9 mm, ~1.5 mm, and ~1.2 mm) and concluded that 1.2 mm-sized $MAPbBr_3$ composite electrodes exhibit unexpectedly high

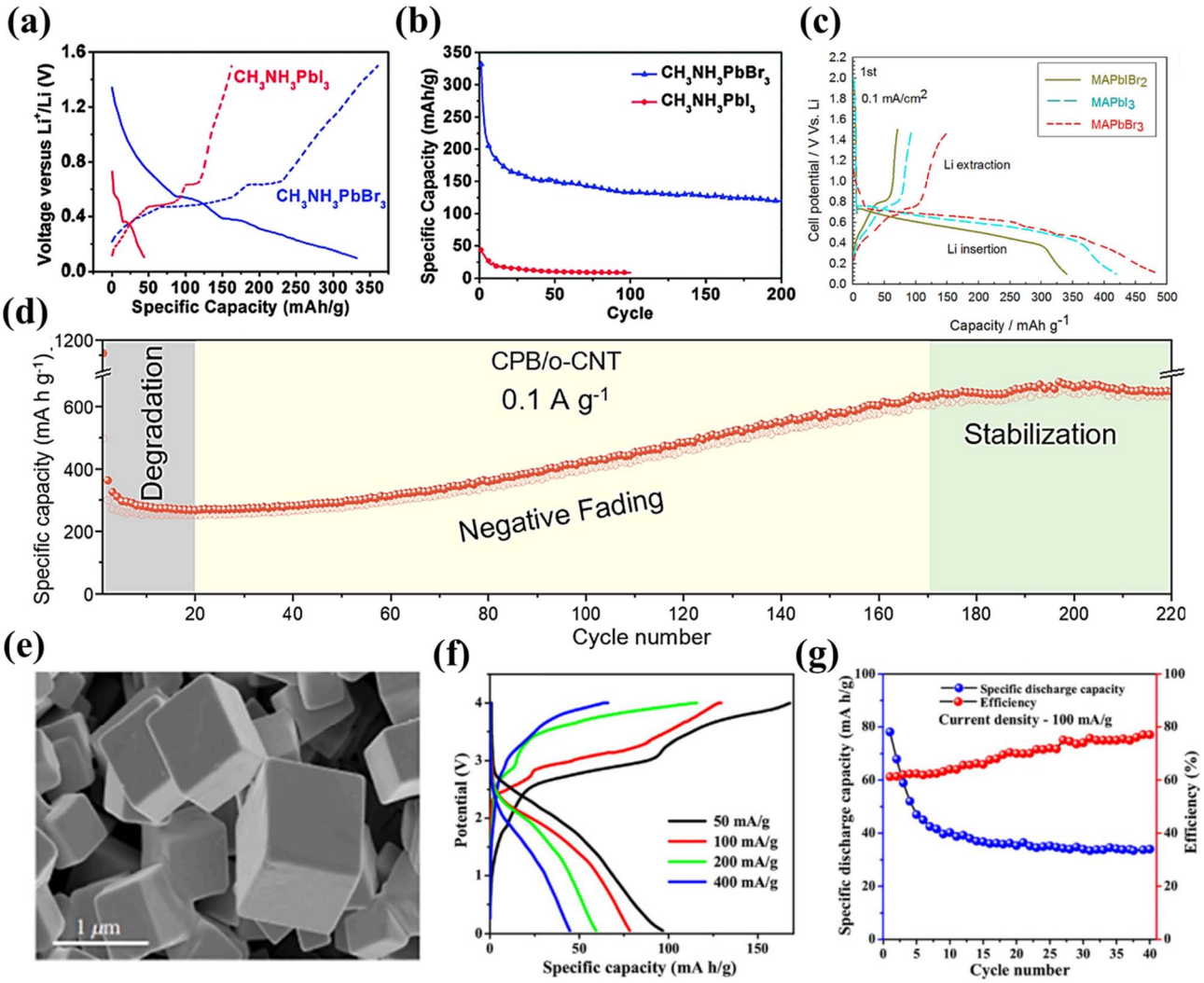

Fig. 9 Electrochemical properties of the LIBs based of $MAPbBr_3$ and $MAPbI_3$: (a) charge/discharge curves, (b) cycle stability[43] Copyright 2015, *Chem. Commun*. (c) Charge/discharge curves of $MAPbI_3$, $MAPbIBr_2$, and $MAPbBr_3$ [169] Copyright 2018, *Inorg. Chem.* (d) The cycling performance of CPB/o-CNT electrode at 0.1 A g^{-1} divided into three regions[44] Copyright 2025, *Energy Storage Mater.* (e) SEM image of cubic $CsPbCl_3$. $CsPbCl_3$–graphite-based dual-ion batteries (f) galvanostatic CD curves at various current densities and (g) discharge capacity retention over 40 CD cycles at a current rate of 100 mA g^{-1} Copyright 2020, *Phys. Rev. Appl.*[45]

cycling stability for more than 1000 cycles when tested as LIB anodes compared to other-sized samples due to high crystal quality and improved electrical conductivity.

As compared to organometallic halide perovskites, all-inorganic halide perovskites showed better stability, ultrahigh photoluminescence quantum yield, *etc.* In this regard, Jiang *et al.* proposed all inorganic $CsPbBr_3$ as an active material for the LIB anode in 2017 with a first charging capacity of 94.8 mAh g^{-1} and the cyclic life of 32 rounds at 60 μA cm^{-2}.[176] In another report, the electrochemical performance and storage capacity were further enhanced by incorporating carbon nanotubes (CNTs), resulting in improved stability and rate capability due to the pseudo-capacitive effect.[177] Moreover, X.-H. Wu *et al.*[44] displays "negative fading" effect and a significant increase in capacity in $CsPbBr_3$@CNT based electrodes. This electrode delivered a specific capacity of 630 mAh g^{-1} at 0.1 Ag^{-1} after 200 cycles (Fig. 9d). In addition to bromide, cubic $CsPbCl_3$ (Fig. 9e) has been developed as an anode for LIB and dual-ion batteries. The findings indicate that the half-cell LIB exhibited specific discharge capacities of 612.3, 508.7, 362.4, and 275.2 mAh g^{-1} at varying current densities of 50, 100, 200, and 250 mA g^{-1}, respectively (Fig. 9f), along with an average coulombic efficiency of 88%. Moreover, the combination of a 3D perovskite anode with a graphitic cathode provided insights into dual-ion batteries operating within a voltage range of 0–4.0 V, averaging 2.53 V, as illustrated in Fig. 9g. The summary of the performance of different MHPs used in LIBs is summarized in Table 3.

3.1.2 Low-dimensional MHPs-based anodes. In contrast to 3D perovskites, lower-dimensional variants are favored for improved lithium storage due to the greater space present in their layered architecture. These low-dimensional perovskites

Table 3 Summary of different MHPs based on LIBs and their performance[a]

Perovskite material	Counter electrode	Electrolyte	Potential range in V (*vs.* Li/Li^+)	Current density	1st cycle capacity (mAh g^{-1})	Discharge capacity after '*n*' cycles (mAh g^{-1})	Ref.
$CsPbCl_3$	$LiFePO_4$	1 M $LiBF_4$ in PVDF-HFP + $BMIMBF_4$ (1 : 3 w/w)	3.60.01-	50 mA g^{-1}	612	~300 (70 cycles)	45
Cs_4PbCl_6 0DPG-A (zero-dimensional glass powder-A)	Li-metal foil	1.0 M $LiPF_6$ in EC/DMC (1 : 1 vol ratio)	0.01–3	5 A g^{-1}	1387.9	510.5 (1000 cycles)	178
$CsPbBr_3$@CNTs	Li-metal disks	1.0 M $LiPF_6$ in EC/DMC (1 : 1 vol ratio)	0.001–3.0	100 mA g^{-1}	644.6	470.2 (200 cycles)	177
$CsPbBr_3$@CNTs	Li	1.0 M $LiPF_6$ in EC/DMC/EMC (1 : 1 : 1 vol ratio)	0.2–3 V	1 A g^{-1}	629	~376 after (900 cycles)	44
$CsPbBr_3$	Li-metal foil	1.0 M LiTFSI in DOL/DME (1 : 1 vol ratio)	2.8–0.05	60 μA cm^{-2}	102.6	~73.8 after (32 cycles)	176
$CsPbBr_3$	Li-metal foil	LiTFSI + BMIMTFSI film	3.0–0	60 mA g^{-1}	259	~200 (100 cycles)	179
Cs_4PbBr_6 0DPG-A	Li-metal foil	1.0 M $LiPF_6$ in EC/DMC (1 : 1 vol ratio)	0.01–3.0	5 A g^{-1}	195	429.6 (1000 cycles)	178
$CsPbI_3$	Li-metal foil	1.0 M $LiPF_6$ in a EC/DMC (1 : 1 vol ratio)	0.1–3	40 mA g^{-1}	151	235 (100 cycles)	46
Cs_4PbI_6 0DPG-A	Li-metal foil	1.0 M $LiPF_6$ in EC/DMC (1 : 1 vol ratio)	0.01–3.0	5 A g^{-1}	1589.7	36.1 (1000 cycles)	178
$MAPbI_3$	Li-metal foil	1.0 M $LiPF_6$ in EC/DMC/EMC (1 : 1 : 1 vol ratio)	0.1–1.5	200 mA g^{-1}	43.6	9 (200 cycles)	43
$MAPbI_3$	Li-metal foil	$LiPF_6$ in EC/DMC (1 : 1 vol ratio)	0.01–2.5	100 mA g^{-1}	476	202 (50 cycles)	172
$MAPbI_3$/ITO	Li-metal foil	1.0 M $LiPF_6$ in EC/DEC (1 : 1) vol ratio)	1.5–0.1	0.1 mA cm^{-2}	~340	~50 (10 cycles)	169
$MAPbBr_3$	Li-metal foil	1.0 M $LiPF_6$ EC/DMC	0.01–2.5	300 mA g^{-1}	158.2	120.1 (200 cycles)	175
$MAPbBr_3$	Li sheet	$LiPF_6$ in EC/DMC	0.1–1.5	300 mA g^{-1}	480	50 (10 cycles)	169
$MAPbBr_3$	Li	5 M LiTFSI in EC/PC	0.1–2.7	30 mA g^{-1}	~510	80 (100 cycles)	180
$MAPbBr_3$	Li	$LiPF_6$ in EC/EMC/DMC (1 : 1 : 1 vol ratio)	0.1–1.8	50 mA g^{-1}	~600	260 (50 cycles)	167
$MAPbBr_3$	Li-metal	$LiPF_6$ in EC/EMC/DMC(1 : 1 : 1 vol ratio)	0.2–1.4	200 mA g^{-1}	331.8	121 (200 cycles)	43
$MAPbIBr_2$/ITO	Li-metal foil	1.0 M $LiPF_6$ in EC/DEC (1 : 1) vol ratio)	1.5–1.0	0.1 mA cm^{-2}	~425	~50 (10 cycles)	169
$MANiCl_3$	Li-metal foil	1.2 M $LiPF_6$ in EC/DMC (1 : 1) vol ratio)	0.1–3.5	0.1 mA g^{-1}	170	~120 (50 cycles)	181
$MANiCl_3$	Li-metal foil	1.0 M $LiPF_6$ in EC/DMC (1 : 1) vol ratio)	0.1–2.7	~32 mA g^{-1}	650	350 (19 cycles)	170
$Cs_2NaErCl_6$	Li-metal foil	1.0 M $LiPF_6$ in EC/DMC/EMC (1 : 1 : 1 vol ratio)	0.1–2.5	300 mA g^{-1}	522	120 (500 cycles)	5
$MA_2(CH_3(CH_2)_2NH_3)_2Pb_3Br_{10}$	Li-metal foil	1.0 M $LiPF_6$ in EC/DEC (1 : 1 vol ratio)	0.1–1.2	0.1 mA cm^{-2}	375	—	169
Cs_4PbBr_6	Li-metal foil	1.0 M $LiPF_6$ in EC/DEC (1 : 1 vol ratio)	0.01–3	0.5 A g^{-1}	158.6	136.5 (1000 cycles)	182
SnF_2-doped Cs_4PbBr_6 (FLII glass matrix)	Li-metal	—	0–2.0	0.5 A g^{-1}	773	741 (350 cycles)	183
$(C_4H_9NH_3)_2PbI_4$	Li-metal	1 M $LiPF_6$ in an EC/DMC e (1: 1 vol ratio) with 5% FEC	0.01–2.5	100 mA g^{-1}	1605	213 (250 cycles)	172
Cs_4PbBr_6 quantum dots silicate glass-ceramic	Li-metal foil	1.0 M $LiPF_6$ in EC/DEC (1 : 1 vol ratio)	0 to 3	50 mA g^{-1}	1986.9	426.7 (100 cycles)	184
C_6H_9NOPb	Li-metal foil	1 M $LiPF_6$ in EC/DEC (1 : 1 vol ratio) with 5% FEC	2.5–0.01	100 mA g^{-1}	1580	585 (50 cycles)	172
$Li_2(taurine)_2CuCl_4$ (LTCC)	Li-metal foil	1 M $LiPF_6$ in EC/DEC/DMC 1 : 1 : 1 vol ratio) + 5% FEC	0.005–3.0	1.0 A g^{-1}	—	548 mAh g^{-1} (550 cycles)	185
$C_4H_{20}N_4PbBr_6$	Li-metal foil	1.0 M $LiPF_6$ EC/DMC/EMC (1 : 1 : 1 vol ratio)	0.1–2.5	150 mA g^{-1}	1632.8	598.0 (50 cycles)	186
$(BA)_2(MA)_3Pb_4Br_{13}$	Li-metal foil	5 M LiTFSI in 1 mL EC/PC (1 : 1 vol ratio)	2.8–1.8	30 mA g^{-1}	108	~42 (10 cycles)	180
Mn-substituted $Cs_3Bi_2Cl_9$	Li-foil	1.0 M $LiPF_6$ in EC/DMC/EMC (1 : 1 : 1 vol ratio)	0.1–2.5	100 mA g^{-1}	467	117.08 (500 cycles)	187
Cs_4PbBr_6 nano hexagons/ITO	Pt	LiCl	−1 to +0.1	45 mA g^{-1}	377	—	188
$Cs_2NaBiCl_6$	Li-metal foil	1.0 M $LiPF_6$ in EC/DMC/EMC (1 : 1 : 1 vol ratio)	0.01–2.5	75 mA g^{-1}	~775	300 (25 cycles)	189
$Cs_2NaBiCl_6$:xMn^{2+}	Li-metal foil	1.0 M $LiPF_6$ in EC/DMC/EC (1 : 1 : 1 vol ratio)	0.01–2.5V	70 mA g^{-1}	—	240 (300 cycles)	190

[a] Li-salt and solvent abbreviations in the electrolytes reported: $LiPF_6$ = lithium hexafluorophosphate, $LiBF_6$ = lithium tetrafluoroborate, LiTFSI = lithium bis(trifluoromethanesulfonyl)imide, LiCl = lithium chloride. EC = ethylene carbonate; DMC = dimethyl carbonate; DEC = diethyl carbonate; EMC = ethyl methyl carbonate; PC = propylene carbonate; DOL = 1,3-dioxolane; DME = dimethoxyethane.

can enhance capacity and provide better reversibility than their 3D counterparts. The effect of dimensionality on electrochemical properties was first investigated in 2017 by Tathavadekar *et al.*[172] They discovered that lowering the dimensionality of perovskites was effective in improving the lithium storage. They used 1D $C_6H_9I_3NOPb$, 2D $(C_4H_9NH_3)_2PbI_4$, and 3D $MAPbI_3$ perovskites and revealed that the first discharge capacity for 1D and 2D perovskites is nearly 4 times higher than the 3D perovskite, making them potential active materials for anodes in LIBs (Fig. 10a). Similar results have been reported by Hong Kong *et al.*[186] in 2022, they fabricated three different dimensional perovskites as anodes in the Li-ion battery. Among the anodes, the 1D $C_4H_{20}N_4PbBr_6$-based one offers the best performance, providing a stable capacity value of 598.0 mAh g^{-1} (Fig. 10b–d). The reason for this is that 2D and 1D perovskites have a greater spacing between crystal planes than close-packed 3D structures, which allows more Li-ions to intercalate. As a type of low-dimensional material, RP perovskites possess a quasi-2D structure, which allows for the optimization of energy storage capacity through the arrangement of layers. De Volder *et al.*[180] examined the electrochemical capacity and cyclic stability of a series of $(BA)_2(MA)_{n-1}Pb_nX_{3n+1}$ as anodes for LIBs by adjusting the n values (Fig. 10e and f). It is evident from Fig. 10g that the sample with $n = 4$ exhibited the best performance in terms of battery capacity, while a noticeable decline in capacity was observed as per units increased. And the spacer layers that facilitate ion diffusion and provide structural constraint. Recently, Maity *et al.* compared the electrochemical performance of 3D MHP (CsMAPbIBr) and the 2D–3D hybrid MHP (CsMABPAPbIBr) as shown in Fig. 10h.[171] They demonstrated that the mixed

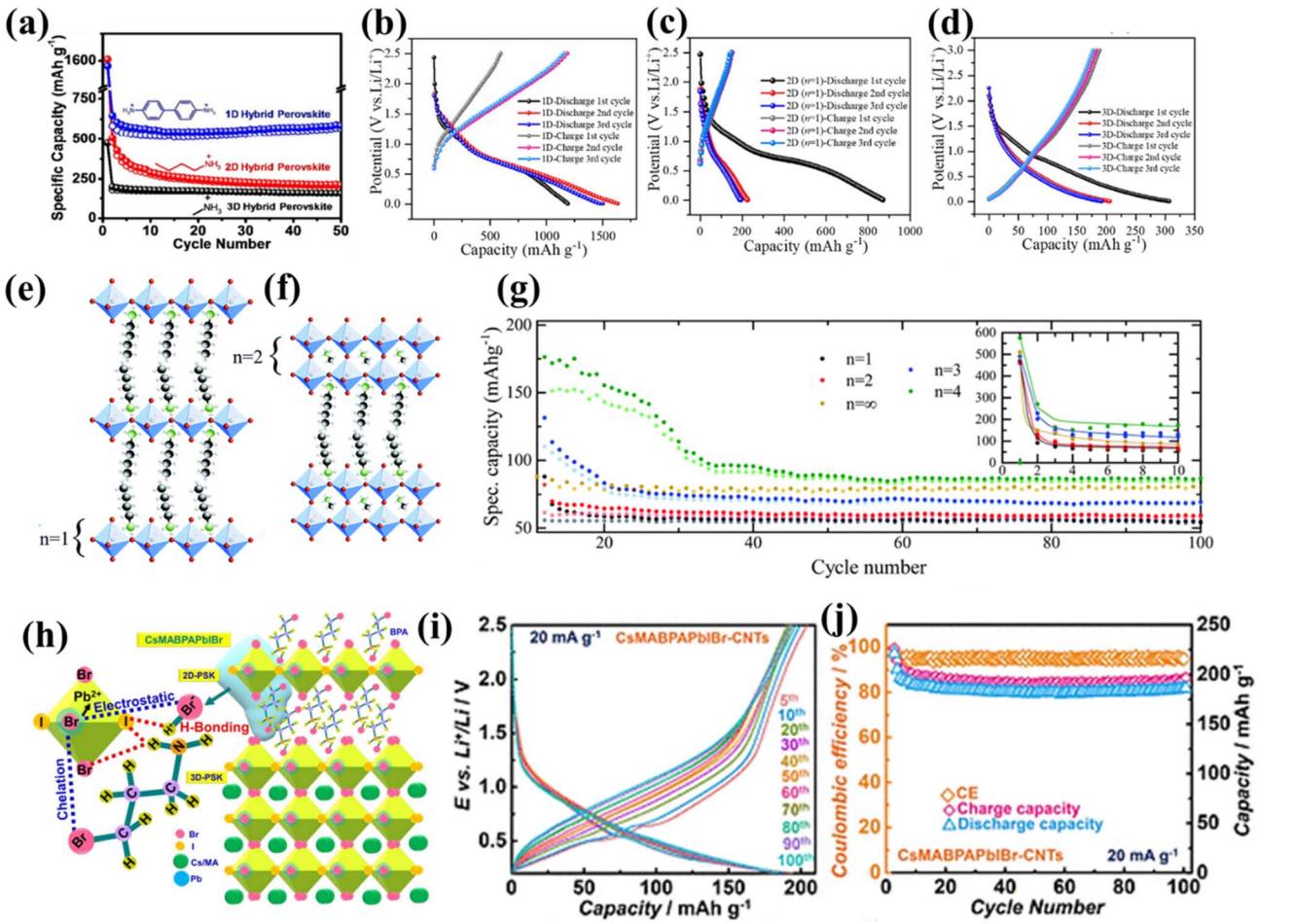

Fig. 10 (a) Cyclic stability for 1–2–3 D hybrid perovskite at a current density of 100 mA g^{-1} in the potential window of 2.5–0.01 V[172] Copyright 2017, *J. Mater. Chem. A* Galvanostatic charge–discharge profiles of first three cycles of (b–d) 1D, 2D and 3D perovskite at a current density of 100 mA g^{-1} between 0.01 and 2.50 V[186] Copyright 2022, *J. Energy Chem.* (e) Quasi 2D $(BA)_2(MA)_{n-1}M_nX_{3n+1}$ ($n = 1$) perovskite structure with individual layers of PbX_4 intercalated between two BA organic chains. (f) $n = 2$-layered perovskite structure. (g) Gravimetric charge–discharge capacities of the bromide-based layered perovskite $(BA)_2(MA)_{n-1}Pb_nBr_{3n+1}$ from $n = 1$–$n = 4$ and the respective bulk $MAPbBr_3$ perovskite (equivalent in structure to $n = \infty$) as a function of cycle number from cycle 11–100; the first 10 cycles are highlighted inset. Specific charge capacities are shown shaded and specific discharge capacities block colour. A current density of 30 mA g^{-1} and a potential window of 2.85–0.1 V are used[180] Copyright 2021, *Mater. Adv.* (h) Schematic structure of 2D–3D hybrid PSK (CsMABPAPbIBr), showing the interactions between Br(Pr) $NH_2{\cdot}HBr$ and the unit cell of the PSK (perovskite). (i) GCD plots acquired intermittently during cycling at 20 mA g^{-1}, (j) capacity/CE variation with cycling[171] Copyright 2025, *ACS Appl. Energy Mater.*

Table 4 Comparison of energy density and cycle life of different MHPs in LIBs

Perovskite material	Year of publication	First discharge capacity (mAh g^{-1})	Average voltage (V)	First discharge energy density (Wh kg^{-1})	Stable capacity (mAh g^{-1})	Stable energy density (Wh kg^{-1})	Cycling life	Ref.
$CsPbCl_3$	2020	612	1.805	1105.26	~300	541.50	70 cycles	45
$CsPbBr_3$@CNT	2025	~640	1.50	961.6	376	564	900 cycles	44
$CsPbBr_3$	2021	259	1.5	388.5	~200	300	100 cycles	179
$CsPbI_3$	2021	151	1.55	234	235	364	100 cycles	46
$MAPbI_3$	2017	476	1.255	597	202	254	50 cycles	169
$MAPbBr_3$	2021	~510	1.4	714	80	112	100 cycles	180
$MAPbBr_3$	2015	331.8	0.8	265.4	121	96.8	200 cycles	43
$MANiCl_3$	2024	170	1.8	306	~120	216	50 cycles	181
$MANiCl_3$	2020	650	1.4	910	350	490	19 cycles	170
Cs_4PbCl_6 0DPG-A	2022	1387.9	1.505	2088.8	510.5	768.3	1000 cycles	178
Cs_4PbI_6 0DPG-A	2022	1589.7	1.505	2392.5	36.1	54.3	1000 cycles	178
Cs_4PbBr_6 0DPG-A	2022	195	1.505	293.5	429.6	646.5	1000 cycles	178
$MA_2(CH_3(CH_2)_2NH_3)_2Pb_3Br_{10}$	2018	375	0.65	243.8	—	—	—	180
$(C_4H_9NH_3)_2PbI_4$	2017	1605	1.25	2014.3	213	267.3	250 cycles	172
C_6H_9NOPb	2017	1580	1.25	1982.9	585	734.2	50 cycles	172
Li_2(taurine)$_2CuCl_4$ (LTCC)	2025	—	1.5	—	548	823.4	550 cycles	185
$C_4H_{20}N_4PbBr_6$	2022	1632.8	1.3	2122.6	598.0	777.4	50 cycles	186
$(BA)_2(MA)_3Pb_4Br_{13}$	2021	108	2.3	248.4	~42	96.6	10 cycles	180
Mn-substituted $Cs_3Bi_2Cl_9$	2025	467	1.3	607.1	117.08	152.2	500 cycles	187
$Cs_2NaBiCl_6$	2021	775	1.25	972.6	300	376.5	25 cycles	189
$Cs_2NaErCl_6$	2022	300	1.3	390	120	156	500 cycles	5
Cs_4PbBr_6 quantum dots silicate glass-ceramic	2022	1986.9	1.5	2980.35	426.7	640.05	100 cycles	184

dimensionality furnishes more accessible sites for Li-ions compared to the control 3D MHP (CsMAPbIBr), thereby increasing both capacity and rate capability. Li-ion cells utilizing the 2D–3D hybrid MHP–CNTs composite demonstrated an outstanding discharge capacity of 221 mAh g^{-1}, an energy density of 508 Wh kg^{-1}, and 84% of capacity retention after 100 cycles, marking a significant enhancement compared to 3D MHP–CNTs (Fig. 10i and j). Due to the environmental issues associated with Pb-based perovskites stemming from the recognized toxicity of lead, it is crucial to establish stable lead-free perovskite alternatives for LIBs. Research focused on lead-free perovskite materials and their photoelectric applications has shown that lead-free perovskites featuring intricate crystal structures are capable of accommodating defects and intercalated ions, which could lead to effective Li-ion storage.[191,192] Pandey *et al.*[193] reported that the 2D $(MA)_2CuBr_4$ and 3D Cs_2CuBr_4 possess a reversible capacity of ~480mAh g^{-1} and 420 mAh g^{-1}, respectively. In their study, it was observed that 2D material capacity increased gradually with subsequent charge–discharge cycles, achieving 630 mAh g^{-1} at 140 cycles. The reason for this observation stems from the slow percolation of electrolyte into the electrode as well as the appearance of Li-ion intercalation sites in response to cycling. Similarly, Yang and coworkers introduced lead-free all-inorganic double perovskite $Cs_2NaBiCl_6$ [188] and $Cs_2NaErCl_6$ [5] as anode material for LIB. It was revealed that $Cs_2NaBiCl_6$-based battery properties are not beneficial, especially poor battery cycle stability, which limits their practical use. Nevertheless, $Cs_2NaErCl_6$ as a negative electrode material showed high cycle stability, with a specific capacity of 120 mAh g^{-1} after 500 cycles at a current density of 300 mA g^{-1} with a Coulomb efficiency of nearly 100%. Recently, a new class of low-dimensional lead-free $Cs_3Bi_2Cl_9$ was synthesized by Jia *et al.*[187] The authors demonstrated that the initial discharge specific capacity can be enhanced from 263.39 mAh g^{-1} to 467 mAh g^{-1} and stabilized to values from 89.32 mAh g^{-1} to 125.3 mAh g^{-1} after 100 cycles, with a coulombic efficiency of more than 99%, and stabilized at 117.08 mAh g^{-1} after 500 cycles. Recently, Wu *et al.*[185] presented a layered perovskite $Li_2(C_2H_7NO_3S)_2CuCl_4$ (LTCC). The LTCC anode can achieve a remarkable specific capacity of 861 mAh g^{-1} at 0.1 A g^{-1} after 100 cycles. Moreover, it retains a high discharge capacity of 548 mAh g^{-1} over 550 cycles at 1.0 A g^{-1}, exhibiting outstanding cycling stability among perovskite-type anode materials for LIBs. However, compared to traditional 3D perovskites, there is a limited number of studies on low-dimensional, lead-free, and non-perovskite MHPs in LIBs. Nevertheless, emerging research in this area highlights significant potential for future exploration and development. The quantitative comparison of energy density and cycle life of different MHPs in LIBs is given in Table 4.

3.2. MHPs as ASEI

The major issue with Li-metal batteries (LMBs) is the self-derived unstable SEI, which possesses low Li^+ conductivity, low mechanical modulus, and inhomogeneous composition, which makes it difficult to achieve smooth and stable deposition/stripping of Li metal anode.[194] Due to an inhomogeneous SEI, a non-uniform Li deposition will result, which facilitates the formation of Li dendrites. Li dendrites are capable of piercing low mechanical modulus SEI, leading to the formation of new SEIs derived from Li metal reactions with electrolytes. During Li stripping, Li dendrites are likely to isolate from the Li bulk and turn into "dead'' Li, resulting in low coulombic efficiency. After repeated cycling, the dendrites may grow to several hundred microns and penetrate the separators, causing short circuits and safety hazards.[195] In this regard, researchers are exploring various strategies for inhibiting dendrite growth: (a) Li-alloy anodes,[196] (b) solid-state electrolyte,[197] (c) structured anodes,[195] (d) ASEI,[198] (e) electrolyte additives,[199] and (f) interface modifications.[200] Among them, one of the most effective approaches to inhibit dendrite problems has been reported to be regulating Li-ion distribution *via* the application of an artificial protective layer on the electrode surface, which reduces current density and strengthens the electrode/electrolyte interface stability.[201] So far, a variety of protective materials, including inorganics, polymers, and hybrids, have been applied to LMAs through various deposition methods, such as solid gas reactions, atomic layer deposition, or wet chemical emulsion coating.[202–204]

Choosing the materials for ASEI coating depends on the preparation conditions of thin films on LMAs, as well as the properties of the materials, such as stability against electrolytes, electron insulation, high Li-ion conduction, and flexibility confirm the changes in the volume of the lithium anode.[201] Currently used materials for SEI are capable of effectively separating LMAs from electrolytes and preventing spontaneous side reactions. However, structural stability and high ion conductivity are incompatible, which makes Li plating/stripping tough, further restricting LMB capacity and long-term performance. It is therefore highly desirable to develop ASEI materials that have good structural stability and Li-ion conductivity.[205]

Due to its adjustable 3D framework structure and bandgap, MHPs can achieve Li-ion conduction and electronic insulation, which is expected to become a promising candidate for constructing a high-performance SEI layer. In 2020, an interfacial layer composed of solution-processed $MASnCl_3$ and $MAPbCl_3$ perovskites was developed by Yin *et al.*[47] as a new type of interfacial layer for the LMA through a solid-state transfer process. They demonstrated through galvanostatic Li plating and stripping that MSC-Li cell can be cycled for more than 800 h, much longer than the 100 h cycling life of the cell using bare Li (Fig. 11a). They also evaluated the electrochemical performance of $Li_4Ti_5O_{12}$ (LTO)/perovskite coated Li metal batteries at a high rate of 5C to demonstrate the efficiency of perovskite protection in LMBs. It was shown that the bare Li metal anodes exhibit a drastic capacity decay, with a capacity of 28.3 mAh g^{-1} at the 400th cycle. In contrast, the cells using $MASnCl_3$ and $MAPbCl_3$ coated LMA show stable cycling for more than 500 cycles with a low capacity decay rate of 0.07% per cycle (Fig. 11b). It was concluded that the metal chloride perovskite protection layer can ensure stable cycling of LMBs under strict conditions. Furthermore, based on DFT calculations, the researchers proposed a Li-ion transport gradient layer

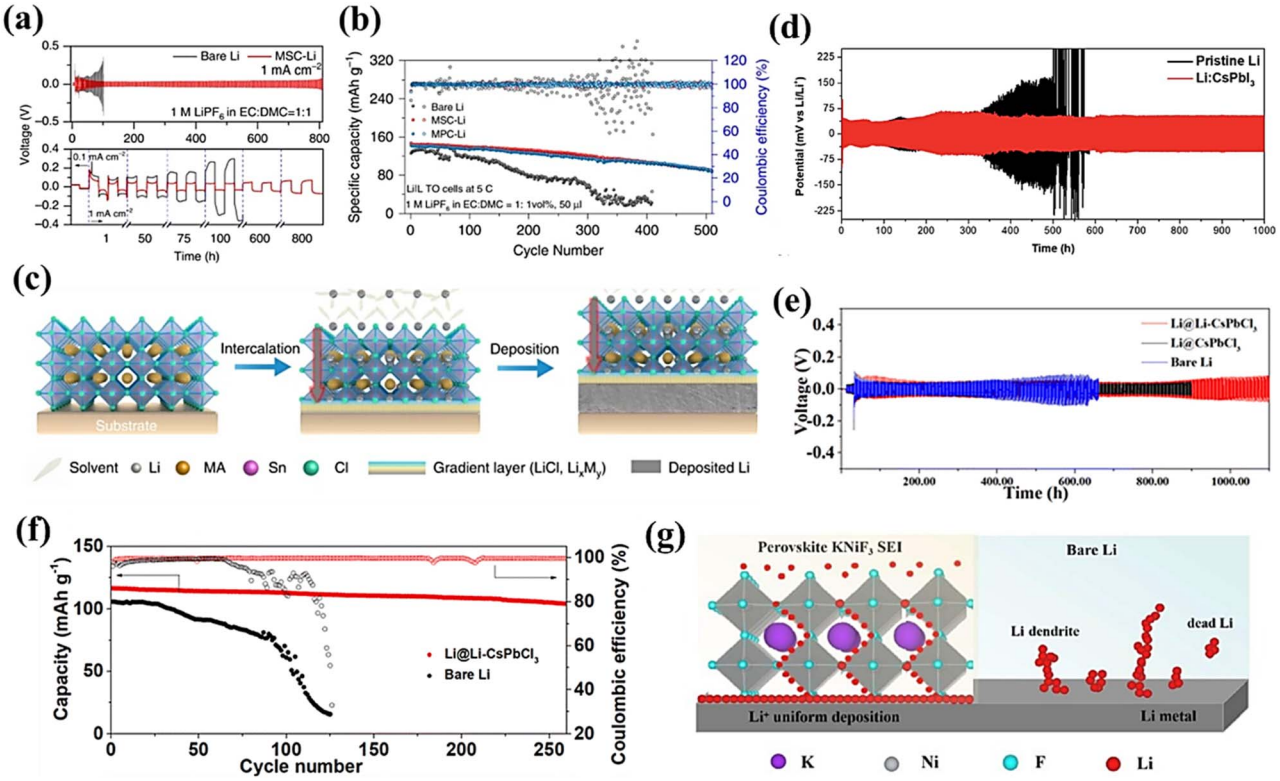

Fig. 11 (a) Galvanostatic voltage curves (top) of bare Li and MSC-Li tested with a current density of 1 mA cm^{-2} for 1 mAh cm^{-2}, and the enlarged voltage curves during different periods (bottom). (b) Galvanostatic cycling performances of cells using LTO as cathode and bare Li, MSC-Li or MPC-Li as anode. (c) Schematic illustration of the mechanism of Li-ions' intercalation into perovskite lattice, the formation of perovskite-alloy gradient Li-ion conductor, and the deposition process[47] Copyright 2020, *Nat. Commun.* (d) Voltage profiles of pristine Li and Li: $CsPbI_3$ symmetric cells measured at a current density of 1 mA cm^{-2} and a discharge capacity of 1 mA h cm^{-2} [206] Copyright 2020, *J. Mater. Chem. A* (e) Voltage–time curves of Li/Li and Li@Li–$CsPbCl_3$/Li@Li–$CsPbCl_3$ symmetric cells with an areal capacity of 1 mAh cm^{-2} at a current density of 1 mA cm^{-2}. (f) Long-term cycling stabilities of Li/$LiFePO_4$ cells with bare Li and Li@ Li@Li–$CsPbCl_3$ anodes at a current density of 3C[48] Copyright 2024, *Energy Adv.* (g) Schematic illustration of Li plating on $KNiF_3$ perovskite SEI through octahedral structure and on bare Li[205] Copyright 2022, *Chem. Eng. J.*

model that illustrated the shielding mechanism for dense deposition of Li-metal using perovskite thin films, shown in Fig. 11c.

Step 1: only Li-ions absorption within the perovskite framework, leaving solvent molecules outside the perovskite framework.

Step 2: intercalation and migration of Li-ions into the highly symmetric perovskite framework.

Step 3: electrochemical conversion reaction at the interface of the perovskite layer and the substrate.

Step 4: formation of both the insulating LiCl layer and the Li–M alloy layer. A Li–M layer will facilitate homogeneous Li deposition. Nevertheless, the generated LiCl can insulate electrons, preventing the perovskite from further conversion reactions, ensuring that the perovskite remains stable in its top state.

In the same year, Kaisar *et al.*[206] fabricated δ-$CsPbI_3$ as an electrochemical intercalation layer through an inexpensive and facile spray-coating method that stabilizes Li electrodes for LMBs. DFT calculations confirmed the Li-ion intercalation into the δ-$CsPbI_3$ framework, forming Li:$CsPbI_3$. Electrochemical testing of a Li:$CsPbI_3$ symmetric cell revealed dendrite-free plating after 1000 h at a current density of 1 mA cm^{-2} and discharge capacity of 1 mAh cm^{-2} (Fig. 11d). In this new and simple method, derogatory dendrites are avoided, thereby enabling the preparation of LMAs for practical application in high-density LMBs. Recently, Liu *et al.* developed lithium-doped $CsPbCl_3$ ASEI. They demonstrated that Li–$CsPbCl_3$ not only successfully inhibits the formation of lithium dendrites but also promotes the movement of Li-ions at the interface and encourages the ultra-dense and even deposition of Li, creating a beneficial setting for stable Li electroplating/stripping and greatly enhancing the electrochemical performance of LMBs (Fig. 11e and f). However, hybrid perovskites such as $MAPbCl_3$ and $MASnCl_3$ are prone to decomposition when exposed to photo-, thermal-, or moisture-stresses.[207,208] Furthermore, the cubic phase of $CsPbI_3$ is thermodynamically unstable at room temperature, which may result in a blocking of Li-ion transfer channels.[209] In addition to that, lead-based perovskites are highly toxic, which makes them unsuitable for LMBs. Therefore, perovskite materials that are non-toxic and have a high moisture- and thermal stability would be better suited to Li-metal SEI. In this regard, Y. Zhang *et al.*[205] developed air-stable fluoride perovskite ($KNiF_3$), which is applied as an SEI layer to

induce uniform Li-ion deposition for an air-stable and dendrite-free LMA. In their study, they demonstrated that symmetric cells protected by $KNiF_3$ SEI maintain high cycling stability over a period of 3000 hours at a capacity of 4 mAh cm^{-2}. When coupled with commercial $LiFePO_4$ cathodes (LFP, 13.3 mg cm^{-2}), LFP‖Li–$KNiF_3$ batteries show promoted cycling stability and rate capability, much better than the bare Li. Even though MHPs are capable of improving cycling performance, rate capability, and stability. Moreover, they also reveal the protection mechanism of the perovskite SEI through DFT calculation. They demonstrated that Li-ion migrated along the octahedral structure of the perovskite while maintaining the 3D cubic framework without decomposition or phase transition (Fig. 11g).

4. MHPs-based photo-induced LIBs

It is essential to integrate energy storage systems with photovoltaic technology to efficiently and widely utilize solar energy. Conventional photo-rechargeable batteries are made up of a photovoltaic cell and a storage battery, which are separate systems linked by an external wire (Fig. 12a).[210] Nevertheless, this type of system is known for its high expense, size, and various other issues.[42] To address this problem, integrated photovoltaic rechargeable batteries were developed that, unlike non-integrated systems, merge solar energy collection and storage into one device, potentially resulting in more efficient and streamlined solutions.[211] These integrated systems can be implemented in two configurations:[51]

(a) Three-electrode system: this type of system includes a photoelectrode for light conversion, a counter electrode for storing energy, and a common electrode (as a positive or negative electrode) between the photovoltaic cell and the battery (Fig. 12b).

(b) Two-electrode system: the positive electrode has an integrated function, *i.e.*, both photoconversion and energy storage (Fig. 12c).

In this section, we will be discussing the configuration and working principle of photo-induced batteries, followed by the role of MHPs in photo-induced LIBs.

4.1. Working principle

The fundamental operating principle of a photo-battery remains largely consistent, regardless of the type or configuration of the device. When illuminated, the photo-active electrode produces electron–hole pairs as a result of the photovoltaic effect. The electrons and holes generated play a role in the reactions that take place during the charge and discharge cycle. During the charging process (Fig. 12b), a link is formed between the external circuit and both the anode and photoelectrode.

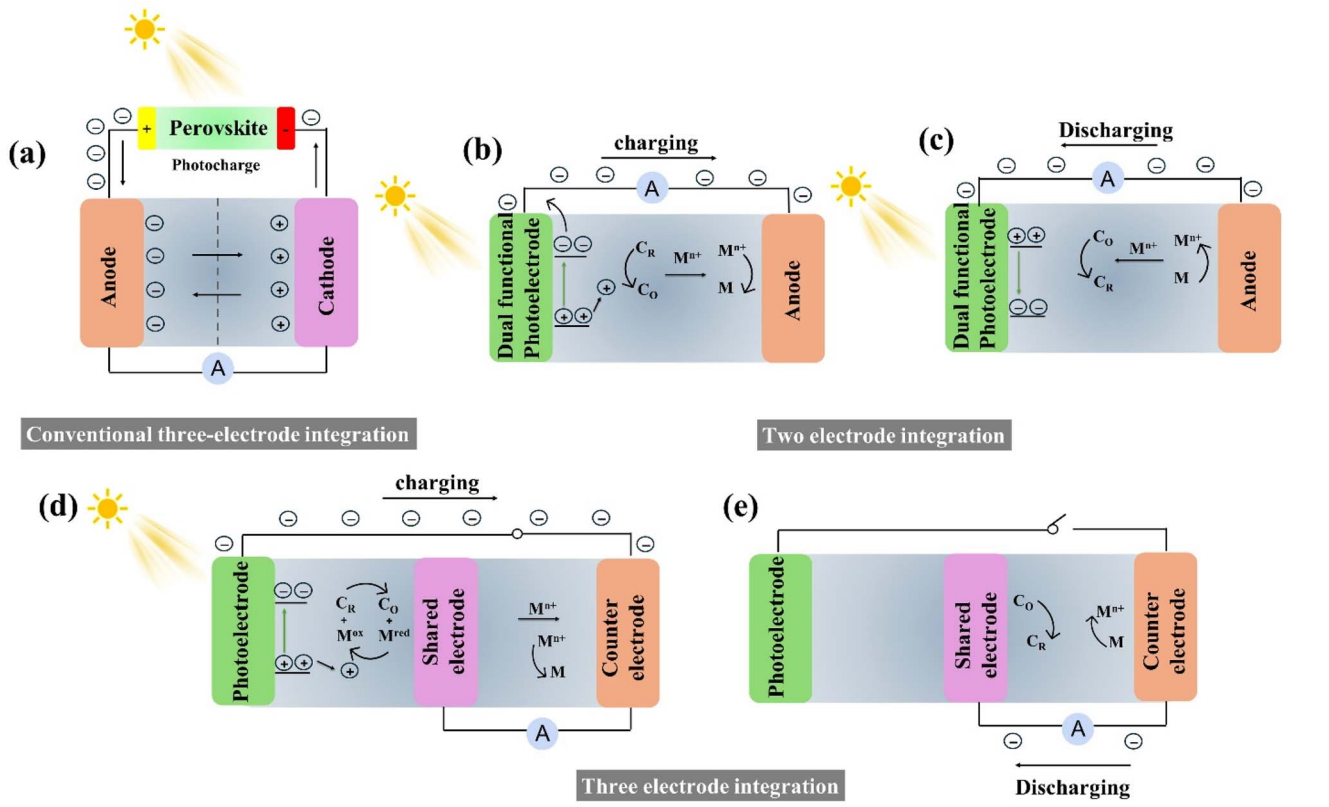

Fig. 12 Working principle of the photo-assisted energy storage device (a) conventional three electrode system[210] reproduced with permission 2024, *Adv. Funct. Mater.*, (b and c) the charging and discharging process of a two-electrode device. (d and e) The charging and discharging process of a three-electrode device[211] reproduced with permission 2024, *Nano Energy*.

When the photoelectrode material is exposed to light, it gets excited, generating high-energy photoelectrons that jump from the VB of the semiconductor to the CB. Concurrently, positive holes are created in the VB of the material. As these holes migrate to the outer layer of the active material on the photoelectrode/cathode side, an oxidation reaction takes place. In this reaction, the reduction product from the photoelectrode (C_R) transforms into the oxidation product (C_O), as demonstrated by the following equation:

$$C_R + h^+ \rightarrow C_o \quad (3)$$

At the same time, the photoelectrons originating from the VB of the semiconductor will move through the external circuit toward the anode and interact with the migrating metal ions M^{n+} from the cathode side. This interaction leads to a reduction reaction that restores the metal M, as depicted in the following equation:

$$M^{n+} + e^- \rightarrow M \quad (4)$$

As a result, the battery device converts electrical energy into chemical energy, which is subsequently stored.

During the discharge process (Fig. 12c), a link is formed between the photoelectrode and the anode to enable integration with the external load. Photoelectrons that are excited on the surface of the semiconductor engage in a reduction reaction with the charging product (C_O) from the photoelectrode, resulting in the production of the discharge product (C_R), as indicated in eqn (5). At the same time, the photo-holes interact with the electrons released from the oxidation reaction taking place on the anode side, leading to their recombination, as illustrated by the eqn (6):

$$C_O + e^- \rightarrow C_R \quad (5)$$

$$M \rightarrow M^{n+} + e^- \quad (6)$$

In this procedure, chemical energy is converted into electrical energy and discharged to supply power to the external load. In more intricate three-electrode systems, the photo-assisted charging mode frequently entails a multi-step reaction occurring at the shared electrode side. This reaction involves additional holes to oxidize the shuttle mediator, as shown in eqn (7)

$$M^{red} + h^+ \rightarrow M^{ox} \quad (7)$$

Then M^{ox} will oxidize the reduction product (C_R) as shown in eqn (8)

$$M^{ox} + C_R \rightarrow C_o + M^{red} \quad (8)$$

Solar energy is stored as chemical energy in the form of C_o at the photoelectrode and the M^{red} at the counter electrode. During the discharge process (Fig. 12e), the M^{red} is oxidized, and electrons are transferred from the external circuit to the shared electrode. Simultaneously, the C_o reduced back to its reduced state. This completed the charge–discharge cycle of the integrated three-electrode photo-rechargeable battery.

4.2. Role of MHPs in photo-induced batteries

Perovskite halides have become significant in the domains of photovoltaics and energy storage, and they are now being explored as photoactive materials for photo-batteries. This is due to the same characteristics that make them suitable for photovoltaic technologies and batteries: an adjustable bandgap, high mobility of charge carriers, a low rate of non-radiative recombination, an extensive absorption spectrum, long charge diffusion lengths, and minor effective masses of carriers, as previously mentioned. Connecting a LIB directly to a solar cell allows for self-charging capabilities. Solar cells are capable of converting solar energy into electrical energy, which can then be stored in LIBs for later use. In a study by Dai *et al.*,[41] a PSC was directly linked to four individual $MAPbI_3$ packs with a LIB, achieving a notable overall conversion and storage efficiency of 7.80% along with outstanding cycling stability. Nevertheless, external photo-rechargeable batteries have several drawbacks, including the tendency to incur ohmic loss during energy transfer between solar cells and storage batteries, as well as their bulky size and high expense, which do not align with the evolving needs of portable electronic devices. As a result, integrated photo-rechargeable batteries have increasingly emerged as a focal point for research. In this regard, Ahmad *et al.*[212] explored the application of 2D lead-based perovskites, specifically $(PEA)_2PbI_4$ (PEA = $C_6H_9C_2H_4NH_3$) (Fig. 13a and b), as a photo-active electrode material for LIBs. The battery utilizing the iodide perovskite achieved a specific capacity of up to 100 mAh g^{-1} at a current rate of 30 mA g^{-1}. Incorporating reduced graphene oxide (rGO) as a conductive additive enabled it to demonstrate photo-charging when illuminated, without needing an external load, across a voltage range of 1.4–3.0 V. This was then succeeded by a 25-hour discharge period with a 21.5 kΩ resistor acting as the load, thus allowing the device to operate as a genuine photo-battery. When the voltage range was lowered to below 1.4 V, the perovskite experienced irreversible degradation due to the reduction of Pb^{2+} to Pb^0. Additionally, the battery provided a higher voltage output when discharged in light compared to darkness. With a 21.5 kΩ resistor as the load, Ahmad *et al.* recorded a photo-conversion efficiency of 0.034%. Additionally, He *et al.*[213] proposed a hypothesis involving polarons to clarify the process of photo-rechargeability in the $(PEA)_2PbI_4$ perovskite system. Importantly, the movement of the Li-ion is indicated to occur following the formation of a hole polaron, which is believed to reflect the photo-charging activity that triggers the one-way flow of Li-ions on the surface of the electrode. This illustrates that MHPs are viable electrode materials and can function as the active layer for photo-charging in photo-rechargeable perovskite batteries. Due to toxicity issues related to Pb-based MHPs, lead-free MHPS also gained a lot of attention in photo-induced batteries. Tewari *et al.*[214] created a photo-rechargeable LIB utilizing a lead-free, fully inorganic perovskite material known as $Cs_3Bi_2I_9$ for the photo-electrode (Fig. 13c and d). In their experiments, the

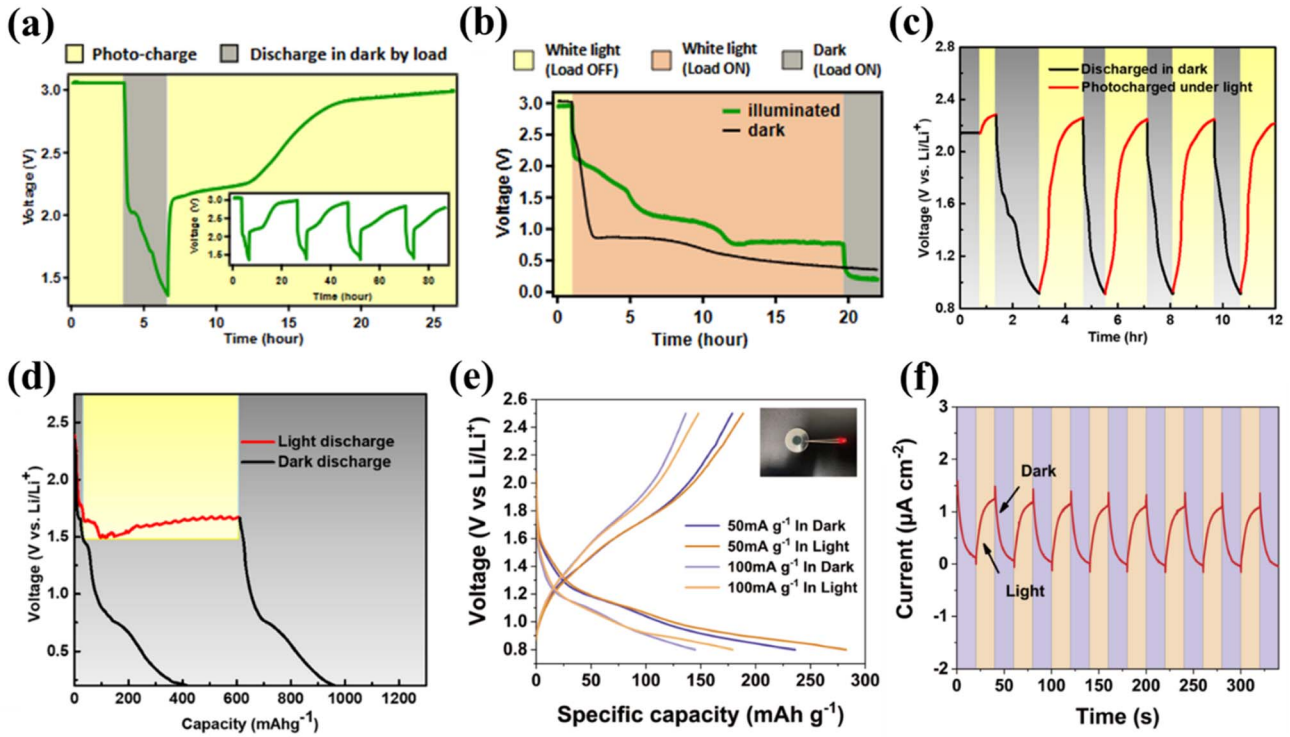

Fig. 13 (a) First photo-charge (at 100 mW cm^{-2}) and discharge (dark, 21.5 kΩ load) voltage profile of the 2D $(PEA)_2PbI_4$ (CHPI). (b) The discharge curves of CHPI based photo-batteries in dark and illuminated conditions[212] Copyright 2018, *Nano Lett.* (c) Cycles of discharge of the $Cs_3Bi_2I_9$ photo-battery in dark at 100 mA g^{-1} followed by photo-charging under 100 mW cm^{-2}. (d) First discharge curves of the $Cs_3Bi_2I_9$ photo-battery in dark and under light. Electrochemical performance of PR-LIB under illumination[214] Copyright 2021, *Nano Lett.* (e) Capacity variation of the PE at 50 and 100 mA g^{-1} under dark and light states. (f) *I*–*T* curves with alternating light and dark states[217] Copyright 2025, *Sci. China Mater.*

battery initially exhibited a discharge capacity of 413 mAh g^{-1} at a current of 50 mA g^{-1}. Nevertheless, after several cycles, the performance deteriorated due to the transformation of bismuth in the perovskite from Bi^{3+} to metallic Bi^0, which influenced the material's structure and functionality. To investigate its photo-charging characteristics, they fabricated the photo-electrode on either FTO-coated glass or porous carbon felt and assessed the battery under light conditions. They discovered that the perovskite was the key component facilitating the light-induced charging process. Upon exposure to light with energy surpassing the bandgap of the perovskite, electrons were excited and traversed a layer of PCBM to reach the current collector, resulting in an accumulation of positive charges (holes) within the perovskite. These holes caused Li-ions to be repelled back into the electrolyte, aiding in the battery's charging process.[212,215] However, further investigation is needed to understand the fate of these photo-generated electrons fully (Table 5).

As noted by Paolella *et al.*, during electrical charging, these electrons could flow through the external circuit to the opposite electrode, where they reduce Li-ions to Li-metal. In scenarios lacking an external circuit, the electrons might interact with the battery's electrolyte (ethylene carbonate/dimethyl carbonate), generating reactive oxygen species that ultimately contribute to the formation of the SEI on Li-metal.[216] Furthermore, Tewari and Shivarudraiah[214] discharged the battery to 0.9 V and then photo-charged it up to approximately 2.5 V under light without any external load. They measured a photo-conversion efficiency of 0.43% during the initial cycle, but this efficiency declined to about 0.1% in subsequent cycles. Despite the existing limitations, their findings indicate that $Cs_3Bi_2I_9$ perovskites have significant potential for photo-rechargeable batteries, and future enhancements in efficiency may stem from a better comprehension of how light-driven charge separation and transport function in these systems. Yin and colleagues have recently developed a photo-rechargeable LIB utilizing a bismuth-based hybrid perovskite known as $(MA)_3Bi_2I_9$, commonly called MBI, as the light-sensitive electrode.[217] Their research demonstrated that this material enhances charge separation when exposed to light, facilitating better Li-ion mobility in the battery and improving its overall performance. Investigations using *ex situ* XRD indicated that Li-ion storage within MBI occurs through a combination of two mechanisms: the insertion of Li-ion into the structure and a chemical conversion reaction. When the battery was evaluated under light conditions, its discharge capacity increased from 236 mAh g^{-1} in darkness to 282.4 mAh g^{-1}, marking a 19.7% enhancement at a current rate of 50 mA g^{-1} (Fig. 13e). This improvement was attributed to the light-generated electrons and holes in MBI, which accelerated charge movement and the flow of Li-ions. This not only increased the battery's capacity but also lowered the charge flow resistance. From the perspective of

Table 5 Summary of different MHP-based photo-induced batteries and their performance

Configuration of PSCs	Configuration of energy storage units	Integrated strategy	Photocharge capacity [mAh g^{-1}]	Photo conversion efficiency (PCE) %	Ref.
ITO/PEDOT:PSS/$MAPbI_3$	$LiFePO_4/Li_4Ti_5O_{12}$	Wire connection of 4 cells	140.4 at 0.5 °C	7.8	41
FTO/$(PEA)_2PbI_4$/rGO	$PEAPbBr_4$/Li	Dual functional electrode	100	0.034	212
ITO/PTAA/$MAPbI_3$/PCBM/BCP/Ag	$LiFePO_4/Li_4Ti_5O_{12}$	DC–DC	0.372 mAh at 6C	9.9	218
ITO/PEDOT:PSS/$MAPbI_3$/PCBM/Ag	$LiFePO_4/Li_4Ti_5O_{12}$	DC–DC	151.3 at 0.5 °C	9.36	219
FTO/rGO (PCBM)/$Cs_3Bi_2I_9$/Cu	$Cs_3Bi_2I_9$/Cu	Dual functional electrode	410	0.43	214
ITO/PYAA/$MAPbI_3$/PCBM/C60/BCP/Al	Al/graphite	Dual functional electrode	757–770	12.04	220
FTO/TiO_2/ZrO_2/$MAPbI_3$/carbon	FTO/NiO/rGO/WO_3/FTO	Wire connection	63 at 5C	—	221
FTO/TiO_2/$MAPbI_3$/carbon	Li/carbon	Joint electrode mode	750	5.14	222
$(MA)_3Bi_2I_9$/rGO	$MA_3Bi_2I_9$/rGO/Li	Dual functional electrode	282.4	11.8	217
$(BA)_2(MA)_3Pb_4I_{13}$/MoS_2/rGO	$(BA)_2(MA)_3Pb_4I_{13}/MoS_2$/rGO/Li	Dual functional electrode	180.67	0.52	223
FTO/$CsPbI_2Br$	S–$Li_7P_{2.9}Sb_{0.1}S_{10.75}O_{0.25}$–C	Dual functional electrode	~1500 at 0.1C	11.2	224
FTO/TiO_2/$MAPbI_3$	FTO/TiO_2/$MAPbI_3$/Zn foil	Dual functional electrode	362	0.31	225
$MAPbI_3$/PEDOT/ZrO_2	$MAPbI_3$/PEDOT/ZrO_2/Zn anode	Dual functional electrode	555	0.51	226

energy efficiency, the battery exhibited better performance in light conditions. It required 0.1 V less for charging, leading to a 6% reduction in energy input, and delivered 0.1 V more during discharge, resulting in an 11.8% increase in energy output (Fig. 13f). In summary, this research indicates that MBI-based batteries could pave the way for the next generation of energy storage solutions devices that are efficient, environmentally friendly, and well-suited for portable electronics powered by light.

5. Perovskites in supercapacitors and photo-induced supercapacitors

The integration of perovskite materials into SCs has garnered considerable attention, given the ongoing efforts to improve energy density, efficiency, and charge storage for bridging the performance differences between standard capacitors and batteries, since they deliver high power density with quick charge–discharge rates. Nonetheless, traditional SCs typically struggle with energy density and stability, while different structures of perovskite materials can enhance their electrochemical performance. In SCs, the spotlight is on identifying the mechanisms by which perovskites affect charge storage and transfer processes and investigating their operational efficiency and cyclic stability.[227,228] Studies demonstrate that ionic and electronic conductivity are essential for supercapacitor performance. In addition, the properties of MHP-based materials can be enhanced by simply making modifications in the crystal structure. Outcomes suggest that perovskite-based supercapacitors significantly increased specific capacitance, reaching over 200 F g^{-1}, compared to the 60–120 F g^{-1} seen in typical carbon-based materials, which stems from the high surface area and superior ionic conductivity of perovskite materials, which allow for more effective ion transport and charge storage.[229] The perovskite SCs performed well over time, retaining over 90% of their initial capacitance after 5.000 charge–discharge cycles.[230] NCs combined with reduced graphene oxide (rGO) have delivered a specific capacitance 178 times better than rGO electrodes on their own.[231] Furthermore, cycle life tests lasting over 10.000 cycles with minimal capacity fade strengthen the case for perovskite-based SCs in practical applications, which closely aligns with the stability problems in other advanced materials.[232] In general, the room temperature laser-triggered technique selected for the conjugation of the two components presents a distinct avenue for the cost-effective and large-scale synthesis of precisely tailored perovskite-2D conjugates.[231] However, limitations of perovskites' usage in SCs are due to their inherent instability and sensitivity to moisture and heat changes. These contentious issues must be systematically addressed to hint at a factual potential for commercial applications in high-performance energy storage. Furthermore, these devices maintain robust capacitance retention, generally above 80% following numerous cycles, suggesting good operational stability. The data suggest that perovskite materials integrated with carbon composites in hybrid electrode designs can create synergistic effects, improving both electron and ion transport,

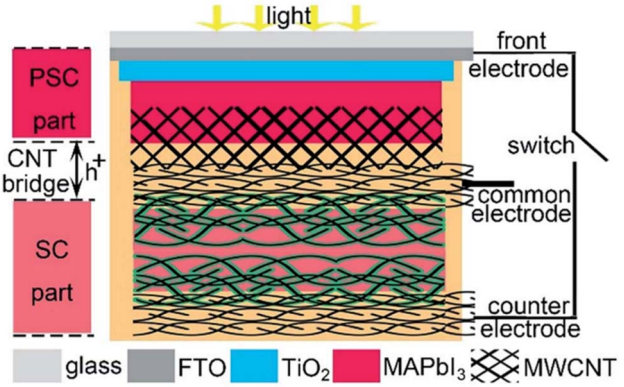

Fig. 14 Representation of the photo capacitor and energy level schematic.[237] Copyright 2017, *J. Mater. Chem. A*.

and thus, performance, and reinforcing the potential benefits of perovskite-based approaches. This can be attributed to the synergy of the EDLC and pseudo capacitance originating from the different components. In particular, they showed a specific capacitance value of 106 F g^{-1} with excellent stability, remaining 97.2% after 100 continuous intercalation/deintercalation scans. This route allows one to create NCs with various morphologies and chemical phases, along with multiple 2D materials, to discover the optimal combinations.[230] Different 2D materials with large electrolyte contact areas and numerous energy storage active sites may serve as alternatives to the low capacitance NH_3-functionalized rGO for enhancing the capacitance of the conjugated systems.[231] For example, layered perovskites are associated with better ion transport dynamics, giving them distinct advantages over materials like manganese oxides and carbon-based electrodes.[232]

When these results focus on nanostructured materials, the performance improvement appears noticeably. These conclusions are also consistent with studies that highlight how scalable synthesis methods have been key in reaching these performance levels with perovskites. Nevertheless, it is also important to note the challenges, particularly concerning the environmental impact and the operational stability of perovskite materials over longer periods. The fine-tuning of the anionic species in the perovskite framework has noticeably improved ionic conductivity, which helps charge move better within the SC.[233] For example, changing the lead content in lead-based perovskites leads to different electrochemical behaviors and stabilities.[230] Similarly, the incorporation of dopants can effectively tweak the bandgap of perovskite materials, increasing their performance in SC applications. Moreover, looking at various perovskite formulations, lower-dimensional perovskites tend to have better capacitance and energy density than their 3D counterparts.[231] The insights could lead to new perovskite composites that further enhance their electrochemical properties, keeping them relevant in the area of energy storage.[234] Sol–gel and hydrothermal methods, for example, give different structures that boost ion conductivity and surface area-both vital for storing charge effectively in SCs.[235] The synthesis method of perovskites may lead to the conclusion that using hydrothermal methods can deliver better electrical performance, with more capacitance and better stability.[228] Adding other elements and materials during production is also essential for the construction of perovskites for supercapacitors.[236] For example, perovskites mixed with conducting polymers can work together to improve both electrical conductivity and mechanical stability. This helps to solve some significant problems when using perovskites in energy storage. Perovskite materials, especially the organic–inorganic type like $MAPbI_3$, are showing power conversion and absorbing light.[231] In general, light intensity and wavelength play a crucial role in getting the most out of perovskites. If light intensity changes, it can significantly enhance charge separation and the speed at which electrons move. Some perovskite structures, such as thin microbelts, convert light into energy, particularly when exposed to visible light. SC energy storage largely depends on what happens electrostatically and electrochemically at the electrode material interface. Photo-induced SCs are based on solar cells for photoelectricity energy conversion and SCs for energy storage. Liu and co-workers have incorporated an all-solid-state photo-charging capacitor based on $MAPbI_3$ and SCs (polyaniline (PANI)/carbon nano tube (CNT)), where the CNT bridge was devoted to preventing water from the aqueous gel electrolytes (Fig. 14). Indeed, the CNT bridge could be a path for holes to transport between the two electrodes.[237]

The MHP-based PSCs achieve excellent charging performance, recording energy, with efficient storage mechanisms,

Table 6 The MHP-based electrodes in electrochemical supercapacitors and photo-induced supercapacitors

Perovskites in electrodes	Specific capacitance [mF cm^{-2}]	Energy density	Capacitance retention	Reference
$MAPbBr_3$	507 [F g^{-1}]	Power density 764 W kg^{-1}	—	239
$MAPbBr_3$	98.36 [F g^{-1}]	—	93% after 2000 cycles	240
2D BA_2PbBr_4	148.25 [F g^{-1}]	—	98% after 2000 cycles	240
Quasi-2D $BA_2MAPb_2Br_7$	138.35 [F g^{-1}]	—	96% after 2000 cycles	240
$CsPbBr_{2.9}I_{0.1}$	150	—	—	241
$MAPbI_3$	432	34.2 Wh kg^{-1}	—	242
$CsPbI_3$	7.23	—	65.5% after 1000 cycles	243
$MAPbI_3$	422	—	70% after 500 cycles	237
CdS-$MAPI_3$	372	23.8	96.6% after 4000 cycles	244
MBI	350	2.98 μF cm^{-2}	94.79% after 5000 cycles	245

and power densities of 30.71 Wh kg^{-1} and 1875 Wh kg^{-1}.[237] Especially when applied in portable electronics, PSCs may have to operate under complex illumination conditions, such as fluctuating sunlight. By creating high-performance supercapacitors, nanostructured electrode materials have outlined tremendous electrochemical characteristics. The improvements in performance and lifespan could be achieved by optimizing the integration of perovskite materials into existing energy storage systems, particularly for energy-harvesting applications, which emphasize the need for scalable and affordable solutions (Table 6). The implications of this research are quite significant, both from a theoretical and a practical point of view, and help to understand the charge storage and transport mechanisms within perovskite materials.[238]

In summary, the improved electrochemical performance of SCs using perovskite materials is directly linked to their distinct structural and compositional benefits, pointing to a clear path for the advancement of energy storage solutions. Perovskites continue to be explored for use in supercapacitors, yet several challenges have surfaced that keep them from being fully used in actual applications. Though the creation of perovskite materials has shown promise, like better electrochemical performance and energy density, some key problems still need to be taken into account. For instance, how stable are perovskite SCs when the environment changes, like with different humidity or temperatures. While they seem to cycle better than older electrode materials, they can still be destroyed over time.[246]

Furthermore, empirical data reveal that perovskite films often have defects and grain boundaries despite improvements in material design, which can harm charge mobility and performance.[231] Prior research supports this, suggesting that refining synthetic techniques is key to reducing defects and improving the electrochemical stability of perovskite systems. Thus, research into perovskite materials for SCs keeps enriching the academic world but also points out the many complexities that must be addressed to reach their full potential. Future research should closely match real-world applications, ensuring that the knowledge gained leads to real progress in sustainable energy technologies.[246]

On the other hand, research toward perovskites' photo-induced functionalities demonstrates how light-induced impacts could enhance energy storage mechanisms in supercapacitors by synergistic interactions between light absorption and the charge storage qualities of perovskite materials.[234] The oxygen vacancies in the perovskite are deemed to remain the charge storage region of the pseudo capacitance. Charge storage of oxygen intercalation and energy densities of perovskite supercapacitors will be enhanced by expanding the vacancies of oxygen.

Mechanisms of photo-induced charge generation and understanding how perovskites generate charge when exposed to light are super important for boosting. Basically, when perovskites absorb light, electrons jump from one energy level (the VB) to a higher one (the CB), and this creates electron–hole pairs. How long these charge carriers stick around depends on the material's band gap, how crystalline it is, and its interface properties. For the best energy storage, there is a need for good charge separation and transport, which lets you capture and release energy in a more dynamic way. Getting a handle on these complex mechanisms is key to using perovskites in energy devices. As we keep researching, tweaking the design and makeup of perovskite materials might solve current problems and help them become more useful in photo-induced SCs.

6. Conclusion and future perspective

MHPs have come a long way from being niche materials for photovoltaics to now a dynamic platform with the potential of revolutionizing energy conversion and storage technologies. Their standout properties, like high ionic conductivity, adjustable optoelectronic properties, expansive surface areas, and structural flexibility, have opened doors for their use in LIBs, SCs, ASEIs, and integrated photo-rechargeable systems. Acting as electrodes and interfacial layers, MHPs enhance energy storage and conversion performance. By advancing compositional engineering, surface passivation, and interface design, perovskite-based devices have been able to achieve improved operational stability and functional versatility, allowing for moving beyond proof-of-concept. Combining carbon with perovskite in hybrid electrodes can enhance electronic conductivity, while approaches like compositional and bandgap engineering (for instance, partially substituting Pb^{2+} with Sn^{2+}) may provide avenues to optimize charge carrier mobility and address toxicity issues. However, as this review points out, there are still several hurdles that need to be overcome before perovskite-based energy technologies can hit the market. These challenges include long-term operational instability when faced with real-world stressors, environmental and health issues tied to lead-containing systems, difficulties in scaling up high-quality large-area films, and the use of toxic or hard-to-handle solvents in material synthesis. To address these issues, not only will materials chemistry have to be bettered gradually, but processing methods will also need to be integrated, sustainable, and scalable. Ultimately, MHPs offer a remarkable opportunity to create self-sustaining, multifunctional energy platforms by integrating photovoltaics with energy storage. The following should be considered when prioritizing future research:

(1) Environmentally friendly chemistries: lead-free MHP formulations that maintain electronic and ionic performance while ensuring long-term chemical stability need to be explored further. Compositional bandgap engineering requires the partial replacement of Pb^{2+} with Sn^{2+} or with other stable metals and surface passivation techniques (by widening the bandgap, it suppresses electron migration).

(2) Scalable and green fabrication methods: pushing forward with solvent-free or hybrid deposition strategies that work well with industrial roll-to-roll processing, ensuring everything stays uniform and reproducible over large areas. Undisputedly, a significant mission in the preparation of MHPs and deposition procedures of perovskite thin film also lies in translating the lab-scale technique to industrially applicable manufacturing methods.

(3) Dimensionality and microstructural engineering: the study of the influence of modifying grain size, controlling

defects, optimizing phase transitions, and nano-structuring on the electrochemical performance is required. Moreover, the enhanced electrochemical performance of low-dimensional MHPs in energy storage systems should be explored further.

(4) Solid-electrolyte: development of advanced methods of dense perovskite-based solid electrolytes, which would lower impedance and boost performance.

(5) Li-transport mechanisms: understanding of Li-ion movement through vacancy, interstitial, or exchange routes within perovskite frameworks is essential for facilitating uniform ion flow and even lithium deposition.

(6) Interface study: diving into advanced characterization and computational modelling to get a grip on defect formation, ion migration, and interfacial degradation, all while keeping it real under actual operating conditions.

(7) ASEI: the MHP interfacial layer protection approach could open a promising avenue for shielding lithium metal from the liquid electrolyte-Li-ion transport gradient layer model.

(8) Fluorinated MHPs: future research should aim at creating open-framework perovskite-derived electrodes and SEIs with fluorinated heterogeneous nanodomains to improve stability and prevent dendrite growth in LIBs.

(9) Circular economy integration: setting up closed-loop recycling protocols for MHP-based devices to tackle end-of-life management, especially for those lead-containing systems. Also, integrate sustainable supply chain practices.

(10) Collaborative pathways: promote interdisciplinary collaboration across materials science, electrochemistry, and device engineering to achieve stable, efficient, and scalable next-generation perovskite-based energy storage solutions.

To conclude, MHPs are poised to redefine energy harvesting, storage, and optoelectronics. In order to transform the energy landscape, MHP-based technologies must strategically tackle current challenges and embrace interdisciplinary innovations. We aim to be both a comprehensive reference and a springboard for such forward-thinking research directions. In turn, profound insights offered by the scientists in the near future will pave the way for discoveries and developments in fertile landscapes of halide perovskite materials and energy storage systems. With profound insights offered by the scientists in the future, further exciting discoveries are certainly to be realized.

Conflicts of interest

There is no conflict of interest.

Data availability

No primary research results, software or code have been included and no new data were generated or analysed as part of this review.

Acknowledgements

As a part of the DESTINY PhD program, this publication is acknowledged by funding from the European Union's Horizon 2020 research and innovation program under the Marie Skłodowska-Curie Actions COFUND (Grant Agreement #945357). The authors also gratefully acknowledge the National Science Centre, Poland, Grants OPUS 2021/41/B/ST5/04450 (W. W. and M. K. K.) and MAESTRO 11, No. 2019/34/A/ST5/00416 (J. L., M. S.), for financial support.

References

1 A. T. Nguyen, V. D. Phung, V. O. Mittova, H. D. Ngo, T. N. Vo, M. L. Le Thi, V. H. Nguyen, I. Y. Mittova, M. L. P. Le, Y. N. Ahn, I. T. Kim and T. L. Nguyen, Fabricating nanostructured $HoFeO_3$ perovskite for lithium-ion battery anodes via co-precipitation, *Scr. Mater.*, 2022, **207**, 114259.

2 Q. Wei, F. Xiong, S. Tan, L. Huang, E. H. Lan, B. Dunn and L. Mai, Porous One-Dimensional Nanomaterials: Design, Fabrication and Applications in Electrochemical Energy Storage, *Adv. Mater.*, 2017, **29**, 1602300.

3 C.-Y. Wang, T. Liu, X.-G. Yang, S. Ge, N. V. Stanley, E. S. Rountree, Y. Leng and B. D. McCarthy, Fast charging of energy-dense lithium-ion batteries, *Nature*, 2022, **611**, 485–490.

4 B. Nykvist and M. Nilsson, Rapidly falling costs of battery packs for electric vehicles, *Nat. Clim. Change*, 2015, **5**, 329–332.

5 S. Yang, Q. Liang, H. Wu, J. Pi, Z. Wang, Y. Luo, Y. Liu, Z. Long, D. Zhou, Y. Wen, Q. Wang, J. Guo and J. Qiu, Lead-Free Double Perovskite $Cs_2NaErCl_6 : Li^+$ as High-Stability Anodes for Li-Ion Batteries, *J. Phys. Chem. Lett.*, 2022, **13**, 4981–4987.

6 C. P. Grey and D. S. Hall, Prospects for lithium-ion batteries and beyond—a 2030 vision, *Nat. Commun.*, 2020, **11**, 6279.

7 R. K. Sahu, S. Gangil, V. K. Bhargav, P. Sahu and B. Ghritalahre, Synthesizing biomass into nano carbon for use in high-performance supercapacitors - A brief critical review, *J. Energy Storage*, 2023, **72**, 108348.

8 W. Zhang, G. E. Eperon and H. J. Snaith, Metal halide perovskites for energy applications, *Nat. Energy*, 2016, **1**, 16048.

9 J. Y. Kim, J.-W. Lee, H. S. Jung, H. Shin and N.-G. Park, High-Efficiency Perovskite Solar Cells, *Chem. Rev.*, 2020, **120**, 7867–7918.

10 C. Yang, W. Hu, J. Liu, C. Han, Q. Gao, A. Mei, Y. Zhou, F. Guo and H. Han, Achievements, challenges, and future prospects for industrialization of perovskite solar cells, *Light: Sci. Appl.*, 2024, **13**, 227.

11 J. Han, K. Park, S. Tan, Y. Vaynzof, J. Xue, E. W.-G. Diau, M. G. Bawendi, J.-W. Lee and I. Jeon, Perovskite solar cells, *Nat. Rev. Methods Primers*, 2025, **5**, 3.

12 L. Yuan, Q. Xue, F. Wang, N. Li, G. I. N. Waterhouse, C. J. Brabec, F. Gao and K. Yan, Perovskite Solar Cells and Light Emitting Diodes: Materials Chemistry, Device Physics and Relationship, *Chem. Rev.*, 2025, **125**, 5057–5162.

13 L. Liang, T. Ma, Z. Chen, J. Wang, J. Hu, Y. Ji, W. Shen and J. Chen, Patterning Technologies for Metal Halide Perovskites: A Review, *Adv. Mater. Technol.*, 2023, **8**, 2200419.

14 M. A. Green, E. D. Dunlop, M. Yoshita, N. Kopidakis, K. Bothe, G. Siefer, X. Hao and J. Y. Jiang, Solar Cell Efficiency Tables (Version 65), *Prog. Photovoltaics Res. Appl.*, 2025, **33**, 3–15.
15 Z.-A. Nan, L. Chen, Q. Liu, S.-H. Wang, Z.-X. Chen, S.-Y. Kang, J.-B. Ji, Y.-Y. Tan, Y. Hui, J.-W. Yan, Z.-X. Xie, W.-Z. Liang, B.-W. Mao and Z.-Q. Tian, Revealing phase evolution mechanism for stabilizing formamidinium-based lead halide perovskites by a key intermediate phase, *Chem*, 2021, **7**, 2513–2526.
16 Z. Liang, Y. Zhang, H. Xu, W. Chen, B. Liu, J. Zhang, H. Zhang, Z. Wang, D.-H. Kang, J. Zeng, X. Gao, Q. Wang, H. Hu, H. Zhou, X. Cai, X. Tian, P. Reiss, B. Xu, T. Kirchartz, Z. Xiao, S. Dai, N.-G. Park, J. Ye and X. Pan, Homogenizing out-of-plane cation composition in perovskite solar cells, *Nature*, 2023, **624**, 557–563.
17 J. Kim, J. Park, J. Lim, J. Kim, J. Kim, N. Shin, J. S. Yun, J. Im and S. Il Seok, Susceptible organic cations enable stable and efficient perovskite solar cells, *Joule*, 2025, **9**, 101879.
18 M. Cheng, Y. Duan, D. Zhang, Z. Xie, H. Li, Q. Cao, Z. Qiu, Y. Chen and Q. Peng, Tailoring Buried Interface and Minimizing Energy Loss Enable Efficient Narrow and Wide Bandgap Inverted Perovskite Solar Cells by Aluminum Glycinate Based Organometallic Molecule, *Adv. Mater.*, 2025, **37**, 2419413.
19 M. Saliba, T. Matsui, J.-Y. Seo, K. Domanski, J.-P. Correa-Baena, M. K. Nazeeruddin, S. M. Zakeeruddin, W. Tress, A. Abate, A. Hagfeldt and M. Grätzel, Cesium-containing triple cation perovskite solar cells: improved stability, reproducibility and high efficiency, *Energy Environ. Sci.*, 2016, **9**, 1989–1997.
20 A. Kojima, K. Teshima, Y. Shirai and T. Miyasaka, Organometal Halide Perovskites as Visible-Light Sensitizers for Photovoltaic Cells, *J. Am. Chem. Soc.*, 2009, **131**, 6050–6051.
21 S. Liu, J. Li, W. Xiao, R. Chen, Z. Sun, Y. Zhang, X. Lei, S. Hu, M. Kober-Czerny, J. Wang, F. Ren, Q. Zhou, H. Raza, Y. Gao, Y. Ji, S. Li, H. Li, L. Qiu, W. Huang, Y. Zhao, B. Xu, Z. Liu, H. J. Snaith, N.-G. Park and W. Chen, Buried interface molecular hybrid for inverted perovskite solar cells, *Nature*, 2024, **632**, 536–542.
22 X. Zhang, S. Wu, H. Zhang, A. K. Y. Jen, Y. Zhan and J. Chu, Advances in inverted perovskite solar cells, *Nat. Photonics*, 2024, **18**, 1243–1253.
23 N. Ren, L. Tan, M. Li, J. Zhou, Y. Ye, B. Jiao, L. Ding and C. Yi, 25% - Efficiency flexible perovskite solar cells via controllable growth of SnO_2, *iEnergy*, 2024, **3**, 39–45.
24 Y. Gao, K. Huang, C. Long, Y. Ding, J. Chang, D. Zhang, L. Etgar, M. Liu, J. Zhang and J. Yang, Flexible Perovskite Solar Cells: From Materials and Device Architectures to Applications, *ACS Energy Lett.*, 2022, **7**, 1412–1445.
25 Y. Cheng and L. Ding, Pushing commercialization of perovskite solar cells by improving their intrinsic stability, *Energy Environ. Sci.*, 2021, **14**, 3233–3255.
26 H. Zhu, S. Teale, M. N. Lintangpradipto, S. Mahesh, B. Chen, M. D. McGehee, E. H. Sargent and O. M. Bakr, Long-term operating stability in perovskite photovoltaics, *Nat. Rev. Mater.*, 2023, **8**, 569–586.
27 P. Zhu, C. Chen, J. Dai, Y. Zhang, R. Mao, S. Chen, J. Huang and J. Zhu, Toward the Commercialization of Perovskite Solar Modules, *Adv. Mater.*, 2024, **36**, 2307357.
28 C. Jing, Z. Lin, Y. Wu and X. Ouyang, Air-Processed Perovskite Solar Cells: Challenges, Progress, and Industrial Strategies, *Small*, 2025, 2504448.
29 X.-K. Liu, W. Xu, S. Bai, Y. Jin, J. Wang, R. H. Friend and F. Gao, Metal halide perovskites for light-emitting diodes, *Nat. Mater.*, 2021, **20**, 10–21.
30 D. Chen, G. Zou, Y. Wu, B. Tang, A. L. Rogach and H. Yip, Metal Halide Perovskite LEDs for Visible Light Communication and Lasing Applications, *Adv. Mater.*, 2024, **37**, 2414745.
31 Y. Fu, H. Zhu, J. Chen, M. P. Hautzinger, X.-Y. Zhu and S. Jin, Metal halide perovskite nanostructures for optoelectronic applications and the study of physical properties, *Nat. Rev. Mater.*, 2019, **4**, 169–188.
32 H. Dong, C. Ran, W. Gao, M. Li, Y. Xia and W. Huang, Metal Halide Perovskite for next-generation optoelectronics: progresses and prospects, *eLight*, 2023, **3**, 3.
33 L. A. Muscarella and E. M. Hutter, Halide Double-Perovskite Semiconductors beyond Photovoltaics, *ACS Energy Lett.*, 2022, **7**, 2128–2135.
34 X. Guan, Z. Lei, X. Yu, C. Lin, J. Huang, C. Huang, L. Hu, F. Li, A. Vinu, J. Yi and T. Wu, Low-Dimensional Metal-Halide Perovskites as High-Performance Materials for Memory Applications, *Small*, 2022, **18**, 2203311.
35 W. Peixiong, C. Xiang, P. Xiaoxin, J. Bowen, L. Xiaoqing, P. Yanqin, P. Jie, T. Li, D. Jinxia, Z. Jun and W. Hao, A mini review of recent progress on halide perovskite memristor devices: materials science, challenges and applications, *Mater. Today Energy*, 2024, **45**, 101692.
36 B. Jiang, X. Chen, X. Pan, L. Tao, Y. Huang, J. Tang, X. Li, P. Wang, G. Ma, J. Zhang and H. Wang, Advances in Metal Halide Perovskite Memristors: A Review from a Co-Design Perspective, *Adv. Sci.*, 2024, **12**, 2409291.
37 W. Xu, H. Cho, Y. Kim, Y. Kim, C. Wolf, C. Park and T. Lee, Organometal Halide Perovskite Artificial Synapses, *Adv. Mater.*, 2016, **28**, 5916–5922.
38 M. Yu, X. Ren, L. Ma and Y. Wu, Integrating a redox-coupled dye-sensitized photoelectrode into a lithium–oxygen battery for photoassisted charging, *Nat. Commun.*, 2014, **5**, 5111.
39 X. Liu, Y. Yuan, J. Liu, B. Liu, X. Chen, J. Ding, X. Han, Y. Deng, C. Zhong and W. Hu, Utilizing solar energy to improve the oxygen evolution reaction kinetics in zinc–air battery, *Nat. Commun.*, 2019, **10**, 4767.
40 J. Han, S. Lee, C. Youn, J. Lee, Y. Kim and T. Choi, Hybrid photoelectrochemical-rechargeable seawater battery for efficient solar energy storage systems, *Electrochim. Acta*, 2020, **332**, 135443.
41 J. Xu, Y. Chen and L. Dai, Efficiently photo-charging lithium-ion battery by perovskite solar cell, *Nat. Commun.*, 2015, **6**, 8103.
42 H. Xue, H. Gong, Y. Yamauchi, T. Sasaki and R. Ma, Photo-enhanced rechargeable high-energy-density metal batteries

for solar energy conversion and storage, *Nano Res. Energy*, 2022, **1**, e9120007.

43 H.-R. Xia, W.-T. Sun and L.-M. Peng, Hydrothermal synthesis of organometal halide perovskites for Li-ion batteries, *Chem. Commun.*, 2015, **51**, 13787–13790.

44 X.-H. Wu, M.-J. Zhao, Y. Chai, Z. Liu, W.-J. Jiang, L.-B. Yang, B.-J. Feng, J.-J. Liu, Q. Yu, K.-Z. Du and Y. Zhao, Unlocking the atomic-scale mechanism of structural evolutions during (de)lithiation and negative-fading in $CsPbBr_3$ anodes, *Energy Storage Mater.*, 2025, **75**, 104043.

45 P. Pal and A. Ghosh, Three-Dimensional $CsPbCl_3$ Perovskite Anode for Quasi-Solid-State Li-Ion and Dual-Ion Batteries: Mechanism of Li^+ Conversion Process in Perovskite, *Phys. Rev. Appl.*, 2020, **14**, 064010.

46 N. Kaisar, T. Paul, P.-W. Chi, Y.-H. Su, A. Singh, C.-W. Chu, M.-K. Wu and P. M. Wu, Electrochemical Performance of Orthorhombic $CsPbI_3$ Perovskite in Li-Ion Batteries, *Materials*, 2021, **14**, 5718.

47 Y.-C. Yin, Q. Wang, J.-T. Yang, F. Li, G. Zhang, C.-H. Jiang, H.-S. Mo, J.-S. Yao, K.-H. Wang, F. Zhou, H.-X. Ju and H.-B. Yao, Metal chloride perovskite thin film-based interfacial layer for shielding lithium metal from liquid electrolyte, *Nat. Commun.*, 2020, **11**, 1761.

48 R. Liu, W. Feng, L. Fang, H. Deng, L. Lin, M. Chen, J.-X. Zhong and W. Yin, An ultrathin Li-doped perovskite SEI film with high Li ion flux for a fast charging lithium metal battery, *Energy Adv.*, 2024, **3**, 2999–3006.

49 A. Sandhu and M. K. Chini, 2D and 3D Halide Perovskite-Based Supercapacitors, *ChemistrySelect*, 2024, **9**, e202304441.

50 M. Riaz, S. M. Ali, R. Alotaibi, S. D. Ali and A. Mehmood, Mesoporous structure of tin (Sn) based inorganic halide perovskite CsSnBr3 binary composite with PANI and rGO for energy storage as supercapacitor electrodes, *Inorg. Chem. Commun.*, 2025, **176**, 114338.

51 X. Zhang, W. Song, J. Tu, J. Wang, M. Wang and S. Jiao, A Review of Integrated Systems Based on Perovskite Solar Cells and Energy Storage Units: Fundamental, Progresses, Challenges, and Perspectives, *Adv. Sci.*, 2021, **8**, 2100552.

52 Y. Chen, Z. Yue, S.-W. Tsang and Y. Cheng, Metal halide perovskites for efficient solar energy conversion and storage systems: Principles, recent advances, challenges and prospects, *Nano Energy*, 2025, **137**, 110782.

53 F. Li, Y. Liang and R. Zheng, A balanced view of ion migration in halide perovskite electronics, *Newton*, 2025, **1**, 100096.

54 T. Oku, Crystal structures of perovskite halide compounds used for solar cells, *Rev. Adv. Mater. Sci.*, 2020, **59**, 264–305.

55 H. Tanaka, T. Oku and N. Ueoka, Structural stabilities of organic–inorganic perovskite crystals, *Jpn. J. Appl. Phys.*, 2018, **57**, 08RE12.

56 Z. Li, M. Yang, J.-S. Park, S.-H. Wei, J. J. Berry and K. Zhu, Stabilizing Perovskite Structures by Tuning Tolerance Factor: Formation of Formamidinium and Cesium Lead Iodide Solid-State Alloys, *Chem. Mater.*, 2016, **28**, 284–292.

57 R. Kour, S. Arya, S. Verma, J. Gupta, P. Bandhoria, V. Bharti, R. Datt and V. Gupta, Potential Substitutes for Replacement of Lead in Perovskite Solar Cells: A Review, *Global Challenges*, 2019, **3**, 1900050.

58 Y. Wang, J. Ren, X. Zhou and G. Zhang, Stability improvements of metal halide perovskite nanocrystals and their optoelectrical applications, *Mater. Chem. Front.*, 2023, **7**, 2175–2207.

59 W. Gao, C. Chen, C. Ran, H. Zheng, H. Dong, Y. Xia, Y. Chen and W. Huang, A-Site Cation Engineering of Metal Halide Perovskites: Version 3.0 of Efficient Tin-Based Lead-Free Perovskite Solar Cells, *Adv. Funct. Mater.*, 2020, **30**, 2000794.

60 D. Duan, C. Ge, M. Z. Rahaman, C.-H. Lin, Y. Shi, H. Lin, H. Hu and T. Wu, Recent progress with one-dimensional metal halide perovskites: from rational synthesis to optoelectronic applications, *NPG Asia Mater.*, 2023, **15**, 8.

61 T. Ibn-Mohammed, S. C. L. Koh, I. M. Reaney, A. Acquaye, G. Schileo, K. B. Mustapha and R. Greenough, Perovskite solar cells: An integrated hybrid lifecycle assessment and review in comparison with other photovoltaic technologies, *Renewable Sustainable Energy Rev.*, 2017, **80**, 1321–1344.

62 J. Huang, Y. Yuan, Y. Shao and Y. Yan, Understanding the physical properties of hybrid perovskites for photovoltaic applications, *Nat. Rev. Mater.*, 2017, **2**, 17042.

63 J.-W. Lee, S. Tan, S. Il Seok, Y. Yang and N.-G. Park, Rethinking the A cation in halide perovskites, *Science*, 2022, 375.

64 M. G. Goesten and R. Hoffmann, Mirrors of Bonding in Metal Halide Perovskites, *J. Am. Chem. Soc.*, 2018, **140**, 12996–13010.

65 J. Han, Y. Li, P. Zhang, B. Xu, X. Xu and Z. Quan, Cooperative Regulation of ns^2 Lone-Pair Expression Realizes Distinct Excitonic Emissions in Hybrid Germanium, Tin, and Lead Halides, *J. Am. Chem. Soc.*, 2025, **147**, 1291–1299.

66 I. Y. H Chang, C. H. Park and K. Matsuishi, First-Principles Study of the Structural and the Electronic Properties of the Lead-Halide-Based Inorganic-Organic Perovskites, *Inorg. Chem.*, 2019, **58**, 4134–4140.

67 K. J. Savill, A. M. Ulatowski and L. M. Herz, Optoelectronic Properties of Tin–Lead Halide Perovskites, *ACS Energy Lett.*, 2021, **6**, 2413–2426.

68 M. Awais, R. L. Kirsch, V. Yeddu and M. I. Saidaminov, Tin Halide Perovskites Going Forward: Frost Diagrams Offer Hints, *ACS Mater. Lett.*, 2021, **3**, 299–307.

69 Y. Zhang, J. D. Lin, V. Vijayaragavan, K. K. Bhakoo and T. T. Y. Tan, Tuning sub-10 nm single-phase $NaMnF_3$ nanocrystals as ultrasensitive hosts for pure intense fluorescence and excellent T1 magnetic resonance imaging, *Chem. Commun.*, 2012, **48**, 10322.

70 C. W. Myung, J. Yun, G. Lee and K. S. Kim, A New Perspective on the Role of A-Site Cations in Perovskite Solar Cells, *Adv. Energy Mater.*, 2018, **8**, 1702898.

71 G. E. Eperon, S. D. Stranks, C. Menelaou, M. B. Johnston, L. M. Herz and H. J. Snaith, Formamidinium lead trihalide: a broadly tunable perovskite for efficient planar heterojunction solar cells, *Energy Environ. Sci.*, 2014, **7**, 982.

72 P. Wu, D. Li, S. Wang and F. Zhang, Magic guanidinium cations in perovskite solar cells: from bulk to interface, *Mater. Chem. Front.*, 2023, **7**, 2507–2527.
73 D. J. Kubicki, D. Prochowicz, A. Hofstetter, M. Saski, P. Yadav, D. Bi, N. Pellet, J. Lewiński, S. M. Zakeeruddin, M. Grätzel and L. Emsley, Formation of Stable Mixed Guanidinium–Methylammonium Phases with Exceptionally Long Carrier Lifetimes for High-Efficiency Lead Iodide-Based Perovskite Photovoltaics, *J. Am. Chem. Soc.*, 2018, **140**, 3345–3351.
74 J. Qin, Z. Che, Y. Kang, C. Liu, D. Wu, H. Yang, X. Hu and Y. Zhan, Towards operation-stabilizing perovskite solar cells: Fundamental materials, device designs, and commercial applications, *InfoMat*, 2024, **6**, e12522.
75 C. C. Stoumpos, C. D. Malliakas and M. G. Kanatzidis, Semiconducting Tin and Lead Iodide Perovskites with Organic Cations: Phase Transitions, High Mobilities, and Near-Infrared Photoluminescent Properties, *Inorg. Chem.*, 2013, **52**, 9019–9038.
76 D. M. Trots and S. V. Myagkota, High-temperature structural evolution of caesium and rubidium triiodoplumbates, *J. Phys. Chem. Solids*, 2008, **69**, 2520–2526.
77 R. Panetta, G. Righini, M. Colapietro, L. Barba, D. Tedeschi, A. Polimeni, A. Ciccioli and A. Latini, Azetidinium lead iodide: synthesis, structural and physico-chemical characterization, *J. Mater. Chem. A*, 2018, **6**, 10135–10148.
78 M. Maçzka, M. Ptak, A. Gągor, D. Stefańska, J. K. Zaręba and A. Sieradzki, Methylhydrazinium Lead Bromide: Noncentrosymmetric Three-Dimensional Perovskite with Exceptionally Large Framework Distortion and Green Photoluminescence, *Chem. Mater.*, 2020, **32**, 1667–1673.
79 C. Yi, J. Luo, S. Meloni, A. Boziki, N. Ashari-Astani, C. Grätzel, S. M. Zakeeruddin, U. Röthlisberger and M. Grätzel, Entropic stabilization of mixed A-cation ABX_3 metal halide perovskites for high performance perovskite solar cells, *Energy Environ. Sci.*, 2016, **9**, 656–662.
80 D. Drozdowski, A. Gągor and M. Mączka, Methylhydrazinium lead iodide – one dimensional chain phase with excitonic absorption and large energy band gap, *J. Mol. Struct.*, 2022, **1249**, 131660.
81 Y. Zhang, G. Grancini, Z. Fei, E. Shirzadi, X. Liu, E. Oveisi, F. F. Tirani, R. Scopelliti, Y. Feng, M. K. Nazeeruddin and P. J. Dyson, Auto-passivation of crystal defects in hybrid imidazolium/methylammonium lead iodide films by fumigation with methylamine affords high efficiency perovskite solar cells, *Nano Energy*, 2019, **58**, 105–111.
82 K. Opała, M. Saski, W. Marynowski, A. Borkenhagen and J. Lewiński, Exploring Polytype Formation in Double-Cation $DMA_xFA_{1-x}Pb_3$ Perovskites: Compositional Engineering and Phase Transitions, *Chem. Mater.*, 2025, **37**, 897–911.
83 M. Šimėnas, S. Balčiūnas, A. Gągor, A. Pieniążek, K. Tolborg, M. Kinka, V. Klimavicius, Š. Svirskas, V. Kalendra, M. Ptak, D. Szewczyk, A. P. Herman, R. Kudrawiec, A. Sieradzki, R. Grigalaitis, A. Walsh, M. Maçzka and J. Banys, Mixology of $MA_{1-x}EA_xPbI_3$ Hybrid Perovskites: Phase Transitions, Cation Dynamics, and Photoluminescence, *Chem. Mater.*, 2022, **34**, 10104–10112.
84 P. Singh, R. Mukherjee and S. Avasthi, Acetamidinium-Substituted Methylammonium Lead Iodide Perovskite Solar Cells with Higher Open-Circuit Voltage and Improved Intrinsic Stability, *ACS Appl. Mater. Interfaces*, 2020, **12**, 13982–13987.
85 M. Nishat, M. K. Hossain, M. R. Hossain, S. Khanom, F. Ahmed and M. A. Hossain, Role of metal and anions in organo-metal halide perovskites $CH_3NH_3MX_3$ (M: Cu, Zn, Ga, Ge, Sn, Pb; X: Cl, Br, I) on structural and optoelectronic properties for photovoltaic applications, *RSC Adv.*, 2022, **12**, 13281–13294.
86 Y. Liang, F. Li, X. Cui, C. Stampfl, S. P. Ringer, X. Yang, J. Huang and R. Zheng, Multiple B-site doping suppresses ion migration in halide perovskites, *Sci. Adv.*, 2025, **11**, eads7054.
87 M. B. Gray, E. T. McClure and P. M. Woodward, $Cs_2AgBiBr_{6-x}Cl_x$ solid solutions – band gap engineering with halide double perovskites, *J. Mater. Chem. C*, 2019, **7**, 9686–9689.
88 A. H. Slavney, T. Hu, A. M. Lindenberg and H. I. Karunadasa, A Bismuth-Halide Double Perovskite with Long Carrier Recombination Lifetime for Photovoltaic Applications, *J. Am. Chem. Soc.*, 2016, **138**, 2138–2141.
89 G. García-Espejo, D. Rodríguez-Padrón, R. Luque, L. Camacho and G. de Miguel, Mechanochemical synthesis of three double perovskites: $Cs_2AgBiBr_6$, $(CH_3NH_3)_2TlBiBr_6$ and $Cs_2AgSbBr_6$, *Nanoscale*, 2019, **11**, 16650–16657.
90 W. Meng, X. Wang, Z. Xiao, J. Wang, D. B. Mitzi and Y. Yan, Parity-Forbidden Transitions and Their Impact on the Optical Absorption Properties of Lead-Free Metal Halide Perovskites and Double Perovskites, *J. Phys. Chem. Lett.*, 2017, **8**, 2999–3007.
91 G. Meyer, Halogen-Elpasolithe, VI [1] Erste Iod-Elpasolithe, $Cs_2^{I}M^{III}I_6$ (B^{I} = Li, Na)/Halo-Elpasolites, VI [1] The First Iodo-Elpasolites, $Cs_2B^{I}M^{III}I_6$ (B^{I} = Li, Na), *Z. Naturforsch., B*, 1980, **35**, 394–396.
92 Z. Deng, F. Wei, F. Brivio, Y. Wu, S. Sun, P. D. Bristowe and A. K. Cheetham, Synthesis and Characterization of the Rare-Earth Hybrid Double Perovskites: $(CH_3NH_3)_2KGdCl_6$ and $(CH_3NH_3)_2KYCl_6$, *J. Phys. Chem. Lett.*, 2017, **8**, 5015–5020.
93 G. T. Kent, E. Morgan, K. R. Albanese, A. Kallistova, A. Brumberg, L. Kautzsch, G. Wu, P. Vishnoi, R. Seshadri and A. K. Cheetham, Elusive Double Perovskite Iodides: Structural, Optical, and Magnetic Properties, *Angew. Chem., Int. Ed.*, 2023, **62**, e202306000.
94 S. Ghosh, H. Shankar and P. Kar, Recent developments of lead-free halide double perovskites: a new superstar in the optoelectronic field, *Mater. Adv.*, 2022, **3**, 3742–3765.
95 D. J. Kubicki, M. Saski, S. MacPherson, K. Gałkowski, J. Lewiński, D. Prochowicz, J. J. Titman and S. D. Stranks, Halide Mixing and Phase Segregation in Cs_2AgBiX_6 (X =

Cl, Br, and I) Double Perovskites from Cesium-133 Solid-State NMR and Optical Spectroscopy, *Chem. Mater.*, 2020, **32**, 8129–8138.

96 F. Wei, Z. Deng, S. Sun, F. Zhang, D. M. Evans, G. Kieslich, S. Tominaka, M. A. Carpenter, J. Zhang, P. D. Bristowe and A. K. Cheetham, Synthesis and Properties of a Lead-Free Hybrid Double Perovskite: $(CH_3NH_3)_2AgBiBr_6$, *Chem. Mater.*, 2017, **29**, 1089–1094.

97 C. Kupfer, J. Elia, M. Kato, A. Osvet and C. J. Brabec, Mechanochemical Synthesis of Cesium Titanium Halide Perovskites $Cs_2TiBr_{6-x}I_x$ (x = 0, 2, 4, 6), *Cryst. Res. Technol.*, 2023, **58**, 2200150.

98 P. Sebastia-Luna, U. Pokharel, B. A. H. Huisman, L. J. A. Koster, F. Palazon and H. J. Bolink, Vacuum-Deposited Cesium Tin Iodide Thin Films with Tunable Thermoelectric Properties, *ACS Appl. Energy Mater.*, 2022, **5**, 10216–10223.

99 S.-T. Ha, R. Su, J. Xing, Q. Zhang and Q. Xiong, Metal halide perovskite nanomaterials: synthesis and applications, *Chem. Sci.*, 2017, **8**, 2522–2536.

100 A. Soultati, M. Tountas, K. K. Armadorou, A. R. b. M. Yusoff, M. Vasilopoulou and M. K. Nazeeruddin, Synthetic approaches for perovskite thin films and single-crystals, *Energy Adv.*, 2023, **2**, 1075–1115.

101 S. Tao, I. Schmidt, G. Brocks, J. Jiang, I. Tranca, K. Meerholz and S. Olthof, Absolute energy level positions in tin- and lead-based halide perovskites, *Nat. Commun.*, 2019, **10**, 2560.

102 K. Chen, S. Schünemann, S. Song and H. Tüysüz, Structural effects on optoelectronic properties of halide perovskites, *Chem. Soc. Rev.*, 2018, **47**, 7045–7077.

103 A. Alaei, A. Circelli, Y. Yuan, Y. Yang and S. S. Lee, Polymorphism in metal halide perovskites, *Mater. Adv.*, 2021, **2**, 47–63.

104 M. Saski, S. Sobczak, P. Ratajczyk, M. Terlecki, W. Marynowski, A. Borkenhagen, I. Justyniak, A. Katrusiak and J. Lewiński, Unprecedented Richness of Temperature- and Pressure-Induced Polymorphism in 1D Lead Iodide Perovskite, *Small*, 2024, **20**, 2403685.

105 M. Simenas, A. Gagor, J. Banys and M. Maczka, Phase Transitions and Dynamics in Mixed Three- and Low-Dimensional Lead Halide Perovskites, *Chem. Rev.*, 2024, **124**, 2281–2326.

106 M. T. Weller, O. J. Weber, P. F. Henry, A. M. Di Pumpo and T. C. Hansen, Complete structure and cation orientation in the perovskite photovoltaic methylammonium lead iodide between 100 and 352 K, *Chem. Commun.*, 2015, **51**, 4180–4183.

107 R. Shi, Q. Fang, A. S. Vasenko, R. Long, W.-H. Fang and O. V. Prezhdo, Structural Disorder in Higher-Temperature Phases Increases Charge Carrier Lifetimes in Metal Halide Perovskites, *J. Am. Chem. Soc.*, 2022, **144**, 19137–19149.

108 H. Jin, Y.-J. Zeng, J. A. Steele, M. B. J. Roeffaers, J. Hofkens and E. Debroye, Phase stabilization of cesium lead iodide perovskites for use in efficient optoelectronic devices, *NPG Asia Mater.*, 2024, **16**, 24.

109 A. Marronnier, G. Roma, S. Boyer-Richard, L. Pedesseau, J.-M. Jancu, Y. Bonnassieux, C. Katan, C. C. Stoumpos, M. G. Kanatzidis and J. Even, Anharmonicity and Disorder in the Black Phases of Cesium Lead Iodide Used for Stable Inorganic Perovskite Solar Cells, *ACS Nano*, 2018, **12**, 3477–3486.

110 M. Szafrański and A. Katrusiak, Photovoltaic Hybrid Perovskites under Pressure, *J. Phys. Chem. Lett.*, 2017, **8**, 2496–2506.

111 L. Kong, G. Liu, J. Gong, Q. Hu, R. D. Schaller, P. Dera, D. Zhang, Z. Liu, W. Yang, K. Zhu, Y. Tang, C. Wang, S.-H. Wei, T. Xu and H. Mao, Simultaneous band-gap narrowing and carrier-lifetime prolongation of organic–inorganic trihalide perovskites, *Proc. Natl. Acad. Sci. U. S. A.*, 2016, **113**, 8910–8915.

112 N. Wang, S. Zhang, S. Wang, X. Yang, F. Guo, Y. Zhang, Z. Gu and Y. Song, Pressure Engineering on Perovskite Structures, Properties, and Devices, *Adv. Funct. Mater.*, 2024, **34**, 2315918.

113 D. D. Nematov, A. S. Burkhonzoda, M. S. Kurboniyon, U. Zafari, K. T. Kholmurodov, M. G. Brik, T. Yamamoto and F. Shokir, The Effect of Phase Changes on Optoelectronic Properties of Lead-Free $CsSnI_3$ Perovskites, *J. Electron. Mater.*, 2025, **54**, 1634–1644.

114 K. Yamada, Y. Kuranaga, K. Ueda, S. Goto, T. Okuda and Y. Furukawa, Phase Transition and Electric Conductivity of $ASnCl_3$ (A = Cs and CH_3NH_3), *Bull. Chem. Soc. Jpn.*, 1998, **71**, 127–134.

115 F. Hao, C. C. Stoumpos, D. H. Cao, R. P. H. Chang and M. G. Kanatzidis, Lead-free solid-state organic–inorganic halide perovskite solar cells, *Nat. Photonics*, 2014, **8**, 489–494.

116 Y. Kawamura, H. Mashiyama and K. Hasebe, Structural Study on Cubic–Tetragonal Transition of $CH_3NH_3PbI_3$, *J. Phys. Soc. Jpn.*, 2002, **71**, 1694–1697.

117 H. Mashiyama, Y. Kawamura, E. Magome and Y. Kubota, Displacive character of the cubic-tetragonal transition in $CH_3NH_3PbX_3$, *J. Korean Phys. Soc.*, 2003, **42**, S1026–S1029.

118 A. Poglitsch and D. Weber, Dynamic disorder in methylammoniumtrihalogenoplumbates (II) observed by millimeter-wave spectroscopy, *J. Chem. Phys.*, 1987, **87**, 6373–6378.

119 E. C. Schueller, G. Laurita, D. H. Fabini, C. C. Stoumpos, M. G. Kanatzidis and R. Seshadri, Crystal Structure Evolution and Notable Thermal Expansion in Hybrid Perovskites Formamidinium Tin Iodide and Formamidinium Lead Bromide, *Inorg. Chem.*, 2018, **57**, 695–701.

120 X. Wang, Q. Wang, Z. Chai and W. Wu, The thermal stability of $FAPbBr_3$ nanocrystals from temperature-dependent photoluminescence and first-principles calculations, *RSC Adv.*, 2020, **10**, 44373–44381.

121 R. J. Sutton, M. R. Filip, A. A. Haghighirad, N. Sakai, B. Wenger, F. Giustino and H. J. Snaith, Cubic or Orthorhombic? Revealing the Crystal Structure of Metastable Black-Phase $CsPbI_3$ by Theory and Experiment, *ACS Energy Lett.*, 2018, **3**, 1787–1794.

122 M. Rodová, J. Brožek, K. Knížek and K. Nitsch, Phase transitions in ternary caesium lead bromide, *J. Therm. Anal. Calorim.*, 2003, **71**, 667–673.

123 I. Chung, J.-H. Song, J. Im, J. Androulakis, C. D. Malliakas, H. Li, A. J. Freeman, J. T. Kenney and M. G. Kanatzidis, $CsSnI_3$: Semiconductor or Metal? High Electrical Conductivity and Strong Near-Infrared Photoluminescence from a Single Material. High Hole Mobility and Phase-Transitions, *J. Am. Chem. Soc.*, 2012, **134**, 8579–8587.

124 D. E. Scaife, P. F. Weller and W. G. Fisher, Crystal preparation and properties of cesium tin(II) trihalides, *J. Solid State Chem.*, 1974, **9**, 308–314.

125 G. Thiele, H. Wilhelm Rotter and K. Schmidt, Kristallstrukturen und Phasentransformationen von Caesiumtrihalogenogermanaten(II) $CsGeX_3$ (X = Cl, Br, I), *Z. Anorg. Allg. Chem.*, 1987, **545**, 148–156.

126 A. Celeste and F. Capitani, Hybrid perovskites under pressure: Present and future directions, *J. Appl. Phys.*, 2022, **132**, 220903.

127 P. Vishnoi and C. N. R. Rao, Temperature and pressure induced structural transitions of lead iodide perovskites, *J. Mater. Chem. A*, 2024, **12**, 19–37.

128 P. Gratia, I. Zimmermann, P. Schouwink, J.-H. Yum, J.-N. Audinot, K. Sivula, T. Wirtz and M. K. Nazeeruddin, The Many Faces of Mixed Ion Perovskites: Unraveling and Understanding the Crystallization Process, *ACS Energy Lett.*, 2017, **2**, 2686–2693.

129 S. Shao and M. A. Loi, Advances and Prospective in Metal Halide Ruddlesen–Popper Perovskite Solar Cells, *Adv. Energy Mater.*, 2021, **11**, 2003907.

130 P. Zhu and J. Zhu, Low-dimensional metal halide perovskites and related optoelectronic applications, *InfoMat*, 2020, **2**, 341–378.

131 G. Wang, S. Mei, J. Liao, W. Wang, Y. Tang, Q. Zhang, Z. Tang, B. Wu and G. Xing, Advances of Nonlinear Photonics in Low-Dimensional Halide Perovskites, *Small*, 2021, **17**, 2100809.

132 M. Li, R. Begum, J. Fu, Q. Xu, T. M. Koh, S. A. Veldhuis, M. Grätzel, N. Mathews, S. Mhaisalkar and T. C. Sum, Low threshold and efficient multiple exciton generation in halide perovskite nanocrystals, *Nat. Commun.*, 2018, **9**, 4197.

133 M. C. Brennan, J. E. Herr, T. S. Nguyen-Beck, J. Zinna, S. Draguta, S. Rouvimov, J. Parkhill and M. Kuno, Origin of the Size-Dependent Stokes Shift in $CsPbBr_3$ Perovskite Nanocrystals, *J. Am. Chem. Soc.*, 2017, **139**, 12201–12208.

134 P. Vashishtha, D. Z. Metin, M. E. Cryer, K. Chen, J. M. Hodgkiss, N. Gaston and J. E. Halpert, Shape-, Size-, and Composition-Controlled Thallium Lead Halide Perovskite Nanowires and Nanocrystals with Tunable Band Gaps, *Chem. Mater.*, 2018, **30**, 2973–2982.

135 K. Leng, I. Abdelwahab, I. Verzhbitskiy, M. Telychko, L. Chu, W. Fu, X. Chi, N. Guo, Z. Chen, Z. Chen, C. Zhang, Q.-H. Xu, J. Lu, M. Chhowalla, G. Eda and K. P. Loh, Molecularly thin two-dimensional hybrid perovskites with tunable optoelectronic properties due to reversible surface relaxation, *Nat. Mater.*, 2018, **17**, 908–914.

136 J. Xing, Y. Zhao, M. Askerka, L. N. Quan, X. Gong, W. Zhao, J. Zhao, H. Tan, G. Long, L. Gao, Z. Yang, O. Voznyy, J. Tang, Z.-H. Lu, Q. Xiong and E. H. Sargent, Color-stable highly luminescent sky-blue perovskite light-emitting diodes, *Nat. Commun.*, 2018, **9**, 3541.

137 D. Prochowicz, M. Saski, P. Yadav, M. Grätzel and J. Lewiński, Mechanoperovskites for Photovoltaic Applications: Preparation, Characterization, and Device Fabrication, *Acc. Chem. Res.*, 2019, **52**, 3233–3243.

138 J. Shamsi, A. S. Urban, M. Imran, L. De Trizio and L. Manna, Metal Halide Perovskite Nanocrystals: Synthesis, Post-Synthesis Modifications, and Their Optical Properties, *Chem. Rev.*, 2019, **119**, 3296–3348.

139 Y. Zhang, T. D. Siegler, C. J. Thomas, M. K. Abney, T. Shah, A. De Gorostiza, R. M. Greene and B. A. Korgel, A "Tips and Tricks" Practical Guide to the Synthesis of Metal Halide Perovskite Nanocrystals, *Chem. Mater.*, 2020, **32**, 5410–5423.

140 R. Vidal, J.-A. Alberola-Borràs, S. N. Habisreutinger, J.-L. Gimeno-Molina, D. T. Moore, T. H. Schloemer, I. Mora-Seró, J. J. Berry and J. M. Luther, Assessing health and environmental impacts of solvents for producing perovskite solar cells, *Nat. Sustainability*, 2020, **4**, 277–285.

141 W. Zuo, M. M. Byranvand, T. Kodalle, M. Zohdi, J. Lim, B. Carlsen, T. Magorian Friedlmeier, M. Kot, C. Das, J. I. Flege, W. Zong, A. Abate, C. M. Sutter-Fella, M. Li and M. Saliba, Coordination Chemistry as a Universal Strategy for a Controlled Perovskite Crystallization, *Adv. Mater.*, 2023, **35**, 2302889.

142 D. Prochowicz, M. Franckevičius, A. M. Cieślak, S. M. Zakeeruddin, M. Grätzel and J. Lewiński, Mechanosynthesis of the hybrid perovskite $CH_3NH_3PbI_3$: characterization and the corresponding solar cell efficiency, *J. Mater. Chem. A*, 2015, **3**, 20772–20777.

143 D. Prochowicz, P. Yadav, M. Saliba, D. J. Kubicki, M. M. Tavakoli, S. M. Zakeeruddin, J. Lewiński, L. Emsley and M. Grätzel, One-step mechanochemical incorporation of an insoluble cesium additive for high performance planar heterojunction solar cells, *Nano Energy*, 2018, **49**, 523–528.

144 D. Prochowicz, P. Yadav, M. Saliba, M. Saski, S. M. Zakeeruddin, J. Lewiński and M. Grätzel, Mechanosynthesis of pure phase mixed-cation $MA_xFA_{1-x}PbI_3$ hybrid perovskites: photovoltaic performance and electrochemical properties, *Sustainable Energy Fuels*, 2017, **1**, 689–693.

145 D. Prochowicz, P. Yadav, M. Saliba, M. Saski, S. M. Zakeeruddin, J. Lewiński and M. Grätzel, Reduction in the Interfacial Trap Density of Mechanochemically Synthesized $MAPbI_3$, *ACS Appl. Mater. Interfaces*, 2017, **9**, 28418–28425.

146 F. Palazon, Y. El Ajjouri and H. J. Bolink, Making by Grinding: Mechanochemistry Boosts the Development of Halide Perovskites and Other Multinary Metal Halides, *Adv. Energy Mater.*, 2019, **10**, 1902499.

147 M. F. Mohamad Noh, N. A. Arzaee, I. N. Nawas Mumthas, N. A. Mohamed, S. N. F. Mohd Nasir, J. Safaei, A. R. bin M. Yusoff, M. K. Nazeeruddin and M. A. Mat Teridi, High-humidity processed perovskite solar cells, *J. Mater. Chem. A*, 2020, **8**, 10481–10518.

148 A. Khorasani, F. Mohamadkhani, M. Marandi, H. Luo and M. Abdi-Jalebi, Opportunities, Challenges, and Strategies for Scalable Deposition of Metal Halide Perovskite Solar Cells and Modules, *Adv. Energy Sustainability Res.*, 2024, **5**, 2300275.

149 J. Burschka, N. Pellet, S.-J. Moon, R. Humphry-Baker, P. Gao, M. K. Nazeeruddin and M. Grätzel, Sequential deposition as a route to high-performance perovskite-sensitized solar cells, *Nature*, 2013, **499**, 316–319.

150 A. Ummadisingu and M. Grätzel, Revealing the detailed path of sequential deposition for metal halide perovskite formation, *Sci. Adv.*, 2018, **4**, e1701402.

151 A. Ummadisingu, S. Meloni, A. Mattoni, W. Tress and M. Grätzel, Crystal-Size-Induced Band Gap Tuning in Perovskite Films, *Angew. Chem., Int. Ed.*, 2021, **60**, 21368–21376.

152 K. J. Prince, H. M. Mirletz, E. A. Gaulding, L. M. Wheeler, R. A. Kerner, X. Zheng, L. T. Schelhas, P. Tracy, C. A. Wolden, J. J. Berry, S. Ovaitt, T. M. Barnes and J. M. Luther, Sustainability pathways for perovskite photovoltaics, *Nat. Mater.*, 2025, **24**, 22–33.

153 Y. Zhang, M. Chen, Y. Zhou, W. Li, Y. Lee, H. Kanda, X. Gao, R. Hu, K. G. Brooks, R. Zia, S. Kinge, N. P. Padture and M. K. Nazeeruddin, The Synergism of DMSO and Diethyl Ether for Highly Reproducible and Efficient $MA_{0.5}FA_{0.5}PbI_3$ Perovskite Solar Cells, *Adv. Energy Mater.*, 2020, **10**, 2001300.

154 J. Küffner, J. Hanisch, T. Wahl, J. Zillner, E. Ahlswede and M. Powalla, One-Step Blade Coating of Inverted Double-Cation Perovskite Solar Cells from a Green Precursor Solvent, *ACS Appl. Energy Mater.*, 2021, **4**, 11700–11710.

155 H.-S. Yun, H. W. Kwon, M. J. Paik, S. Hong, J. Kim, E. Noh, J. Park, Y. Lee and S. Il Seok, Ethanol-based green-solution processing of α-formamidinium lead triiodide perovskite layers, *Nat. Energy*, 2022, **7**, 828–834.

156 J. Ávila, C. Momblona, P. P. Boix, M. Sessolo and H. J. Bolink, Vapor-Deposited Perovskites: The Route to High-Performance Solar Cell Production?, *Joule*, 2017, **1**, 431–442.

157 F. U. Kosasih, E. Erdenebileg, N. Mathews, S. G. Mhaisalkar and A. Bruno, Thermal evaporation and hybrid deposition of perovskite solar cells and mini-modules, *Joule*, 2022, **6**, 2692–2734.

158 Z. Zhang, R. Ji, M. Kroll, Y. J. Hofstetter, X. Jia, D. Becker-Koch, F. Paulus, M. Löffler, F. Nehm, K. Leo and Y. Vaynzof, Efficient Thermally Evaporated γ-$CsPbI_3$ Perovskite Solar Cells, *Adv. Energy Mater.*, 2021, **11**, 2100299.

159 H. Li, J. Zhou, L. Tan, M. Li, C. Jiang, S. Wang, X. Zhao, Y. Liu, Y. Zhang, Y. Ye, W. Tress and C. Yi, Sequential vacuum-evaporated perovskite solar cells with more than 24% efficiency, *Sci. Adv.*, 2022, **8**, eabo7422.

160 A. Singh, J. Hieulle, J. F. Machado, S. Gharabeiki, W. Zuo, M. U. Farooq, H. Phirke, M. Saliba and A. Redinger, Coevaporation Stabilizes Tin-Based Perovskites in a Single Sn-Oxidation State, *Nano Lett.*, 2022, **22**, 7112–7118.

161 A. Z. Afshord, B. E. Uzuner, W. Soltanpoor, S. H. Sedani, T. Aernouts, G. Gunbas, Y. Kuang and S. Yerci, Efficient and Stable Inverted Wide-Bandgap Perovskite Solar Cells and Modules Enabled by Hybrid Evaporation-Solution Method, *Adv. Funct. Mater.*, 2023, **33**, 2301695.

162 W. Chen, S. Zhou, J. Cao, L. Yuan and W. Liu, Controlled Crystallization and Enhanced Performance of γ-$CsPbI_3$ Perovskite Through Methylammonium Iodide-Assisted Coevaporation, *Small Methods*, 2024, **9**, 2400796.

163 N. Leupold and F. Panzer, Recent Advances and Perspectives on Powder-Based Halide Perovskite Film Processing, *Adv. Funct. Mater.*, 2021, **31**, 2007350.

164 E. Couderc, Perovskite photovoltaics: Manufacturing costs, *Nat. Energy*, 2017, **2**, 17080.

165 Y. Liu, Z. Zhang, T. Wu, W. Xiang, Z. Qin, X. Shen, Y. Peng, W. Shen, Y. Li and L. Han, Cost Effectivities Analysis of Perovskite Solar Cells: Will it Outperform Crystalline Silicon Ones?, *Nano-Micro Lett.*, 2025, **17**, 219.

166 J. A. Dawson, A. J. Naylor, C. Eames, M. Roberts, W. Zhang, H. J. Snaith, P. G. Bruce and M. S. Islam, Mechanisms of Lithium Intercalation and Conversion Processes in Organic–Inorganic Halide Perovskites, *ACS Energy Lett.*, 2017, **2**, 1818–1824.

167 N. Vicente and G. Garcia-Belmonte, Methylammonium Lead Bromide Perovskite Battery Anodes Reversibly Host High Li-Ion Concentrations, *J. Phys. Chem. Lett.*, 2017, **8**, 1371–1374.

168 N. Vicente, D. Bresser, S. Passerini and G. Garcia-Belmonte, Probing the 3-step Lithium Storage Mechanism in $CH_3NH_3PbBr_3$ Perovskite Electrode by *Operando* -XRD Analysis, *ChemElectroChem*, 2019, **6**, 456–460.

169 D. Ramirez, Y. Suto, N. C. Rosero-Navarro, A. Miura, K. Tadanaga and F. Jaramillo, Structural and Electrochemical Evaluation of Three- and Two-Dimensional Organohalide Perovskites and Their Influence on the Reversibility of Lithium Intercalation, *Inorg. Chem.*, 2018, **57**, 4181–4188.

170 L. T. López, D. Ramírez, F. Jaramillo and J. A. Calderón, Novel hybrid organic-inorganic $CH_3NH_3NiCl_3$ active material for high-capacity and sustainable lithium-ion batteries, *Electrochim. Acta*, 2020, **357**, 136882.

171 D. Maity, B. Kaur, P. Ghosal and M. Deepa, Large Alkylammonium Cation Based 2D-3D Hybrid Perovskite with Fast Charge Conduction for a Li-Ion Battery Anode, *ACS Appl. Energy Mater.*, 2025, **8**, 76–86.

172 M. Tathavadekar, S. Krishnamurthy, A. Banerjee, S. Nagane, Y. Gawli, A. Suryawanshi, S. Bhat, D. Puthusseri, A. D. Mohite and S. Ogale, Low-dimensional hybrid perovskites as high performance anodes for alkali-ion batteries, *J. Mater. Chem. A*, 2017, **5**, 18634–18642.

173 K. Roy, T. Li, S. Ogale and N. Robertson, Hybrid perovskite-like iodobismuthates as low-cost and stable anode

materials for lithium-ion battery applications, *J. Mater. Chem. A*, 2021, **9**, 2689–2693.

174 F. Moradi and A. Iagaru, Dual-tracer imaging of malignant bone involvement using PET, *Clin. Transl. Imaging*, 2015, **3**, 123–131.

175 Q. Wang, T. Yang, H. Wang, J. Zhang, X. Guo, Z. Yang, S. Lu and W. Qin, Morphological and chemical tuning of lead halide perovskite mesocrystals as long-life anode materials in lithium-ion batteries, *CrystEngComm*, 2019, **21**, 1048–1059.

176 Q. Jiang, M. Chen, J. Li, M. Wang, X. Zeng, T. Besara, J. Lu, Y. Xin, X. Shan, B. Pan, C. Wang, S. Lin, T. Siegrist, Q. Xiao and Z. Yu, Electrochemical Doping of Halide Perovskites with Ion Intercalation, *ACS Nano*, 2017, **11**, 1073–1079.

177 S. Liu, K. Zhang, L. Tan, S. Qi, G. Liu, J. Chen and Y. Lou, All-inorganic halide perovskite $CsPbBr_3$@CNTs composite enabling superior lithium storage performance with pseudocapacitive contribution, *Electrochim. Acta*, 2021, **367**, 137352.

178 W. Xie, J. Cao, P. Li, M. Fan, S. Xu, J. Du and J. Zhang, Stabilized anode-electrolyte interfaces via $Cs_4Pb(Cl/Br/I)_6$ perovskite crystal based glass-ceramics for fast and long cycle-life lithium ion batteries, *Mater. Des.*, 2022, **220**, 110860.

179 T. Paul, S. Maiti, B. K. Chatterjee, P. Bairi, B. K. Das, S. Thakur and K. K. Chattopadhyay, Electrochemical Performance of 3D Network $CsPbBr_3$ Perovskite Anodes for Li-Ion Batteries: Experimental Venture with Theoretical Expedition, *J. Phys. Chem. C*, 2021, **125**, 16892–16902.

180 A. Mathieson, M. Rahil, Y. Zhang, W. M. Dose, J. T. Lee, F. Deschler, S. Ahmad and M. De Volder, Ruddlesden Popper 2D perovskites as Li-ion battery electrodes, *Mater. Adv.*, 2021, **2**, 3370–3377.

181 L. T. C. Lopez, J. C. Alvarez Quiceno, F. Jaramillo, J. M. Osorio-Guillén and J. A. Calderón, Enhancement of electrochemical stability by molecular cation vacancies of the electrode material $CH_3NH3NiCl_3$ for lithium-ion batteries, *J. Electroanal. Chem.*, 2024, **968**, 118505.

182 W. Zhao, C. Liu and X. Yin, Cs_4PbBr_6 Combined with Graphite as Anode for High-Performance Lithium Batteries, *Metals*, 2022, **12**, 1584.

183 J. Cao, W. Xie, K. Liu, X. Meng, J. Zhang, J. Zhang, Z. Yao and M. Fan, SnF_2 -Doped Cs_4PbBr_6 Glass Ceramic as a High-Performance Anode for Li-Ion Batteries, *J. Phys. Chem. C*, 2022, **126**, 3359–3365.

184 X. Liu, R. Wei, S. Fu, W. Xie, S. Xu and J. Zhang, Cs_4PbBr_6 QDs silicate glass-ceramic: A potential anode material for LIBs, *Ceram. Int.*, 2022, **48**, 23293–23299.

185 X.-H. Wu, Y. Chai, J. Shen, P.-W. Huang, S.-Y. Xu, H.-Y. Zhong, B.-C. Chen, Y. Zhao, B. Sa and K.-Z. Du, Deciphering the role of van der Waals heterostructures in enhancing layered perovskite anodes for high-performance lithium-ion batteries, *J. Mater. Chem. A*, 2025, **13**, 8750–8760.

186 H. Kong, J. Wu, Y. Han, Y. Zhang, N. Zhou, Q. Chen, W. Sun, H. Zhou and L.-M. Peng, One-dimensional perovskite-based Li-ion battery anodes with high capacity and cycling stability, *J. Energy Chem.*, 2022, **72**, 73–80.

187 W. Jia, J. Bao, H. Zhang, M. Wu, J. Qiu, H. Wu and Y. Zhang, Effect of Mn-ion Reconstructed Lattice on Lead-Free Halide Perovskite $Cs_3Bi_{2-X}Mn_xCl_9$ Anode in Li-ion Batteries, *J. Environ. Sci.*, 2025, **159**, 154–165.

188 A. Kostopoulou, D. Vernardou, K. Savva and E. Stratakis, All-inorganic lead halide perovskite nanohexagons for high performance air-stable lithium batteries, *Nanoscale*, 2019, **11**, 882–889.

189 H. Wu, J. Pi, Q. Liu, Q. Liang, J. Qiu, J. Guo, Z. Long, D. Zhou and Q. Wang, All-Inorganic Lead Free Double Perovskite Li-Battery Anode Material Hosting High Li^+ Ion Concentrations, *J. Phys. Chem. Lett.*, 2021, **12**, 4125–4129.

190 J. Bao, W. Jia, H. Zhang, M. Wu, J. Qiu, H. Wu and Y. Zhang, Synergistic Enhancement of Mn^{2+} Doping and Thermal Field Treatment on $Cs_2NaBiCl_6$ Double Perovskite Anode Performance for Lithium-Ion Batteries, *J. Phys. Chem. C*, 2025, **129**, 8521–8528.

191 Z. Shi, J. Guo, Y. Chen, Q. Li, Y. Pan, H. Zhang, Y. Xia and W. Huang, Lead-Free Organic–Inorganic Hybrid Perovskites for Photovoltaic Applications: Recent Advances and Perspectives, *Adv. Mater.*, 2017, **186**, 113649.

192 S. F. Hoefler, G. Trimmel and T. Rath, Progress on lead-free metal halide perovskites for photovoltaic applications: a review, *Monatsh. Chem.*, 2017, **148**, 795–826.

193 P. Pandey, N. Sharma, R. A. Panchal, S. W. Gosavi and S. Ogale, Realization of High Capacity and Cycling Stability in Pb-Free A_2CuBr_4 (A=CH_3NH_3/Cs, 2D/3D) Perovskite-Based Li-Ion Battery Anodes, *ChemSusChem*, 2019, **12**, 3742–3746.

194 X.-Q. Zhang, X.-B. Cheng, X. Chen, C. Yan and Q. Zhang, Fluoroethylene Carbonate Additives to Render Uniform Li Deposits in Lithium Metal Batteries, *Adv. Funct. Mater.*, 2017, **27**, 1605989.

195 X.-B. Cheng, T.-Z. Hou, R. Zhang, H.-J. Peng, C.-Z. Zhao, J.-Q. Huang and Q. Zhang, Dendrite-Free Lithium Deposition Induced by Uniformly Distributed Lithium Ions for Efficient Lithium Metal Batteries, *Adv. Mater.*, 2016, **28**, 2888–2895.

196 D. Rehnlund, F. Lindgren, S. Böhme, T. Nordh, Y. Zou, J. Pettersson, U. Bexell, M. Boman, K. Edström and L. Nyholm, Lithium trapping in alloy forming electrodes and current collectors for lithium based batteries, *Energy Environ. Sci.*, 2017, **10**, 1350–1357.

197 S. Rajendran, N. K. Thangavel, K. Mahankali and L. M. R. Arava, Toward Moisture-Stable and Dendrite-Free Garnet-Type Solid-State Electrolytes, *ACS Appl. Energy Mater.*, 2020, **3**, 6775–6784.

198 X.-B. Cheng, C. Yan, X. Chen, C. Guan, J.-Q. Huang, H.-J. Peng, R. Zhang, S.-T. Yang and Q. Zhang, Implantable Solid Electrolyte Interphase in Lithium-Metal Batteries, *Chem*, 2017, **2**, 258–270.

199 F. Ding, W. Xu, G. L. Graff, J. Zhang, M. L. Sushko, X. Chen, Y. Shao, M. H. Engelhard, Z. Nie, J. Xiao, X. Liu, P. V. Sushko, J. Liu and J.-G. Zhang, Dendrite-Free

Lithium Deposition via Self-Healing Electrostatic Shield Mechanism, *J. Am. Chem. Soc.*, 2013, **135**, 4450–4456.

200 N. Liu, J. Baek, S. M. Kim, S. Hong, Y. K. Hong, Y. S. Kim, H.-S. Kim, S. Kim and J. Park, Improving the Stability of High-Performance Multilayer MoS_2 Field-Effect Transistors, *ACS Appl. Mater. Interfaces*, 2017, **9**, 42943–42950.

201 Q. Wu, G. Wang, Q. Huang, S. Xie, J. Huang and X. Wang, Perovskite-type $La_{0.6}Sr_{0.4}Co_{0.2}Fe_{0.8}O_{3-\delta}$ as an artificial interphase layer for dendrite-free Li metal anodes, *Chem. Eng. J.*, 2022, **444**, 136340.

202 Z. Yu, Y. Cui and Z. Bao, Design Principles of Artificial Solid Electrolyte Interphases for Lithium-Metal Anodes, *Cell Rep. Phys. Sci.*, 2020, **1**, 100119.

203 R. Xu, X.-B. Cheng, C. Yan, X.-Q. Zhang, Y. Xiao, C.-Z. Zhao, J.-Q. Huang and Q. Zhang, Artificial Interphases for Highly Stable Lithium Metal Anode, *Matter*, 2019, **1**, 317–344.

204 X.-B. Cheng, R. Zhang, C.-Z. Zhao and Q. Zhang, Toward Safe Lithium Metal Anode in Rechargeable Batteries: A Review, *Chem. Rev.*, 2017, **117**, 10403–10473.

205 Y. Zhang, Y. Liu, J. Zhou, D. Wang, L. Tan and C. Yi, 3D cubic framework of fluoride perovskite SEI inducing uniform lithium deposition for air-stable and dendrite-free lithium metal anodes, *Chem. Eng. J.*, 2022, **431**, 134266.

206 N. Kaisar, A. Singh, P.-Y. Yang, Y.-T. Chen, S. Li, C.-W. Pao, S. Jou and C.-W. Chu, Long-lifespan lithium–metal batteries obtained using a perovskite intercalation layer to stabilize the lithium electrode, *J. Mater. Chem. A*, 2020, **8**, 9137–9145.

207 S. Bai, P. Da, C. Li, Z. Wang, Z. Yuan, F. Fu, M. Kawecki, X. Liu, N. Sakai, J. T.-W. Wang, S. Huettner, S. Buecheler, M. Fahlman, F. Gao and H. J. Snaith, Planar perovskite solar cells with long-term stability using ionic liquid additives, *Nature*, 2019, **571**, 245–250.

208 M. Kim, G.-H. Kim, T. K. Lee, I. W. Choi, H. W. Choi, Y. Jo, Y. J. Yoon, J. W. Kim, J. Lee, D. Huh, H. Lee, S. K. Kwak, J. Y. Kim and D. S. Kim, Methylammonium Chloride Induces Intermediate Phase Stabilization for Efficient Perovskite Solar Cells, *Joule*, 2019, **3**, 2179–2192.

209 Y. Wang, M. I. Dar, L. K. Ono, T. Zhang, M. Kan, Y. Li, L. Zhang, X. Wang, Y. Yang, X. Gao, Y. Qi, M. Grätzel and Y. Zhao, Thermodynamically stabilized β-$CsPbI_3$–based perovskite solar cells with efficiencies >18%, *Science*, 2019, **365**, 591–595.

210 M. Yang, D. Wang, Y. Ling, X. Guo and W. Chen, Emerging Advanced Photo-Rechargeable Batteries, *Adv. Funct. Mater.*, 2024, **34**, 2410398.

211 L. Song, Y. Fan, H. Fan, X. Yang, K. Yan, X. Wang and L. Ma, Photo-assisted rechargeable metal batteries, *Nano Energy*, 2024, **125**, 109538.

212 S. Ahmad, C. George, D. J. Beesley, J. J. Baumberg and M. De Volder, Photo-Rechargeable Organo-Halide Perovskite Batteries, *Nano Lett.*, 2018, **18**, 1856–1862.

213 M. He, L. Zhang and J. Li, Theoretical investigation on interactions between lithium ions and two-dimensional halide perovskite for solar-rechargeable batteries, *Appl. Surf. Sci.*, 2021, **541**, 148509.

214 N. Tewari, S. B. Shivarudraiah and J. E. Halpert, Photorechargeable Lead-Free Perovskite Lithium-Ion Batteries Using Hexagonal $Cs_3Bi_2I_9$ Nanosheets, *Nano Lett.*, 2021, **21**, 5578–5585.

215 B. D. Boruah, B. Wen and M. De Volder, Light Rechargeable Lithium-Ion Batteries Using V_2O_5 Cathodes, *Nano Lett.*, 2021, **21**, 3527–3532.

216 A. Paolella, C. Faure, G. Bertoni, S. Marras, A. Guerfi, A. Darwiche, P. Hovington, B. Commarieu, Z. Wang, M. Prato, M. Colombo, S. Monaco, W. Zhu, Z. Feng, A. Vijh, C. George, G. P. Demopoulos, M. Armand and K. Zaghib, Light-assisted delithiation of lithium iron phosphate nanocrystals towards photo-rechargeable lithium ion batteries, *Nat. Commun.*, 2017, **8**, 14643.

217 X. Yin, G. Di, Y. Liu, G. Wang, C. Mi, Y. Kuang, X. Xiang, X. Sun, E. Edri, X. Lv and M. Li, An energy-saving photo-rechargeable lithium-ion battery based on lead-free hybrid perovskite, *Sci. China Mater.*, 2025, **68**, 1091–1099.

218 L. Kin, Z. Liu, O. Astakhov, S. N. Agbo, H. Tempel, S. Yu, H. Kungl, R.-A. Eichel, U. Rau, T. Kirchartz and T. Merdzhanova, Efficient Area Matched Converter Aided Solar Charging of Lithium Ion Batteries Using High Voltage Perovskite Solar Cells, *ACS Appl. Energy Mater.*, 2020, **3**, 431–439.

219 A. Gurung, K. Chen, R. Khan, S. S. Abdulkarim, G. Varnekar, R. Pathak, R. Naderi and Q. Qiao, Highly Efficient Perovskite Solar Cell Photocharging of Lithium Ion Battery Using DC–DC Booster, *Adv. Energy Mater.*, 2017, **7**, 1602105.

220 Y. Hu, Y. Bai, B. Luo, S. Wang, H. Hu, P. Chen, M. Lyu, J. Shapter, A. Rowan and L. Wang, A Portable and Efficient Solar-Rechargeable Battery with Ultrafast Photo-Charge/Discharge Rate, *Adv. Energy Mater.*, 2019, **9**, 1900872.

221 X. Xia, Z. Ku, D. Zhou, Y. Zhong, Y. Zhang, Y. Wang, M. J. Huang, J. Tu and H. J. Fan, Perovskite solar cell powered electrochromic batteries for smart windows, *Mater. Horiz.*, 2016, **3**, 588–595.

222 P. Chen, G. Li, T. Li and X. Gao, Solar-Driven Rechargeable Lithium–Sulfur Battery, *Adv. Sci.*, 2019, **6**, 1900620.

223 T.-T. Li, Y.-B. Yang, B.-S. Zhao, Y. Wu, X.-W. Wu, P. Chen and X.-P. Gao, Photo-rechargeable all-solid-state lithium – sulfur batteries based on perovskite indoor photovoltaic modules, *Chem. Eng. J.*, 2023, **455**, 140684.

224 R. M. Ansari, S. Chamola and S. Ahmad, Ruddlesden–Popper 2D Perovskite-MoS_2 Hybrid Heterojunction Photocathodes for Efficient and Scalable Photo-Rechargeable Li-Ion Batteries, *Small*, 2024, **20**, 2401350.

225 H. Liu, P. Wu, R. Wang, H. Meng, Y. Zhang, W. Bao and J. Li, A Photo-rechargeable Aqueous Zinc–Tellurium Battery Enabled by the Janus-Jointed Perovskite/Te Photocathode, *ACS Nano*, 2023, **17**, 1560–1569.

226 H. Hassan, A. Althobaiti, A. Mohammad, Z. Ahmad, I. Barsoum, M. Sohail, S. Mumtaz and A. A. Rafi, A hybrid MAPbI3/PEDOT-ZrO2 perovskedot composite for enhanced stability and charge transport in photo-batteries, *Inorg. Chem. Commun.*, 2024, **170**, 113380.

227 Y. Qian, Q. Ruan, M. Xue and L. Chen, Emerging perovskite materials for supercapacitors: Structure, synthesis, modification, advanced characterization, theoretical calculation and electrochemical performance, *J. Energy Chem.*, 2024, **89**, 41–70.

228 P. Simon and Y. Gogotsi, Materials for electrochemical capacitors, *Nat. Mater.*, 2008, **7**, 845–854.

229 M. Mohan, N. P. Shetti and T. M. Aminabhavi, Perovskites: A new generation electrode materials for storage applications, *J. Power Sources*, 2023, **574**, 233166.

230 R. J. Kashtiban, C. E. Patrick, Q. Ramasse, R. I. Walton and J. Sloan, Picoperovskites: The Smallest Conceivable Isolated Halide Perovskite Structures Formed within Carbon Nanotubes, *Adv. Mater.*, 2022, **35**, 2208575.

231 A. Kostopoulou, D. Vernardou, N. Livakas, K. Brintakis, S. Daskalakis and E. Stratakis, Harnessing laser technology to create stable metal halide perovskite–rGO conjugates as promising electrodes for Zn-ion capacitors, *Nanoscale*, 2024, **16**, 6455–6463.

232 A. Vilanova, P. Dias, T. Lopes and A. Mendes, The route for commercial photoelectrochemical water splitting: a review of large-area devices and key upscaling challenges, *Chem. Soc. Rev.*, 2024, **53**, 2388–2434.

233 M. A. Kuzina, D. D. Kartsev, A. V. Stratonovich and P. A. Levkin, Organogels versus Hydrogels: Advantages, Challenges, and Applications, *Adv. Funct. Mater.*, 2023, **33**, 2301421.

234 M. Titirici, P. Johansson, M. Crespo Ribadeneyra, H. Au, A. Innocenti, S. Passerini, E. Petavratzi, P. Lusty, A. A. Tidblad, A. J. Naylor, R. Younesi, Y. A. Chart, J. Aspinall, M. Pasta, J. Orive, L. M. Babulal, M. Reynaud, K. G. Latham, T. Hosaka, S. Komaba, J. Bitenc, A. Ponrouch, H. Zhang, M. Armand, R. Kerr, P. C. Howlett, M. Forsyth, J. Brown, A. Grimaud, M. Vilkman, K. B. Dermenci, S. Mousavihashemi, M. Berecibar, J. E. Marshall, C. R. McElroy, E. Kendrick, T. Safdar, C. Huang, F. M. Zanotto, J. F. Troncoso, D. Z. Dominguez, M. Alabdali, U. Vijay, A. A. Franco, S. Pazhaniswamy, P. S. Grant, S. López Guzman, M. Fehse, M. Galceran and N. Antuñano, 2024 roadmap for sustainable batteries, *J. Phys. Energy*, 2024, **6**, 041502.

235 A. S. R. Bati, Y. L. Zhong, P. L. Burn, M. K. Nazeeruddin, P. E. Shaw and M. Batmunkh, Next-generation applications for integrated perovskite solar cells, *Commun. Mater.*, 2023, **4**, 2.

236 E. Davari and D. G. Ivey, Bifunctional electrocatalysts for Zn–air batteries, *Sustainable Energy Fuels*, 2018, **2**, 39–67.

237 R. Liu, C. Liu and S. Fan, A photocapacitor based on organometal halide perovskite and PANI/CNT composites integrated using a CNT bridge, *J. Mater. Chem. A*, 2017, **5**, 23078–23084.

238 D. Meng, H. Gu, Q. Lu, Y. Zhao, G. Zhu, Y. Zhang, Q. Zhong and Y. Bu, Advances and Perspectives for the Application of Perovskite Oxides in Supercapacitors, *Energy Fuels*, 2021, **35**, 17353–17371.

239 P. Andričević, X. Mettan, M. Kollár, B. Náfrádi, A. Sienkiewicz, T. Garma, L. Rossi, L. Forró and E. Horváth, Light-Emitting Electrochemical Cells of Single Crystal Hybrid Halide Perovskite with Vertically Aligned Carbon Nanotubes Contacts, *ACS Photonics*, 2019, **6**, 967–975.

240 A. Mahapatra, M. Mandal, A. Das Mahapatra, V. Anilkumar, J. Nawrocki, R. D. Chavan, P. Yadav and D. Prochowicz, Mechanochemically-assisted synthesis of 3D, 2D and quasi 2D lead halide perovskites for supercapacitor applications, *Mater. Adv.*, 2024, **5**, 3881–3889.

241 C. H. Ng, H. N. Lim, S. Hayase, Z. Zainal, S. Shafie, H. W. Lee and N. M. Huang, Cesium Lead Halide Inorganic-Based Perovskite-Sensitized Solar Cell for Photo-Supercapacitor Application under High Humidity Condition, *ACS Appl. Energy Mater.*, 2018, **1**, 692–699.

242 A. Slonopas, H. Ryan and P. Norris, Ultrahigh energy density $CH_3NH_3PbI_3$ perovskite based supercapacitor with fast discharge, *Electrochim. Acta*, 2019, **307**, 334–340.

243 P. Maji, A. Ray, P. Sadhukhan, A. Roy and S. Das, Fabrication of symmetric supercapacitor using cesium lead iodide ($CsPbI_3$) microwire, *Mater. Lett.*, 2018, **227**, 268–271.

244 L. E. Oloore, M. A. Gondal, I. K. Popoola and A. Popoola, Cadmium Sulfide Quantum Dots–Organometallic Halide Perovskite Bilayer Electrode Structures for Supercapacitor Applications, *ChemElectroChem*, 2020, **7**, 486–492.

245 I. K. Popoola, M. A. Gondal, A. Popoola and L. E. Oloore, Bismuth-based organometallic-halide perovskite photo-supercapacitor utilizing novel polymer gel electrolyte for hybrid energy harvesting and storage applications, *J. Energy Storage*, 2022, **53**, 105167.

246 S. Güz, M. Buldu-Akturk, H. Göçmez and E. Erdem, All-in-One Electric Double Layer Supercapacitors Based on $CH_3NH_3PbI_3$ Perovskite Electrodes, *ACS Omega*, 2022, **7**, 47306–47316.